Effects of a Geostrophic Current on the Propagation and Generation of Internal Tides

by

Yangxin He

A thesis
presented to the University of Waterloo
in fulfillment of the
thesis requirement for the degree of
Doctor of Philosophy
in
Applied Mathematics

Waterloo, Ontario, Canada, 2021

© Yangxin He 2021

Examining Committee Membership

The following served on the Examining Committee for this thesis. The decision of the Examining Committee is by majority vote.

Supervisor:	Kevin Lamb Professor, Dept. of Applied Mathematics, University of Waterloo
External Examiner:	Leo Maas Professor, Utrecht University
Internal Member:	Francis Poulin Professor, Dept. of Applied Mathematics, University of Waterloo
Internal Member:	Sander Rhebergen Professor, Dept. of Applied Mathematics, University of Waterloo
Internal-External Member:	Cecile Devaud Professor, Dept. of Mechanical and Mechatronics Engineering, University of Waterloo

Author's Declaration

This thesis consists of material all of which I authored or co-authored: see Statement of Contributions included in the thesis. This is a true copy of the thesis, including any required final revisions, as accepted by my examiners.

I understand that my thesis may be made electronically available to the public.

Statement of Contributions

Yangxin He is the sole author of Chapters 1, 2 and 5 which were written under the supervision of Prof. Kevin Lamb. These three Chapters were not written for publication.

This thesis consists in part of two manuscipts written for publication. Chapter 3 has been submitted to Physics of Fluids. The first part of Chapter 4 sections 4.1 and 4.2 has been submitted to Journal of Fluid Mechanics. The second part of Chapter 4 section 4.3 is part of an ongoing work.

Apart from the aforementioned papers, the content of a paper published in 2019, which was accomplished during this PhD program, is not included in the thesis. The citation of this paper is:

He, Yangxin, Kevin G. Lamb, and Ren-Chieh Lien. "Internal solitary waves with subsurface cores." Journal of Fluid Mechanics 873 (2019): 1-17.

Abstract

Internal tides (ITs) are ubiquitous in a stratified ocean where they are generated in response to tidal flows incident upon bottom topography. Along-shelf currents or boundary currents are ocean currents commonly observed along coastlines. We investigate the effects of a geostrophic current on the propagation and generation of ITs by performing numerical experiments using the MITgcm.

As a mode-one IT propagates perpendicularly across a geostrophic current $V(x, z)$, we have investigated the amount of IT energy reflected from the current and the impact of the current on the transmitted wave field. These are quantified by considering the reflection coefficient R and the linear modal energy conversion P_n, where n is the modal number. Here a linear theory built upon idealized barotropic currents is presented. Fully nonlinear numerical simulations are used for the baroclinic currents. We conclude that the reflection is determined by the horizontal shear of the current V_x through varying the effective frequency f_{eff}. The modal energy conversion P_n is determined by the vertical shear of the current V_z, i.e. the horizontal variation of the density ρ_x as a result of the thermal wind relation. The current can increase R up to approximately 50%. However, P_n is less than 6% among all our simulations. This indicates that IT can propagate through the current without losing much of its structure and the interaction is mostly linear.

The effects of along-shelf barotropic geostrophic currents on IT generation by the K_1 tide interacting with a shelf at near-critical latitudes is investigated. We use barotropic currents because it is the simplest way to study the effect of the horizontal shear of the current without complications of a horizontally varying stratification. The horizontal shear of the background current results in a spatially varying effective Coriolis frequency which modifies the slope criticality and potentially creates blocking regions where freely propagating internal tides cannot exist. This thesis is focused on the barotropic to baroclinic energy conversion rate, which is affected by a combination of three factors: slope criticality, size and location of the blocking region where the conversion rate is extremely small and the IT beam patterns. All of these can be significantly altered by the presence of the current. In our parameter space, the current can increase the conversion rate up to 10 times. On the other hand, we have started examining the frequency of the generated internal waves under the influence of the current. Questions have been posed in the thesis and this is part of our ongoing work.

Acknowledgements

Many thanks to Kevin Lamb for being an excellent and patient supervisor. I would like to thank Francis Poulin and Sander Rhebergen for serving as my committee members, and also thank Leo Maas and Cecile Devaud for serving on my examining committee.

I would like to express appreciation for the support of my family. To my husband, Anson Maitland, my mother-in-law Karen Maitland and my father-in-law Daniel Maitland.

Further thanks are extended to my colleagues who have helped in many ways throughout my graduate studies. I would like to thank Ben Storer, Chengzhu Xu, David Deepwell, Michael Dunphy, Matthew Harris and Xiaolin Bai.

Dedication

This thesis is dedicated to Little Bear and Mooncake.

Table of Contents

List of Figures

List of Tables

Chapter 1

Background

Internal waves (IWs) are waves in a density stratified fluid driven by gravitational restoring forces acting on vertically displaced fluid. Approximately half the IW energy in the ocean is generated by tide-topography interactions which primarily generate IWs of tidal frequency called the internal tide (IT). Studies of ITs have attracted considerable attention, because these waves can have a significant impact on oceanic mixing, transport of energy, large scale ocean circulation and shaping the continental shelves. Understanding the propagation and generation of ITs has been an active area of research. The thesis contributes to this area by investigating the influence of geostrophic currents on IT propagation and generation. It is organised in the following manner. Background material and literature review are presented in Chapter 1. The numerical model is introduced in Chapter 2. Two separate works are carried out studying the effects of a geostrophic current on internal waves in Chapter 3 and Chapter 4, respectively. More details on these two chapters will be explained in section 1.4.3 after we introduce the background information.

We begin the discussion of the relevant background material by introducing the governing equations. Then we move on to the linearised equations and the basic properties for internal waves (IWs), followed by the energetics. We then present the literature review summarising past works on IWs and its interaction with geostrophic currents.

1.1 Governing equations

We use the two dimensional Navier-Stokes equations in the vertical plane (also referred to 2.5 dimensional since the velocity component in the third direction, v, is included) with

the Boussinesq approximation on traditional f-plane, which are given by

$$u_t + uu_x + wu_z - fv = -p_x + D_1, \tag{1.1}$$
$$v_t + uv_x + wv_z + fu = D_2, \tag{1.2}$$
$$\epsilon_{nh}\big(w_t + uw_x + ww_z\big) = -p_z - \rho g + \epsilon_{nh} D_3, \tag{1.3}$$

subject to the incompressibility constraint

$$u_x + w_z = 0, \tag{1.4}$$

where the viscosity terms are

$$D_1 = (\nu_H u_x)_x + (\nu_z u_z)_z, \tag{1.5}$$
$$D_2 = (\nu_H v_x)_x + (\nu_z v_z)_z, \tag{1.6}$$
$$D_3 = (\nu_H w_x)_x + (\nu_z w_z)_z. \tag{1.7}$$

Here ν_H and ν_z are the horizontal and vertical eddy viscosities. The hydrostatic approximation is made when $\epsilon_{nh} = 0$. $f = 2\Omega \sin(\phi)$ is the Coriolis parameter, where Ω is the Earth's angular velocity and ϕ is the latitude. In the traditional f-plane approximation, only the vertical component of the Earth's angular velocity is included. The density equation is derived from thermodynamics:

$$\frac{1}{\rho_0} \cdot \frac{D\rho}{Dt} = \frac{1}{\rho_0}\big(\frac{\partial}{\partial t}\rho + u\rho_x + w\rho_z\big) = \frac{D_p}{\rho_0}, \tag{1.8}$$

where D_p is the diffusion

$$D_p = (\kappa \rho_z)_z. \tag{1.9}$$

Note the horizontal diffusion is not implemented [Stashchuk et al., 2017], and κ is the vertical diffusivity. ρ_0 is the constant reference density used in the Boussinesq approximation.

1.2 Linear theory

We consider the linearised equations of the inviscid governing equations (1.1) to (1.8). In the absence of a geostrophic current, we have the equations for internal waves (IWs)

$$\begin{aligned} u_t - fv &= -p_x/\rho_0, && (1.10)\\ v_t + fu &= 0, && (1.11)\\ \epsilon_{nh} w_t &= (-p_z - \rho g)/\rho_0, && (1.12)\\ \rho_t - w\frac{N^2}{g}\rho_0 &= 0, && (1.13)\\ u_x + w_z &= 0. && (1.14) \end{aligned}$$

Combining these equations, we get a wave equation for the vertical velocity w [Kundu et al., 2008],

$$\left(\epsilon_{nh} w_{xx} + w_{zz}\right)_{tt} + N^2 w_{xx} + f^2 w_{zz} = 0. \tag{1.15}$$

The buoyancy frequency squared is defined as

$$N^2 = -\frac{g}{\rho_0}\frac{d\rho}{dz}. \tag{1.16}$$

1.2.1 Vertical modes

We consider a horizontally unbounded ocean with a rigid lid and a flat bottom, where IWs are vertically trapped and can only propagate horizontally. We substitute a horizontal wave with a general vertical structure $\phi_n(z)$,

$$w = \phi_n(z) e^{i(k_n x - \sigma t)}, \tag{1.17}$$

into the w-equation 1.15. The subscript n represents the mode number, k_n is the horizontal wavenumber and σ is the wave frequency. We obtain the eigenvalue equation

$$\frac{d^2\phi_n(z)}{dz^2} + k_n^2\left(\frac{N^2 - \epsilon_{nh}\sigma^2}{\sigma^2 - f^2}\right)\phi_n(z) = 0, \tag{1.18}$$

with the no-normal flow boundary conditions at the top and bottom

$$\phi_n(0) = \phi_n(-H) = 0, \tag{1.19}$$

where H is the constant water depth. If N^2 is constant, we have the analytic solution

$$\phi_n(z) = \sin(m_n z), \tag{1.20}$$

where

$$m_n = \frac{n\pi}{H}. \tag{1.21}$$

The dispersion relation can be obtained by substituting the solution for $\phi_n(z)$ into 1.18,

$$\sigma^2 = \frac{N^2 k_n^2 + f^2 m_n^2}{\epsilon_{nh} k_n^2 + m_n^2}. \tag{1.22}$$

$f \ll N$ in the ocean. From the dispersion relation, we can see that freely propagating IWs can only exist if $f < \sigma < N$. The phase speed of the IW equals the frequency divided by the horizontal wavenumber,

$$c_p = \frac{\sigma}{k_n} = \frac{1}{k_n}\sqrt{\frac{N^2 k_n^2 + f^2 m_n^2}{\epsilon_{nh} k_n^2 + m_n^2}}. \tag{1.23}$$

The group velocity is given by the horizontal number gradient of the frequency,

$$c_g = \frac{\partial \sigma}{\partial k_n} = \frac{k_n m_n^2 (N^2 - \epsilon_{nh} f^2)}{\sigma(\epsilon_{nh} k_n^2 + m_n^2)^2} = \frac{(k_n/m_n)(N^2 - \epsilon_{nh} f^2)}{\sigma(\epsilon_{nh}(k_n/m_n)^2 + 1)^2} \cdot \frac{1}{m_n}. \tag{1.24}$$

The phase speed c represents the propagation of wave crests and troughs. The group velocity c_g gives the propagation of wave energy, so it is very important as the energy budget is concerned. We can re-write the dispersion relation (1.22),

$$\sigma^2 = \frac{N^2 (k_n/m_n)^2 + f^2}{\epsilon_{nh}(k_n/m_n)^2 + 1}. \tag{1.25}$$

If we fix N and f, IWs with the same frequency σ have the same ratio of k_n/m_n. Both m_n and k_n are proportional to n from (1.21). c and c_g are inversely proportional to n. As the mode number n increases, c_p and c_g decrease.

If the buoyancy frequency square is of a general form $N^2(z)$, the vertical structure $\phi_n(z)$ needs to be solved numerically and is described by the eigenvalue problem,

$$\frac{d^2\phi_n(z)}{dz^2} + k_n^2 M^2(z)\phi_n(z) = 0, \tag{1.26}$$

$$\phi_n(0) = \phi_n(-H) = 0. \tag{1.27}$$

There are a countable infinity of eigenvalues giving the vertical modes. We assume the frequency of the wave is constant, and the weighting function $M^2(z)$ is solely dependent on the buoyancy frequency.

$$M^2(z) = \begin{cases} \frac{N^2(z)-\sigma^2}{\sigma^2-f^2} & \text{non-hydrostatic,} \\ \\ \frac{N^2(z)}{\sigma^2-f^2} & \text{hydrostatic.} \end{cases} \tag{1.28}$$

We can multiply the equation (1.26) by ϕ_m and integrate it from $-H$ to 0.

$$\int_{-H}^{0} \phi_n'' \phi_m + k_n^2 M^2 \phi_n \phi_m dz = 0. \tag{1.29}$$

Through integration by parts, (1.29) becomes

$$\phi_n' \phi_m|_{-H}^{0} - \int_{-H}^{0} \phi_n' \phi_m' dz + k_n^2 \int_{-H}^{0} M^2 \phi_n \phi_m dz = 0. \tag{1.30}$$

Using the boundary conditions in (1.27), equation (1.30) becomes

$$-\int_{-H}^{0} \phi_n' \phi_m' dz + k_n^2 \int_{-H}^{0} M^2 \phi_n \phi_m dz = 0. \tag{1.31}$$

Now we repeat the steps above and exchange the subscripts m and n, we have

$$-\int_{-H}^{0} \phi_m' \phi_n' dz + k_m^2 \int_{-H}^{0} M^2 \phi_m \phi_n dz = 0. \tag{1.32}$$

Comparing (1.31) and (1.32), if $n \neq m$ and $k_n^2 \neq k_m^2$, we have

$$\int_{-H}^{0} \phi_m' \phi_n' dz = 0, \tag{1.33}$$

$$\int_{-H}^{0} M^2 \phi_m \phi_n dz = 0. \tag{1.34}$$

If $n = m$ and $k_n^2 = k_m^2$, we can scale the eigenfunction so that

$$\int_{-H}^{0} (\phi_n')^2 dz = k_n^2, \tag{1.35}$$

$$\int_{-H}^{0} M^2 (\phi_n)^2 dz = 1. \tag{1.36}$$

In summary, we obtain the orthogonality conditions for the eigenfunction ϕ_n,

$$\int_{-H}^{0} \phi_m' \phi_n' dz = k_n^2 \delta_{mn}, \tag{1.37}$$

$$\int_{-H}^{0} M^2 \phi_m \phi_n dz = \delta_{mn}. \tag{1.38}$$

Consider a wave field comprised of linear waves of a single frequency σ. The wave field can be decomposed into vertical modes. The decomposition procedure is the same for constant and non-constant N^2. The only difference is how to find $\phi_n(z)$. The decomposition for pressure is not included because it is not useful for the calculations in this thesis.

$$u(x,y,z,t) = \sum u_n(x,y,t)\phi_n'(z), \tag{1.39}$$

$$v(x,y,z,t) = \sum v_n(x,y,t)\phi_n'(z), \tag{1.40}$$

$$w(x,y,z,t) = \sum w_n(x,y,t)\phi_n(z), \tag{1.41}$$

$$\rho(x,y,z,t) = \sum \rho_n(x,y,t)\phi_n(z). \tag{1.42}$$

If we use the orthogonality conditions (1.37) and (1.38), we have the projection coefficients u_n, v_n, w_n and ρ_n. This is used in Chapter 3 to calculate the energy in different modes.

$$u_n(x,y,t) = \frac{1}{k_n^2} \int_{-H}^{0} u\phi_n' dz, \tag{1.43}$$

$$v_n(x,y,t) = \frac{1}{k_n^2} \int_{-H}^{0} v\phi_n' dz, \tag{1.44}$$

$$w_n(x,y,t) = \int_{-H}^{0} wM^2\phi_n dz, \tag{1.45}$$

$$\rho_n(x,y,t) = \int_{-H}^{0} \rho M^2 \phi_n dz. \tag{1.46}$$

1.2.2 Internal plane waves

Now we consider an unbounded fluid with a constant buoyancy frequency N. We look for two-dimensional solutions of the form $w = w_0 e^{i(kx+mz-\sigma t)}$, where (k, m) is the wave vector, w_0 is a real valued constant and σ is the wave frequency. Substituting w into the

w-equation (1.15) gives us the dispersion relation,

$$\sigma^2 = \frac{N^2k^2 + f^2m^2}{\epsilon_{nh}k^2 + m^2}. \tag{1.47}$$

Denote $\epsilon = \frac{k}{m} = \tan(\theta)$, where θ is the angle the wave vector makes with the positive y-axis. We can re-write the dispersion relation as

$$\sigma^2 = \frac{N^2\epsilon^2 + f^2}{\epsilon_{nh}\epsilon^2 + 1}. \tag{1.48}$$

This shows that the wave frequency σ only depends on the direction of the wave vector not its magnitude through the parameter ϵ. The phase velocity of the wave is

$$\vec{c}_p = \frac{\sigma}{|\vec{k}|} \cdot \frac{\vec{k}}{|\vec{k}|} = \frac{\sigma}{|\vec{k}|^2} \cdot (k, m). \tag{1.49}$$

Here $|\vec{k}| = \sqrt{k^2 + m^2}$ is the magnitude of wave vector $\vec{k}$. The group velocity of the wave is

$$\vec{c}_g = (\frac{\partial\sigma}{\partial k}, \frac{\partial\sigma}{\partial m}) = \frac{N^2 - \epsilon_{nh}f^2}{\sigma|\vec{k}|^2} \cdot (m, -k). \tag{1.50}$$

From the expressions in (1.49) and (1.50), we can see the direction of $\vec{c}$ is along the wave vector $\vec{k}$ while the group velocity $\vec{c}_g$ is perpendicular to $\vec{k}$ because $\vec{c}_g \cdot \vec{c} = 0$.

1.2.3 Internal wave beams

We continue the discussion from the previous sub-section. An interesting fact is that the linear internal plane wave solutions for constant N are also exact nonlinear solutions of the fully nonlinear equation because the nonlinear terms cancel each other in each of the nonlinear equations. This is also true for any linear superposition of the plane waves with the same frequency and parallel wave vectors is also a solution for the nonlinear equations:

$$u(x, z, t) = \sum a_j \cos(k_j x + m_j z - \sigma t + \phi_j), \tag{1.51}$$

where the subscript j represents the jth plane wave, (k_j, m_j) is the jth wave vector, a_j is the jth amplitude, ϕ_j is the jth phase shift and σ is the wave frequency. σ is the same for all

the plane waves, so $\epsilon = |\frac{k_j}{m_j}|$ stays constant. For simplicity, if we assume the wavenumbers k_j and m_j have the same signs, we can write the solution as

$$u(x,z,t) = \int_0^\infty a(m)\cos(\epsilon m x + mz - \sigma t + \phi(m))\,dm. \tag{1.52}$$

Alternatively we can write it as the real part of

$$u(x,z,t) = e^{-i\sigma t}\int_0^\infty a(m)e^{i(\epsilon m x + mz)}\,dm, \tag{1.53}$$

where $a(m)$ is in general complex. This is a general solution of an IW beam. Theoretically we can have a beam with infinite width. In reality, the IW beams always have a finite width. Intense research has been done to investigate IW beams. More details can be referred to the review paper by [Dauxois et al., 2018]. In short, the energy of the beam propagates along the beam. This means the slope of the beam represents the propagation direction of the group velocity c_g, which is $\pm\epsilon$. From the dispersion relation in 1.47, we have

$$\epsilon^2 = \frac{\sigma^2 - f^2}{N^2 - \epsilon_{nh}\sigma^2}, \tag{1.54}$$

If we keep N and f fixed, increasing the frequency σ increases the beam slope. If we fix σ, increasing either N or f reduces the slope of the beam. We demonstrate this using a simple example in Figure 1.1. The plot shows results from a numerical simulation of IW generation under the hydrostatic approximation $\epsilon_{nh} = 0$ by tide-topography interactions in the ocean. The IW has a K_1 frequency $\sigma \approx 7.29 \times 10^{-5} s^{-1}$. The constant buoyancy frequency $N = 1\times10^{-3}s^{-1}$. The beam slope is around 0.029 and 0.053 for $f = 6.7\times10^{-5}s^{-1}$ and $f = 5.0 \times 10^{-5}s^{-1}$, respectively. We can see clearly that decreasing f can significantly steepen the beam slope (green lines in Figure 1.1). More details on the propagation of IW beams generated by tide-topography interactions are discussed in Chapter 4.

1.2.4 Effects of a geostrophic current

The analysis on linear theories so far has only IWs in a quiescent fluid. In this section we consider including a geostrophic current. Along-shelf currents or boundary currents are ocean currents commonly observed along coastlines. The latitudinal dependence of the Coriolis force coupled with the wind stress on the water causes the movement of along-shelf currents. Boundary currents are categorized by their east-west locations. Western

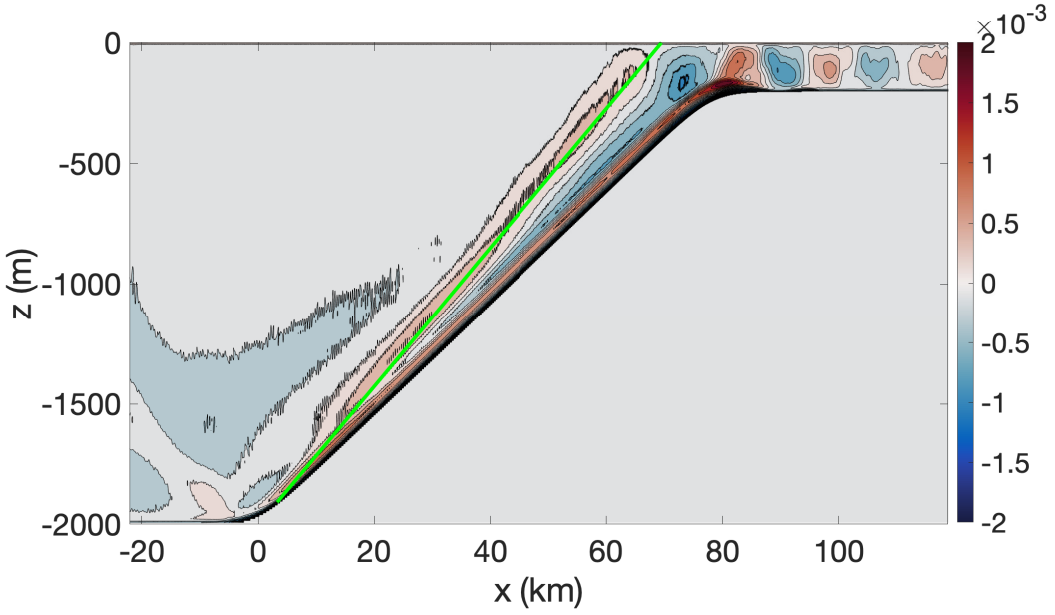

(a)

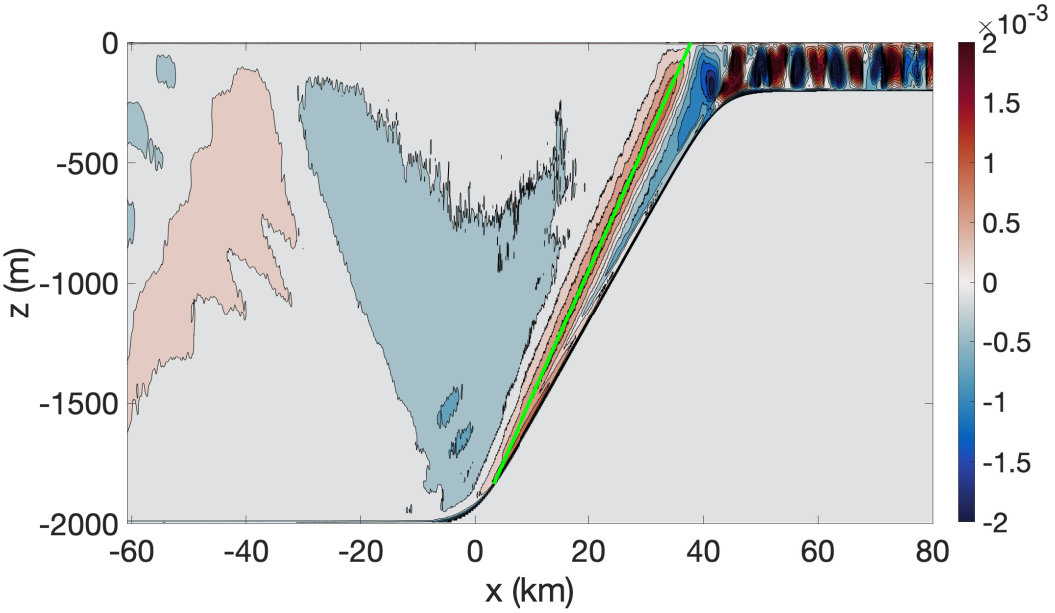

(b)

Figure 1.1: Contour plot of the density perturbation. Wave frequency $\sigma \approx 7.29 \times 10^{-5} s^{-1}$ and $N = 1 \times 10^{-3} s^{-1}$. Upper: $f = 6.7 \times 10^{-5} s^{-1}$. Lower: $f = 5.0 \times 10^{-5} s^{-1}$. Green lines mark the IW beam.

boundary currents are found at the west side of ocean and are usually stronger than eastern boundary currents. Examples of western boundary currents include the Kuroshio current and the Gulf stream, which is one of the most intensively studied current systems in the world.

In the presence of a current $\vec{U}$ which varies slowly compared with the IW wavelengths, the wave frequency of IWs propagating into a geostrophic current is $\sigma = \sigma_{intrinsic} + \vec{k} \cdot \vec{U}$. Here $\vec{k} \cdot \vec{U}$ is the Doppler shift and $\sigma_{intrinsic}$ is the intrinsic frequency of the wave, which is defined as the wave frequency in the reference frame moving with the geostrophic current. The wave frequency σ remains constant throughout the wave propagation, but the intrinsic frequency $\sigma_{intrinsic}$ can change according to the geostrophic current.

If we consider a steady geostrophic current $\vec{U} = (0, V_g(x, z), 0)$, the momentum equation is simplified to

$$-fV_g = -(p_g)_x, \tag{1.55}$$
$$0 = -(p_g)_z - \rho_g g. \tag{1.56}$$

Here p_g and ρ_g are the pressure and density field associated with the geostrophic current. The two equations above yield the thermal wind relation:

$$f(V_g)_z = -(\rho_g)_x g. \tag{1.57}$$

The vertical shear of a geostrophic current is balanced by a corresponding horizontal density gradient. Note when we have a barotropic current $V_g(x)$, there is no horizontal varying density gradient associated with the current, $\rho_g = 0$.

Consider two dimensional waves normally incident on the current so $\vec{k} \cdot \vec{U} = 0$. The linearized governing equations are

$$u_t - fv = -p_x, \tag{1.58}$$
$$v_t + fu + u(V_g)_x + w(V_g)_z = 0, \tag{1.59}$$
$$\epsilon_{nh} w_t = -p_z - \rho g, \tag{1.60}$$
$$\rho_t + u(\rho_g)_x - w\frac{N^2}{g} = 0, \tag{1.61}$$
$$u_x + w_z = 0, \tag{1.62}$$

where $\epsilon_{nh} = 1$ for non-hydrostatic and 0 for hydrostatic approximations. Second order gradients of the current are usually ignored in deriving the intrinsic frequency. The w-equation in (1.15) now becomes [Mooers, 1975],

$$\left(\epsilon_{nh} w_{xx} + w_{zz}\right)_{tt} + N^2 w_{xx} + f_{eff}^2 w_{zz} - 2f(V_g)_z \cdot w_{xz} = 0, \tag{1.63}$$

and the dispersion relation is

$$\sigma^2 = \sigma^2_{intrinsic} = \frac{f^2_{\mathit{eff}} - 2f(V_g)_z \cdot \epsilon + N^2\epsilon^2}{1 + \epsilon_{nh} \cdot \epsilon^2}, \tag{1.64}$$

where f_{eff} is the effective frequency given by $f^2_{\mathit{eff}} = f^2 + f(V_g)_x$. The wave frequency is real and there is no energy exchange between the current and the IWs. If the second order gradients are included in the calculation, we will have an imaginary part added to (1.64), which indicates energy transfer. Note if the current is barotropic, $(V_g)_z = 0$ and the dispersion relation here (1.64) is identical to the earlier one without the current (1.47) except that f has been replaced by f_{eff}. The lower bound of the freely propagating IWs is now f_{eff} instead of f. Kunze [1985] provides the expression of intrinsic frequency for three dimensional IWs propagating into the current. He predicted the trapping of NIWs in regions of negative (positive) relative vorticity in the northern (southern) hemisphere and identified the amplification of NIWs near the vertical critical layer. In this set up, if we consider an eddy (U_e, V_e, W_e) modelled by a rotating solid body, $f_{eff} = f + \frac{\zeta}{2}$, where $\zeta = (V_e)_x - (U_e)_y$ is the vertical vorticity. If the reference frame moves with the eddy, $f_{eff} = f + \zeta$. This is because half the vorticity contribution is hidden in the Doppler shift term in the previous formulation with Earth as the reference frame. The derivation is tedious and omitted here.

1.3 Energetics

The goal of this section is to derive the barotropic to baroclinic energy conversion rate using the fully nonlinear governing equations 1.1 to 1.3. This lays the foundation of the IW generation mechanism from tide-topography interactions, which is the main focus in Chapter 4. We make the hydrostatic approximation in the derivation.

1.3.1 Definitions and assumptions

The overbar of some quantity ϕ refers to the depth integral unless otherwise stated:

$$\bar{\phi} = \int_{-h}^{0} \phi dz. \tag{1.65}$$

The total flow field is divided into

$$\mathbf{u_{tot}} = (u_{tot}, v_{tot}, w_{tot}) = (U + u, V + V_g + v, W + w), \tag{1.66}$$

$$\rho_{tot} = \rho_0\big(\rho_b(z) + \rho_g + \rho(x, z, t)\big), \tag{1.67}$$

$$p_{tot} = \rho_0\big(p_b(z) + p_g(x, z) + p_{bt}(x, z, t) + p(x, z, t)\big), \tag{1.68}$$

where $\mathbf{U} = (U, V, W)$ is the flow field associated with the barotropic tidal currents defined as

$$U(x,t) = \frac{1}{h(x)} \int_{-h}^{0} u_{tot}\, dz, \tag{1.69}$$

$$V(x,t) = \frac{1}{h(x)} \int_{-h}^{0} v_{tot} - V_g\, dz, \tag{1.70}$$

$$\begin{aligned} W(x,z,t) &= \int_{-h}^{z} W_z dz + W|_{z=-h}, \\ &= \int_{-h}^{z} -U_x\, dz - Uh', \\ &= -U_x(z+h) - Uh', \\ &= -U_x z, \qquad \textit{(Rigid lid)} \end{aligned} \tag{1.71}$$

where $h' = dh/dx$. ρ_0 is the reference density. $\rho_b(z)$ is the background density field in hydrostatic balance with $p_b(z)$. $p_g(x)$, given by $\partial p_g/\partial x = fV_g$, is the pressure associated with the geostrophic current V_g. We take $p_g = 0$ to the left of the current. $\rho(x, z, t)$ is the density perturbation in hydrostatic balance with $p_{bt} + p$. p_{bt} and p are the barotropic and baroclinic pressure, respectively. We assume p has zero depth average (Kunze et al. [2002]), i.e. $p = (p_{tot} - p_b) - \frac{1}{h(x)}\overline{(p_{tot} - p_b)}$. ρ is assumed to be the baroclinic density perturbation [Kang and Fringer, 2012]. $\mathbf{u} = (u, v, w)$ is the flow field associated with the internal waves. Here we assume the energy exchange between the current and the wave field is negligible and V_g does not vary with time because the tidal current is small and the tidal advection $U(V_g)_x$ is negligible. Here we use barotropic currents to discuss the energetics because there is no complication in the available potential energy (APE) and this is the simplest way to study the effects of horizontal shear of the background current without additional complications of horizontally varying stratification. $(0, V_g(x), 0)$ is the barotropic geostrophic current, which is in geostrophic balance with ρ_g and $p_g(x)$. Since the current is barotropic, $\rho_g = 0$. We make the hydrostatic approximation so that the kinetic energy of the flow only comes from the horizontal velocities. The detailed assumption about the APE is discussed in the following section.

Available potential energy equation

From the total density equation 1.8, we can get the total potential energy (PE) equation

$$\frac{DE_p}{Dt} = \rho_{tot} g w_{tot} + \rho_o D_p, \tag{1.72}$$

where $E_p = \rho_{tot} g z$ is the total potential energy per unit area. In practice, we are often concerned about the APE instead of the PE because APE is the maximum amount of PE that can be converted into KE, while PE alone does not provide this information. We obtain the APE through the APE density Lamb [2008],

$$E_a(x, z, t) = g \int_z^{z^*(x,z,t)} \big(\rho_r(s) - \tilde{\rho}(x, z, t)\big)\, ds \tag{1.73}$$

where $z^*(x, z, t)$ is the original height of the fluid parcel at (x, z) at time t. ρ_r is the relaxed unperturbed density which gives the minimum potential energy. $\tilde{\rho}$ is the total density of the wave field. If we set $\rho_r = \rho_b(z)$ (or by sorting the density field), we can have the APE equation for the total wave field. Since $\frac{Dz^*}{Dt} = 0$, applying the density equation 1.8 gives

$$\frac{DE_a}{Dt} = \rho g w_{tot} - \epsilon_a, \tag{1.74}$$

where E_a is the APE density for the total wave field, $\epsilon_a = g(z^* - z)D_p$ is the dissipation rate of the APE. Note this formulation of APE is only valid if the reference density ρ_r is a function of z only and $\rho_g = 0$. This is one of the reasons we choose to have a barotropic geostrophic current. If we have a geostrophic baroclinic current, we cannot use 1.73 to calculate the APE inside of the current. In fact, if the reference density $\rho_r(x, z)$ has a non-zero horizontal gradient, the issue of determining the APE is still controversial (Tailleux [2018]). This is because an approriate reference density is ambiguous. For example, a horizontally varying reference density $\rho_r(x, z)$ can further release potential energy and result in a different reference density. Even if we assume the reference density is the initial density $\rho_b(z) + \rho_g(x, z)$, a positive definite APE density is difficult to find. Codoban and Shepherd [2003] tackled this problem and proposed a new formulation using momentum constraints, but the equations are too complicated to be used in practice.

Throughout our work, we follow the work of Kang [2010] that all the APE is contained in the baroclinic waves, and assume there is no APE associated with the barotropic tide. Intuitively when we set the horizontal tidal flow $U \propto \cos(\sigma t)$, the APE averaged over one tidal period is approximately 0. Since we assume V_g is independent of time, this

indicates that the current does not lose or gain energy. We take $\rho_r = \rho_b(z)$ so that the APE associated with the baroclinic waves is given as

$$E'_a = g \int_z^{z^*(x,z,t)} (\rho_b(s) - \rho_b(z) - \rho(x,z,t))\, ds. \tag{1.75}$$

Using $\frac{Dz^*}{Dt} = 0$ and (1.8), the total derivative of E'_a is

$$\frac{DE'_a}{Dt} = \rho g(W + w) - \epsilon_a. \tag{1.76}$$

1.3.2 Boundary conditions

We apply a rigid lid on the surface $z = 0$

$$w_{tot}(x, z = 0) = 0, \tag{1.77}$$
$$W(x, z = 0) = 0, \tag{1.78}$$
$$w(x, z = 0) = 0. \tag{1.79}$$

There is no flow penetrating the bottom bathymetry $z = -h(x)$.

$$W|_{-h} = -Uh', \tag{1.80}$$
$$w|_{-h} = -uh'. \tag{1.81}$$

1.3.3 Properties

In order to derive the energy equations, we will use the following properties:

- $\bar{u} = \bar{v} = 0$. Note $\overline{w} \neq 0$.
- $U_z = V_z = 0$.
- $W_{zz} = -U_{xz} = 0$.

- For any quantity $A = u, v$, we have

$$\begin{aligned}\overline{UA_x} + \overline{WA_z} &= \int_{-h}^{0} UA_x + WA_z dz, \\ &= \Big(U\big(\frac{d}{dx}\big(\int_{-h}^{0} A dz\big) - A|_{-h}h'\big) - WA|_{-h} - \int_{-h}^{0} W_z A dz\Big), \\ &= \Big(0 - UA|_{-h}h' + UA|_{-h}h' + \int_{-h}^{0} U_x A dz\Big), \\ &= 0.\end{aligned} \tag{1.82}$$

-

$$\begin{aligned}U \cdot \overline{(p_s + p)_x} &= U \int_{-h}^{0} (p_s + p)_x \, dz, \\ &= \frac{d}{dx}\big(U \int_{-h}^{0} (p_s + p)\, dz\big) - U_x \int_{-h}^{0} (p_s + p)\, dz - U(p_s + p)|_{-h}h', \\ &= \frac{d}{dx}(U\overline{p_s + p}) + \int_{-h}^{0} W_z(p_s + p)\, dz + \big(W(p_s + p)\big)|_{-h}, \\ &= \frac{d}{dx}(U\overline{p_s + p}) - \int_{-h}^{0} W(p_s + p)_z \, dz, \\ &= \frac{d}{dx}(U\overline{p_s + p}) + \int_{-h}^{0} \rho g W \, dz, \\ &= \frac{d}{dx}(U\overline{p_s + p}) + \overline{\rho g W}.\end{aligned} \tag{1.83}$$

- For any quantity A, we have

$$\begin{aligned}\nabla_H \cdot \overline{(u, v) \cdot A} &= \frac{d}{dx}\Big(\int_{-h}^{0} u \cdot A \, dz\Big), \\ &= \int_{-h}^{0} (u \cdot A)_x \, dz + (uA)|_{-h}h', \\ &= \int_{-h}^{0} (u \cdot A)_x \, dz - (wA)|_{-h}, \\ &= \int_{-h}^{0} (u \cdot A)_x \, dz + \int_{-h}^{0} (w \cdot A)_z \, dz, \\ &= \overline{\nabla \cdot (\mathbf{u}A)}.\end{aligned} \tag{1.84}$$

1.3.4 Energy equations

We begin with the hydrostatic Navier-Stokes equations in two dimensional settings.

$$\frac{\partial}{\partial t}(U+u)+(U+u)(U+u)_x+(W+w)(U+u)_z-f(V+V_g+v) \tag{1.85}$$
$$=-(p_g)_x-(p_s)_x-p_x+D_1,$$
$$\frac{\partial}{\partial t}(V+v)+(U+u)(V+V_g+v)_x+(W+w)(V+V_g+v)_z+f(U+u)=D_2, \tag{1.86}$$
$$-(p_g)_z-p_z-\rho_g g-\rho g=0, \tag{1.87}$$

where the viscosity terms are

$$D_1=(\nu_H(U+u)_x)_x+(\nu_z(U+u)_z)_z, \tag{1.88}$$
$$D_2=(\nu_H(V+V_g+v)_x)_x+(\nu_z(V+V_g+v)_z)_z. \tag{1.89}$$

We take the dot product between the momentum equations and the total velocity $\mathbf{u_{tot}}$, producing

$$\frac{D}{Dt}E_k+\nabla\cdot\big(\mathbf{u_{tot}}(p_g+p_s+p)\big)=-(\rho+\rho_g)gw_{tot}+D, \tag{1.90}$$

where the kinetic energy for the total wave field is

$$E_k=\frac{1}{2}\big(u_{tot}^2+v_{tot}^2\big). \tag{1.91}$$

We re-arrange D to get the dissipation rate.

$$D=u_{tot}D_1+v_{tot}D_2, \tag{1.92}$$
$$=\nabla_H\cdot\big(\nu_H\nabla_H E_k\big)-\epsilon_k,$$

where $\nabla_H=\frac{\partial}{\partial x}$, $\nabla_H\cdot\big(\nu_H\nabla_H E_k\big)$ is the dissipation flux. The dissipation rate ϵ_k of the kinetic energy is

$$\epsilon_k=\nu_H\nabla_H\mathbf{u_{tot}}\cdot\nabla_H\mathbf{u_{tot}}-\mathbf{u_{tot}}\cdot(\nu_V(\mathbf{u_{tot}})_z)_z. \tag{1.93}$$

Now we add 1.90 and 1.74 together,

$$\frac{D}{Dt}(E_k+E_a)+\nabla\cdot\big(\mathbf{u_{tot}}(p+p_g+p_s)\big)-\nabla_H\cdot\big(\nu_H\nabla_H E_k\big)=-\epsilon_k-\epsilon_a, \tag{1.94}$$

where $\epsilon_k+\epsilon_a$ is the total dissipation rate.

Barotropic energy equation

The derivation of the barotropic energy equation is motivated by the work of Kang [2010]. We take the vertical average of 1.85 and 1.86 and apply the thermal wind relation,

$$U_t + UU_x + \frac{1}{h}\Big(\overline{Uu_x} + \overline{uu_x} + \overline{Wu_z} + \overline{wu_z}\Big) - fV = \frac{1}{h}\Big(- \overline{(p_s + p)_x} + \overline{D}_1\Big), \tag{1.95}$$

$$V_t + UV_x + \frac{1}{h}\Big(\overline{Uv_x} + \overline{uv_x} + \overline{Wv_z} + \overline{wv_z} + \overline{G}_1\Big) + fU = \frac{1}{h}\Big(\overline{D}_2\Big), \tag{1.96}$$

where $\overline{G}_1 = \overline{u_{tot}(V_g)_x + w_{tot}(V_g)_z}$. Apply 1.82 to the equations above, they simplify to

$$U_t + UU_x + \frac{1}{h}\Big(\overline{uu_x} + \overline{wu_z}\Big) - fV = \frac{1}{h}\Big(- \overline{(p_s + p)_x} + \overline{D}_1\Big), \tag{1.97}$$

$$V_t + UV_x + \frac{1}{h}\Big(\overline{uv_x} + \overline{wv_z} + \overline{G}_1\Big) + fU = \frac{1}{h}\Big(\overline{D}_2\Big). \tag{1.98}$$

Multiply $(U, V)h$ to 1.97, 1.98, and apply 1.83 after summing the two equations up, we have the kinetic energy equation for the barotropic currents,

$$(hE_{hk})_t + \nabla_H \cdot (\mathbf{U}_H \cdot hE_{hk}) + \nabla_H \cdot (\mathbf{U}_H \cdot \overline{p_s + p}) + G_{bt} = -\overline{C} - \overline{D}_{bt}. \tag{1.99}$$

Here $E_{hk} = \frac{1}{2}(U^2 + V^2)$ is the kinetic energy of the barotropic tides. $G_{bt} = V\overline{G}_1$ forms part of the energy flux associated the geostrophic current. $\overline{\mathbf{U}}_H = (U, V)$ is the horizontal barotropic velocity. $\overline{D}_{bt} = U\overline{D}_1 + V\overline{D}_2$ is related to the dissipation. The vertical average of the conversion rate from barotropic to baroclinic energy is

$$-\overline{C} = -\overline{\rho g W} - C_1, \tag{1.100}$$

where

$$C_1 = U\big(\overline{uu_x} + \overline{wu_z}\big) + V\big(\overline{uv_x} + \overline{wv_z}\big). \tag{1.101}$$

Baroclinic energy equation

We subtract the barotropic components 1.95 and 1.96 from the total momentum equations 1.85 and 1.86,

$$u_t + (U + u)u_x + (W + w)u_z + uU_x - fv = -(p_s + p)_x + \overline{(p_s + p)_x} \tag{1.102}$$
$$+\overline{uu_x} + \overline{wu_z} + D_1 - \overline{D}_1,$$

$$v_t + (U + u)v_x + (W + w)v_z + uV_x + (G_1 - \overline{G}_1) + fu = \overline{uv_x} + \overline{wv_z} + D_2 - \overline{D}_2. \tag{1.103}$$

Multiply the two horizontal momentum equations 1.102, 1.103 and the density equation 1.87 by the baroclinic velocity (u, v, w), then we sum the three equations up,

$$(E'_k)_t + \nabla \cdot (\mathbf{u_{tot}} \cdot E'_k) + \nabla \cdot \big(\mathbf{u} \cdot (p_s + p)\big) + \nabla_H \cdot (u \cdot E'_{k0}) + G_{bc} = -\rho g w + C_2 + D_{bc}, \tag{1.104}$$

where $E'_k = \frac{1}{2}(u^2 + v^2)$ is the kinetic energy of the baroclinic tides. $G_{bc} = v \cdot (G_1 - \overline{G}_1)$ forms part of the energy flux associated with the current. $D_{bc} = u(D_1 - \overline{D}_1) + v(D_2 - \overline{D}_2)$ is related to the dissipation. C_2 will be part of the conversion rate.

$$C_2 = 2Uuu_x + V(uv)_x + u\overline{(p_s + p)_x} + u(\overline{uu_x} + \overline{wu_z}) + v(\overline{uv_x} + \overline{wv_z}). \tag{1.105}$$

$E'_{k0} = Uu + Vv$ is defined as the cross energy. One way to understand this is through the total kinetic energy:

$$\frac{1}{2}[(U+u)^2 + (V+v)^2] = \frac{1}{2}(U^2 + V^2) + \frac{1}{2}(u^2 + v^2) + (Uu + Vv), \\ = E_{hk} + E'_k + E'_{k0}. \tag{1.106}$$

Since $\int_{-h}^{0} E'_{k0} = 0$, this cross energy does not contribute towards the energy budget. We now add the APE equation 1.76 to 1.104 to obtain the total energy for the baroclinic waves,

$$(E'_k + E'_a)_t + \nabla \cdot (\mathbf{u_{tot}}(E'_k + E'_a)) + \nabla \cdot \big(\mathbf{u}(p_s + p)\big) + \nabla_H \cdot (\mathbf{u_H} E'_{k0}) + G_{bc} = \rho g W + C_2 + D_{bc} + D_a, \tag{1.107}$$

where $D_a = g \int_z^{z^*(x,z,t)} u_{tot}(\rho_g)_x \, ds - \epsilon_a$. Now we vertically average 1.107 and apply property 1.84 we have

$$(\overline{E'_k} + \overline{E'_a})_t + \nabla_H \cdot \big(\overline{(\mathbf{u_{tot}})_\mathbf{H}(E'_k + E'_a)}\big) + \nabla_H \cdot \big(\overline{\mathbf{u_H} p}\big) + \nabla_H \cdot \big(\overline{\mathbf{u_H} E'_{k0}}\big) = \overline{C} + \overline{D_{bc} + D_a - G_{bc}}, \tag{1.108}$$

The vertical integration of conversion rate $\overline{C}$ from barotropic to baroclinic is the same as 1.100 derived in the barotropic energy section. To summarize, the vertical barotropic to baroclinic conversion rate is

$$\overline{C}(x,t) = \overline{\rho g W} + C_1 = \overline{\rho g W} + \overline{C_2}. \tag{1.109}$$

The toal conversion rate can be obtained by simply integrating $\overline{C}(x,t)$ over x. This is my primary quantity used to determine the IW conversion rate later in Chapter 4.

1.4 Literature review

Studies on internal tides (ITs) have attracted considerable attention over the years, because these waves can have a significant impact on oceanic mixing [Munk and Wunsch, 1998, Vic et al., 2019], large scale ocean circulation [Wunsch and Ferrari, 2004], transport of energy [Simmons and Alford, 2012], upwelling of nutrients [Schafstall et al., 2010] and shaping the continental shelves [Cacchione et al., 2002]. In situ observations suggest that strong mixing occurs over rough bathymetry [Polzin et al., 1997], the biweekly variation of the mixing indicating a relationship to the spring-neap barotropic tidal cycle, and thus to the conversion of barotropic to baroclinic tidal energy. The most prominent IT generation mechanism is barotropic tidal flows incident upon bottom topography such as the continental shelf slope, subsurface ridges and seamounts. Examples of generation locations include the Bay of Biscay [New and Pingree, 1992, Gerkema et al., 2004], the Australian North West shelf [Holloway et al., 2001], the Malin-Hebrides Shelf [Xing and Davies, 1998], the Hawaiian Ridge [Martin et al., 2006], Mid-Atlantic Ridge [Zilberman et al., 2009], Monterey Bay [Lien and Gregg, 2001] and various seamounts [Lueck and Mudge, 1997, Toole et al., 1997]. Global numerical simulations [Niwa and Hibiya, 2011, Simmons et al., 2004] have been conducted to investigate the spatial distribution of the major generation sites. They found that the generation of baroclinic tides largely occurs over prominent topographic features and the total conversion rate increases as the model grid spacing is reduced.

1.4.1 IT generation

There are three important dimensionless parameters relevant to internal waves (IWs) generated by tide-topography interaction. The first one is the tidal excursion parameter ϵ, which is used to measure the nonlinearity of the waves [Vlasenko et al., 2005, Legg and Huijts, 2006, Garrett and Kunze, 2007]. It is defined as the ratio of the barotropic tidal advection distance to the horizontal scale of the topography. If ϵ is much smaller than 1, linear ITs are generated mainly at the forcing frequency. The second dimensionless parameter is the relative height of the topography $\delta = h/H$, where h is the topographic height and H is a typical water depth. The third important parameter for IT generation is the bottom slope criticality

$$\alpha = s/\gamma, \tag{1.110}$$

where s is the topographic slope and γ is the slope of an IT characteristic. In the presence of a barotropic background flow $V(x)$ in the y-direction which varies slowly in the x direction

so that second-order gradients are negligible and under the hydrostatic approximation,

$$\gamma = \sqrt{\frac{\sigma_T^2 - f_{eff}^2}{N^2}}. \tag{1.111}$$

Here $f_{eff}^2 = f^2 + fV_x$ is the effective Coriolis frequency squared [Mooers, 1975], σ_T is the IT frequency and N is the buoyancy frequency. In general N is a function of z and γ can depend on both x and z.

The critical latitude is defined as the latitude where $f = \sigma_T$ for each tidal constituent. Critical latitudes are around 30° and 75° for the diurnal K_1 and semi-diurnal M_2 tides, respectively. Note that, assuming $N > f_{eff}$, (1.111) is not valid if $f_{eff} > \sigma_T$ or $\sigma_T > N$. Instead we have an evanescent region, where no freely propagating waves are permitted and forced waves decay quasi-exponentially away from the generation site. If the length of the evanescent region is finite, meaning f_{eff} varies spatially, a fraction of the wave energy can tunnel through the region and there is a radiated wave on the other side of the region. This process is termed tunnelling. Intensive research on tunnelling has been done with most of it focused on vertically propagating waves in the atmospheric context [Jones, 1970, Monserrat and Thorpe, 1996, Sutherland and Yewchuk, 2004], though some work has discussed tunnelling in the ocean [Eckart, 1961, Rainville and Pinkel, 2004].

Unlike numerical studies, the theoretical models all use linearized equations of motion, and most of them are formulated without a background current, i.e. $f_{eff} = f$. When α is much less than 1, the analysis in Bell Jr [1975] has been widely used for small amplitude bathymetry $\delta \ll 1$. Bell included the advection by the background flow and used an infinitely deep ocean to estimate the upward energy flux for subcritical topography to be O(1) mW m^{-2}. Building upon Bell's work, Khatiwala [2003] included a rigid lid, which results in horizontal, rather than vertical, energy flux. He found good agreement with that predicted by a nonlinear numerical model. Llewellyn Smith and Young [2002] too present an analytical treatment of this problem by using a different mathematical approach (WKB method) to include non-uniform $N(z)$. While most models with small bathymetry $\delta \ll 1$ used a linearized bottom boundary condition, St. Laurent and Garrett [2002] used a perturbation expansion of the bottom boundary condition for small but finite amplitude topography. However, the linear theory in general underestimates the energy flux for supercritical cases.

Bathymetries with large amplitudes have also been considered theoretically. In this case, the bottom boundary condition cannot be linearized. For subcritical slopes with $\alpha < 1$ the model developed by Baines [1982] is available. Craig [1987] used method of

characteristics and described the generation of ITs of a single frequency at shelf-like topography with a constant shelf slope. He found that energy flux varies linearly with α and like α^5 for supercritical and subcritical cases, respectively. Similar results for subcritical cases were obtained by Vlasenko et al. [2005]. Balmforth et al. [2002] considered an infinitely deep ocean, while a finite depth ocean was discussed in St. Laurent et al. [2003] with a finite amplitude knife edge, step-like and top hat bathymetry. This work was extended by Nycander [2006], where he considered periodic knife edge bathymetry. Pétrélis et al. [2006] applied a Green's function to large submarine ridges assuming small tidal excursion distance ϵ. Their results confirm a monotonic increase in the radiated energy flux as the slope becomes steeper, with most of the increase happening after the slope becomes slightly supercritical. Other models include those of Gerkema [2002], Gerkema et al. [2004] and Baines [1973]. However, none of these models on large amplitude bathymetries include advection by the barotropic tide and they generally need to be solved numerically due to the model complexity. Hence they are restricted to small tidal excursions.

Numerical simulations using primitive equation models to study IT generation by tide-topography interaction have become increasingly important particularly for regions where linear theories break down or become complex. Legg and Huijts [2006] used a Gaussian ridge to confirm that strong local mixing only occurs for narrow features with large α, which is common in the coastal ocean. Holloway and Merrifield [1999] and Munroe and Lamb [2005] focused on idealized seamounts and showed that large seamounts are ineffective at generating ITs unless they are elongated in a direction normal to the barotropic tides. The aforementioned papers all used free surface in their models, Lamb and Kim [2012] applied a rigid lid and concluded that the large amplitude theory yields good results with simulations using subcritical slopes. Investigations of IT generation using more realistic bathymetries are numerous, e.g., Powell et al. [2012], Niwa and Hibiya [2004, 2014], Merrifield et al. [2001], Holloway [1996] and Zilberman et al. [2009]. More details on the theories and numerical simulations can be found in the review by Garrett and Kunze [2007].

Most of the aforementioned research is relatively basic in the sense that only the effect of barotropic tides and bathymetry is considered in the IW generation process. This paper builds on past work by investigating IT generation over a shelf in the presence of an along-shelf geostrophic current, which is a common feature along continental shelves. Strong oceanic currents, such as the Gulf Stream, Kuroshio, Oyasio, the Pacific Equatorial countercurrent and Davidson Current are a significant source of mass, heat and nutrient transport in the world's oceans [Hall and Bryden, 1982]. The presence of the currents can significantly modify the background density, effective frequencies and velocity field, which in turn modulates the IW field including its propagation path, energy distribution and generation process. Incorporating geostrophic currents into studies of IW generation is

necessary and our knowledge is far from complete. One of the first theoretical studies of IWs propagating into a geostrophic current dates back to Mooers [1975], who investigated two dimensional IWs normally incident on a frontal zone using the method of characteristics. Kunze [1985] extended Mooers' work to a three dimensional setting by considering the influence of mean flow shear on wind generated near-inertial waves (NIWs). Since then research on the impact of currents on ITs, particularly through variations in wave frequency, is still sparse and largely focused on linear equations/theories and some observations [Chuang and Wang, 1981, Kolomoitseva and Cherkesov, 1999, Rainville and Pinkel, 2006, Chavanne et al., 2010, Whitt and Thomas, 2013, Li et al., 2019, Dong et al., 2019]. Richet et al. [2017] investigated the impacts of a weak background current on the local dissipation of high mode IWs using fully nonlinear numerical simulations. Their currents flowed in the same direction as the waves so the wave frequency is affected due to the Doppler shift. The effects of horizontal density variability on the IT wave field with no change in f_{eff} has also been investigated [Vlasenko et al., 2005, Kurapov et al., 2010].

Chapter 4 of this thesis contributes to the understanding of IT generation by including along-shelf barotropic geostrophic currents. Barotropic currents are used because this is the simplest way to study the effects of horizontal shear of the background current giving horizontally varying f_{eff} without additional complications of horizontally varying stratification.

1.4.2 The interaction between ITs and a geostrophic current

Most of the theoretical work on the interaction between internal waves (IWs) and geostrophic currents is based on linear theories. Works by Mooers [1975] and Kunze [1985] have been reviewed in section 1.2.4. Jones [2005] derived a general dispersion relation for IWs in the atmosphere or oceans including all components of baroclinicity, vorticity and rate of strain. Few theoretical studies have included nonlinear effects. Bühler and McIntyre [2005] analyzed the nonlinear interactions between an IW wavepacket and a vortical mean flow with a focus on a pre-wave-breaking scenario termed 'wave capture'. The wave packet extracts energy from the layer-wise two-dimensional shear flow as it propagates through.

A number of numerical studies dedicated to linear IW-mesoscale interactions used ray tracing techniques and linear modal decomposition. The oceanic mesoscale is referred to spatial scales of O(100km). The ray tracing technique traces the paths of wave packets, termed as rays. It uses the Wentzel-Kramers-Brillouin-Jeffreys (WKBJ) approximation, where the wavelength of the wave packet is small compared to the length scale of the background flow. Rainville and Pinkel [2006] used 2D ray tracing to track the path of low-mode

IWs affected by variable topography, stratification and mesoscale barotropic current fields. The influence of the currents became more apparent as the IW mode number increases. Modal coupling and 3D ray tracing were incorporated by Chavanne et al. [2010] to investigate the dynamics of M_2 internal tides (ITs) propagating through idealized mesoscale currents. Their results were consistent with observations despite the lack of scale separation between the IWs and the currents. They also found that ITs can become incoherent with the astronomical forcing even close to their generate sites as a result of mesoscale variability. Dunphy and Lamb [2014] considered mode-one ITs propagating through mesoscale eddies. They found that a barotropic eddy can focus the ITs energy into beamlike patterns, and that a baroclinic eddy scatters the ITs into higher modes with conversion rates up to 13%. Building upon previous analysis, Kelly and Lermusiaux [2016] examined the propagation and generation of a mode-one IT in the presence of a shelfbreak front and the Gulf Stream by including intermodal coupling for arbitrary stratifications. More recently Li et al. [2019] considered the reflection and transmission of IWs normally incident on a 2D geostrophic front. They revisited the classical linear wave equation and converted it to a canonical PDE, recovering the properties of the conventional IW theory in the absence of a current.

The presence of geostrophic currents can significantly modify the background density and velocity field, which in turn modulates the IW field including its propagation path, energy distribution and generation process. Figure 1.2 demonstrates the effects of a current on deforming the total density field. Chuang and Wang [1981] investigated the influence of a shelfbreak front on the propagation and generation of ITs. They concluded that when the slope of isopycnals is comparable to the bottom slope, topographic effects can be reduced and redistribution of incident ITs into higher modes becomes more restricted. Following the work of Mooers [1975] and Chuang and Wang [1981], Vlasenko et al. [2005] compared the generation and propagation of ITs through a density front over a ridge and a flat bottom. They used linear governing equations and considered fronts with a linear horizontal density gradient. Their study on a continuous stratification indicated that the width of the frontal zone and the wavelength of the IT are the controlling parameters for the scattering process. Park and Watts [2006] used a geometric optics model to explain the observed refraction of semidiurnal IT beams in the southwestern Japan/East Sea. They found that variations of IT propagation and energy distribution are closely related to the mesoscale circulation. Polzin [2008, 2010] indicated that nonlinear eddy-IW coupling plays an $O(1)$ role in the energy budget of the IW field and is a significant energy sink for mesoscale eddies. The combined effects of wind-driven upwelling and ITs on the central Oregon shelf are studied by Kurapov et al. [2010] using an idealized alongshore uniform setup. They found that variability in stratification associated with upwelling can affect not only the propagation of

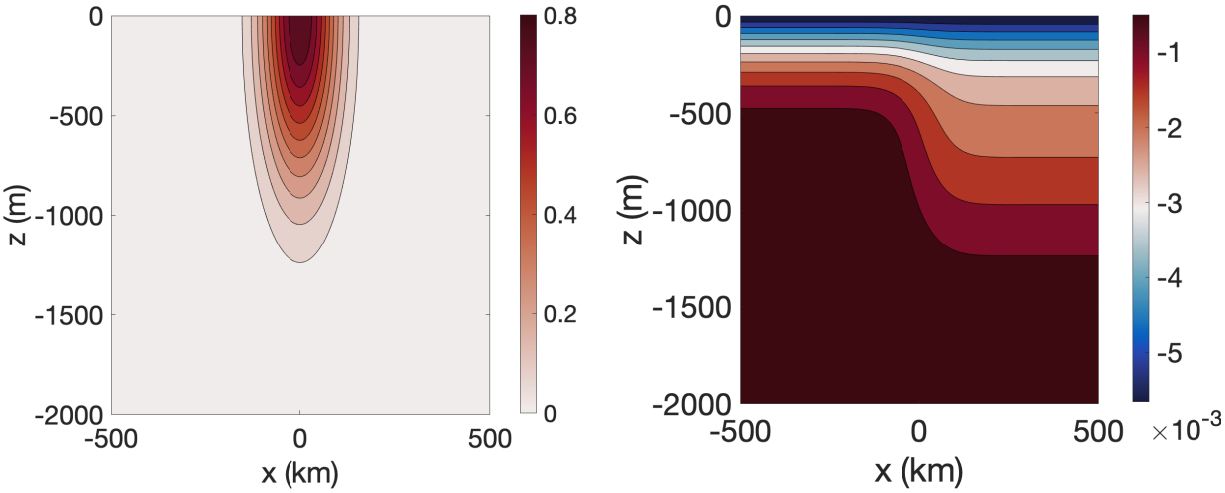

(a) (b)

Figure 1.2: (a) A baroclinic geostrophic current $V(x, z)$ and (b) the total density field in thermal wind balance with it.

ITs, but also the IT generation process by changing the slope criticality. Whitt and Thomas [2013] highlighted a physical interpretation of NIWs propagating into a two dimensional idealized baroclinic geostrophic current using parcel arguments.

1.4.3 Overview

- Chapter 2 introduces the numerical model we will use for the simulations throughout this thesis.
- Chapter 3 studies the effects of a geostrophic current on the propagation of mode-one ITs on a flat bottom.
  - We investigate this problem by carefully varying the current parameters and conducting fully nonlinear numerical simulations. Our parameter space covers typical geostrophic currents in the real oceans.
  - We force an incident mode-one IT on the left boundary that propagates through the current and we investigate the reflection, transmission and the mode conversion from the ITs interacting with the current. We quantify the change of

the ITs wave field through two parameters: the reflection coefficient R and the linear modal energy after the waves propagate through the current.

  - We consider the dispersion relation 1.64 proposed by Mooers [1975]. In general assume $N > max(\sigma, f_{eff})$, three scenarios can happen depending on σ and f_{eff}: 1) if $\sigma > f_{eff}$ everywhere waves can pass through the current; 2) if $f < \sigma < f_{eff}$ in part of the current waves will be partly reflected when propagating across the current; 3) If $\sigma < f$, waves must be generated inside of the current where $f_{eff} < \sigma$ and will be trapped. Chapter 3 of this thesis contributes to the understanding of first two scenarios listed above.

- Chapter 4 studies the effects of an along shelf current on the generation of ITs near the critical latitude.

  - Most of the research on IT generation problem by tide-topography interaction is relatively basic in the sense that only the effect of barotropic tides and bathymetry is considered. Our research is new because we include geostrophic currents into the generation model.
  - The geostrophic current in our work is barotropic instead of baroclinic because it is the simplest way to study the effects of currents without the complications of horizontal density variation.
  - We only studied diurnal tides in this work. However, we expect our conclusion to be relevant for different tidal frequencies.
  - We restrict our attention on near-critical latitudes so that the impact of varying the horizontal shear of the current V_x can be significant. At latitudes far from critical, the current will still modify the wave generation but the effects are expected to be reduced.
  - We assumed $f > 0$, i.e., the Northern Hemisphere in this study. However, our work can be extended to the Southern Hemisphere by simply reversing the signs of f and the current velocity.

- Chapter 5 summaries the results of this thesis.

Chapter 2

MITgcm

We use the MIT General Circulation Model (MITgcm, Marshall et al. [1997]) as our numerical model in this thesis. The MITgcm is designed for studies of the atmosphere, ocean and climate over a wide range of scales. It uses a finite volume method with an Arakawa C grid in the spatial discretization [Arakawa and Lamb, 1977]. The flow (u, v, w) is staggered in space so that the velocity is defined on the center of the interface in the direction it flows, e.g. u is evaluated at the centers of the left and right grid faces, and w is evaluated at the centers of the upper and lower grid faces. We use the 3rd order direct space-time with flux limiting as our advection scheme (code name 33 in MITgcm). It uses the Lax-Wendroff scheme where sufficient diffusion is added to the flux so that the forward-in-time method is stable. This scheme is third order in time. The flux limiter is the Sweby limiter [Alistair et al., 2018].

2.1 Model equations

The MITgcm allows us to make the f-plane approximation in which case the model equations are:

$$\frac{D\vec{u}_h}{Dt} + f\hat{k} \times \vec{u}_h = -\frac{1}{\rho_0}\nabla_h p + \vec{F}, \tag{2.1}$$

$$\epsilon_{nh}\frac{Dw}{Dt} = -\frac{1}{\rho_0}\nabla_z p - \frac{\rho_a}{\rho_0}g + \epsilon_{nh}F_w, \tag{2.2}$$

$$\nabla_h \cdot \vec{u}_h + w_z = 0, \tag{2.3}$$

$$\rho_a = \rho_{tot}(\theta, S, p) - \rho_0, \tag{2.4}$$

$$\frac{D\theta}{Dt} = F_\theta, \tag{2.5}$$

$$\frac{DS}{Dt} = F_S, \tag{2.6}$$

where $\vec{u}_h$ is the horizontal velocity vector, w is the vertical velocity, ρ_0 is a constant reference density, f is the Coriolis parameter, p is the perturbed pressure, F and F_w are the horizontal and vertical momentum forcings. ρ_a and ρ_{tot} are the density anomaly and total density. S is salinity, θ is the potential temperature. F_S and F_θ are the salinity and temperature forcings, respectively. The forcing terms here include contributions from viscosity and diffusivity.

In our simulations, we adopt the hydrostatic equation by setting $\epsilon_{nh} = 0$. MITgcm reads in the temperature and salinity profiles initially and computes the density field by evaluating the equation of state (EOS). We choose linear EOS throughout the simulations.

$$\rho(\theta, S, p) = \rho_0(-t_\alpha(\theta - \theta_0) + \beta(S - S_0)). \tag{2.7}$$

Here t_α and β are the thermal and haline expansion coefficients, θ_0 and S_0 are constant reference values for temperature and salinity, respectively. We hold salinity constant, temperature is the active tracer. We set $\rho_0 = 1028kg/m^3$, $\beta = 0$ and $t_\alpha = 2 \times 10^{-4}\,{}^\circ C^{-1}$. Note our focus is on the buoyancy frequency squared $N^2 = -\frac{g}{\rho_0}\frac{d\rho}{dz}$, and it does not matter if salinity or temperature is the tracer. For simulations in chapter 3, viscosity and diffusivity are neglected. For simulations in chapter 4, both viscosity and diffusivity are implemented. Refer to section 4.1 for more details.

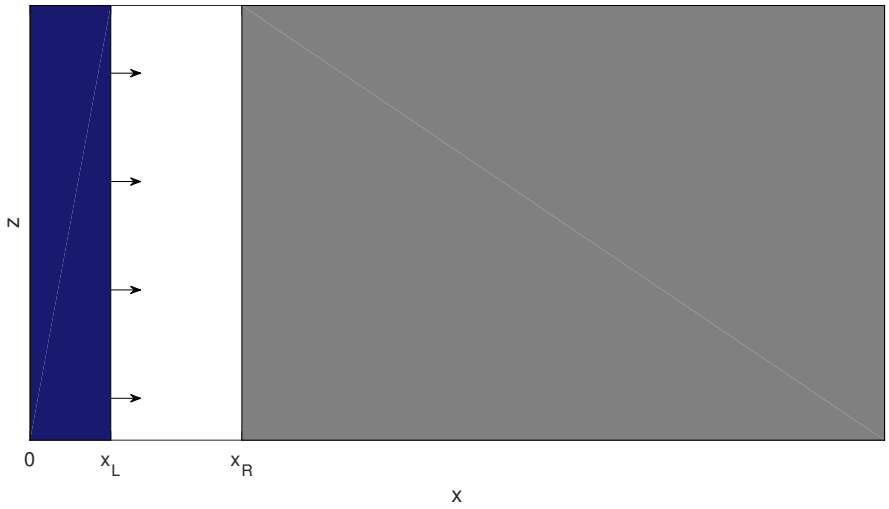

Figure 2.1: A schematic plot of the whole computational domain. The dark blue area is a combination of the stretched grids and the non-zero mask M_{rbc}. The gray area is the stretched grid on the right. The arrows represent the forcing of the linear waves. The wave is forced at $x = x_L$ and the domain of interest is $[x_L, x_R]$.

2.2 Computational domain and geometry

The model uses z-coordinates for the ocean. It is a rectangular domain of dimensions $N_x \times N_y \times N_z$ with a rigid lid at the surface. We pick $N_y = 1$ since we use a two-dimensional setting. The water depth is $h(x)$. In chapter 3, we use a flat bottom with $h(x) = 2$ km. Two extra layer of stretched grids are added to the left and the right side of the domain, where the grids are slowly stretched horizontally with a ratio of 0.5 %. A 2D plot of the domain is given in Figure 2.1. Refer to section 3.1 for more details on the values of the parameters. In chapter 4, we model a linear continental slope. Refer to section 4.1 for more details.

2.3 Restoring boundary condition

In chapter 3, we use the restoring boundary condition package 'rbcs' in the MITgcm to force the internal waves into the domain. This package provides the flexibility to either relax or restore fields in any three dimensional location, so it can be used as a sponge layer

to absorb waves or a source to generate waves. For any variable S (U/V/T) at every grid point, rbcs package replaces the time derivatives by adding a forcing term, where $\frac{DS}{Dt} = F$ is replaced by

$$\frac{DS}{Dt} = F - \frac{M_{rbcs}}{\tau_S}(S - S_{rbc}). \tag{2.8}$$

Here $M_{rbc}(x, y, z)$ is a 3D mask function with values from 0 to 1. 1 indicates maximum forcing and 0 indicates no forcing. τ_S is the relaxing timescale, which usually needs to be greater than the computational time step to maintain the numerical stability. The variable S is restored to S_{rbc}. For example, forcing a linear mode-1 wave at the location (x_L, y, z) sets

$$u(x_L, y, z, t) = S_{rbc}(y, z, t) = \tilde{A}\sin(\sigma t + \phi)\cos(\frac{\pi z}{H}), \tag{2.9}$$

where $\tilde{A}$ is the amplitude of the horizontal velocity. The waves are propagating from left to right, M_{rbc} linearly increases from 0 to 1 in the left patch of stretch grids.

$$M_{rbc}(x, y, z) = x/x_L, \qquad x \leq x_L, \tag{2.10}$$

$$= 0, \qquad otherwise. \tag{2.11}$$

The varying M_{rbc} acts like a sponge layer to damp out the waves propagating to the left due to the forcing. For $x \geq x_R$, the stretched grid alone is enough to absorb all the incoming waves so $M_{rbc} = 0$.

2.4 Open boundary conditions

Unlike 'rbcs' which can be used to restore or relax the field in the entire domain, 'obcs' is an explicit package for open boundary conditions.

In chapter 3, apart from the package 'rbcs', we also use the open boundary conditions package 'obcs' where we choose the western and eastern boundaries to be closed.

In chapter 4, we use 'obcs' to force a barotropic tide at the left boundary. With the implementation of the rigid lid, once the barotropic tide is forced it is felt everywhere in the domain. 'rbcs' package is not needed here. We need 'rbcs' in chapter 3 because there are two layers of stretched grids added to the left and the right side of the boundaries, and the forcing of IWs need to be inside the domain. If IWs are forced at the boundaries, the waves will be damped out. Forcing barotropic tides with a rigid lid does not have this problem. For more details on the barotropic tidal forcing, refer to section 4.1.

Chapter 3

Mode-one linear waves propagating across a geostrophic current

3.1 General set-up

We start our investigation by looking at flat bottom cases with water depth $H = 2000$ m in a two-dimensional inviscid environment. We consider a simple mode-one IT propagating from the left into a geostrophic current. Our boundary forcing is designed to drive a mode-one IW with horizontal velocity $u = \tilde{A}\sin(kx - \sigma \cdot t) \cdot \phi_z(z)$, where $\phi_z(z)$ has been scaled so that $\int_{-H}^{0}(\frac{d\phi}{dz})^2\, dz' = 1$. The amplitude of the wave is the surface current amplitude $A = \tilde{A} \cdot \phi_z(z = 0)$. Although we force only mode-one waves of tidal frequency at the boundary, higher modes/frequencies can be generated from the nonlinear interaction of lower modes. They can also be generated by imperfect forcing, which is independent of the existence of the current. The details of the stratification profiles are listed in sections 3.3 and 3.4. The geostrophic current is modeled using a Gaussian function (Figure 3.1):

$$V(x, z) = V_{max} \exp\Big(- \frac{(z - z_0)^2}{z_r^2} - \frac{(x - x_0)^2}{x_r^2}\Big). \tag{3.1}$$

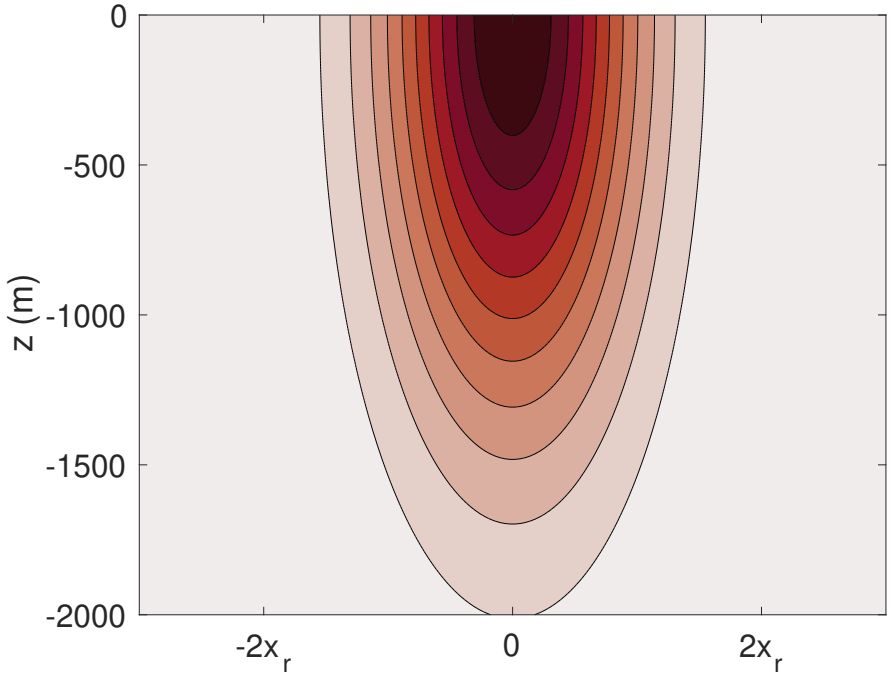

Figure 3.1: Plot of the Gaussian baroclinic current with $z_0 = 0$. $x_0 - 2x_r$ and $x_0 + 2x_r$ are defined as the edges of the current, where the current velocity has dropped to 1% of V_{max}.

The parameters that can be varied under this setting are:

σ : *wave frequency,*

f : *the Coriolis parameter,*

A : *amplitude of the horizontal current of the incident wave,*

(x_0, z_0) : *the location of the centre of the current,*

V_{max} : *the velocity of the geostrophic current at* (x_0, z_0)*,*

(x_r, z_r) : *these determine the width and the height of the current.*

The central domain of interest has length L with uniform resolution $dx = 500$ m. On either side of the central domain there is a layer in which the grid is slowly stretched horizontally with successive grid cell lengths increased by 0.5%. Refer to figure 3.2 for an intuitive plot of the total domain. We set the value of x_0 so that the IWs enter the edge of the current after propagating a distance of s km. s varies for different cases. The edge of the current is defined as $2x_r$ from the center of the current x_0.

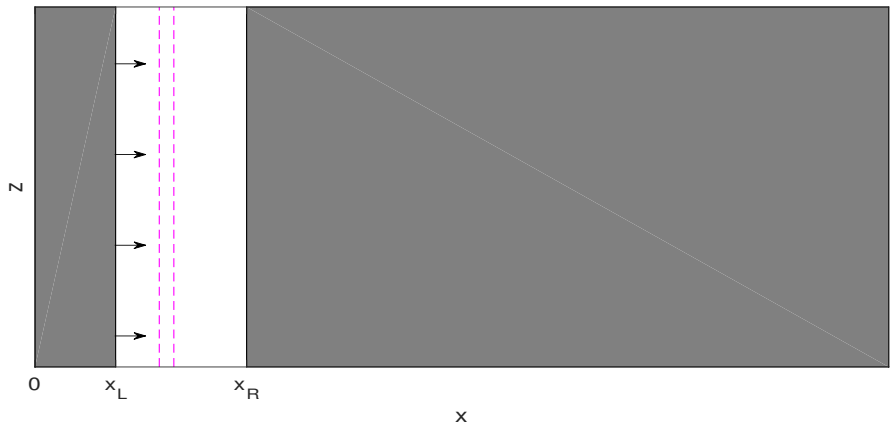

(a)

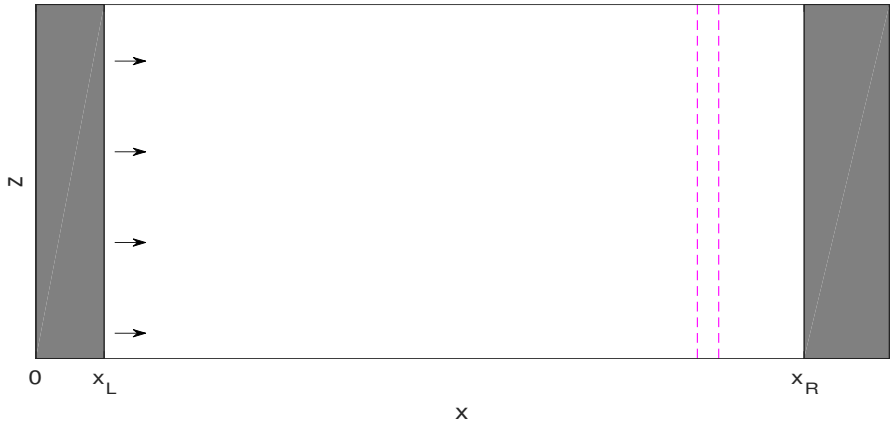

(b)

Figure 3.2: The computational domain with length $L = x_R - x_L$. The shaded gray area is the stretched grid with a ratio of 0.5%. Domain (a) is used if the reflection of the waves from the current is small. The stretched grid is longer to the right of the domain than that to the left. Domain (b) is used if the reflection of the waves from the current is large. Instead of increasing the stretched grid on the left, we have lengthened the domain of interest $x_R - x_L$. This is because the incident wave forcing is implemented on the right edge of the left stretched grid, which makes the left layer less effective in absorbing the leftward propagating reflection waves. The arrows represent the forcing of the linear waves. The magenta dashed lines are the edges of the current.

Linear theory predicts that the majority of the waves can propagate through the current if $\sigma > (f_{eff})_{max}$, and waves will get partially reflected if $\sigma < (f_{eff})_{max}$. We separate our cases into two groups. In the first group, σ is much larger than f so that no stable currents can lift $(f_{eff})_{max}$ up to be larger or even close to σ. Semidiurnal tides are the most commonly observed internal tides and they are studied in the first group. In the second group, we have near inertial waves, i.e. f is close to σ. The currents are chosen so that $(f_{eff})_{max}$ is larger than or close to σ. Most strong currents are in low- to mid-latitudes, where f is much smaller than semidiurnal but can be close to diurnal frequencies. Diurnal tides are studied in the second group. The critical latitudes for semidiurnal and diurnal tides are approximately 75° and 29°. respectively.

Our analysis is mainly focused on 1) the reflection coefficient R of the internal waves from the current and 2) the linear modes produced after the waves propagate through the current. For each f and σ, we have conducted two extra simulations A and B to set the benchmarks. Simulation A has only the mode-1 ITs with no current and simulation B has only the geostrophic current with no IWs. We define E_0 as the energy flux in simulation A, which is the total energy flux not contaminated with possible reflections from the current. For simulations including currents, E_0 is considered to be the incident IW energy flux and we define E_T as the transmitted energy flux at the right side. The reflection coefficient R is defined by $1 - \frac{E_T}{E_0}$. We define E_n as the modal energy flux to the right of the current, where n is the modal number. Note $\sum_{n=1}^{n=\infty} E_n = E_T$. $P_n = \frac{E_n}{E_0}$ is the fraction of the energy in the linear modes generated as the incident mode-1 wave passes through the current.

Ideally there should be no radiating waves in simulation B. However, the current will emit tiny fluxes in the simulation because of small numerical imbalances. Simulation B provides a baseline $E0_n$ for E_n. Simulation A provides a baseline energy flux $P0_n$, the fraction of the incident energy flux in mode n waves, in the absence of a current such that any simulations with $P_n \approx P0_n$ are seen as currents that are too weak to convert a significant fraction of incident energy to higher modes. Figure 3.3 shows a snapshot of the modal coefficients u_n of a semi-diurnal IT for the first four modes at the end of 20 tidal periods in the absence of a current showing more than 99% of the incident energy flux is in mode one waves. The upper panel shows the expected mode-1 wave energy propagating a distance of 1386 km ($c_g = 1.55$ m/s) at $x = 2486$ km with the forcing at $x_L = 1100$ km. The lower panel shows the higher mode waves are over two orders of magnitude smaller than the mode-1 wave. For example, the blue curve shows a much weaker mode-2 wave. The long wavelength part coincident with the main mode-1 wave has a near inertial frequency. We further verify this result by calculating the power spectrum density analysis which shows that waves with frequencies close to f are generated (Figure 3.4). The short wavelength is a mode-2 wave of twice the tidal frequency, which is a result of the crude forcing at the

western boundary. At the end of the 20 tidal periods, this higher frequency mode-2 wave has propagated 691 km ($c_g = 0.77$ m/s) at $x = 1791$ km and it has a wavelength of 26 km. The magenta (green) curve shows a even weaker mode-3 (mode-4) wave. At the tidal frequency, the wavelength and the group velocity of the mode-3 (mode-4) are 47 km (35 km) and 0.52 m/s (0.39 m/s), respectively. The mode-3 wave has propagated 460 km at $x = 1560$ km after 20 tidal periods, while the mode-4 wave signal is very weak.

3.2 Linear theory on reflection coefficient: barotropic current

Before proceeding to the numerical simulations with more realistic baroclinic background currents, we first present a simple linear theory for an idealized barotropic current. Let us consider a fluid with a constant buoyancy frequency N and a continuous piecewise linear geostrophic barotropic current profile,

$$V(x) = 2\sigma_V\big(x + L\big), \quad -L \le x \le 0, \tag{3.2}$$

$$V(x) = -2\sigma_V\big(x - L\big), \quad 0 < x \le L, \tag{3.3}$$

$$V(x) = 0, \quad \text{otherwise.} \tag{3.4}$$

Here $V_{max} = V(0) = 2L\sigma_V$. The wave field is (u, v, w, p, ρ). The background velocity field is $(0, V, 0)$. The effective frequency is,

$$f_1 = \sqrt{f^2 + 2f\sigma_V}, \quad -L < x < 0, \tag{3.5}$$

$$f_2 = \sqrt{f^2 - 2f\sigma_V}, \quad 0 < x < L. \tag{3.6}$$

Note V_x does not exist at $x = -L, 0, L$. $f_{eff} = f$ outside of $[-L, L]$. Here we define an incident internal mode-1 wave with $u(x, z, t) = a\sin(kx - \sigma t + kL)\cos(mz)$ propagating rightward into the current. Since a barotropic current does not vary the background density, the vertical structure of the internal wave is the same throughout the domain. The horizontal wavenumber does change, it is k_1 and k_2 in the left and right half of the current. We will first derive the solutions for three scenarios: 1) blocking in the left half of the current so $\sigma_V > 0$ and $\sigma < f_1$; 2) blocking in the right half of the current so $\sigma_V < 0$

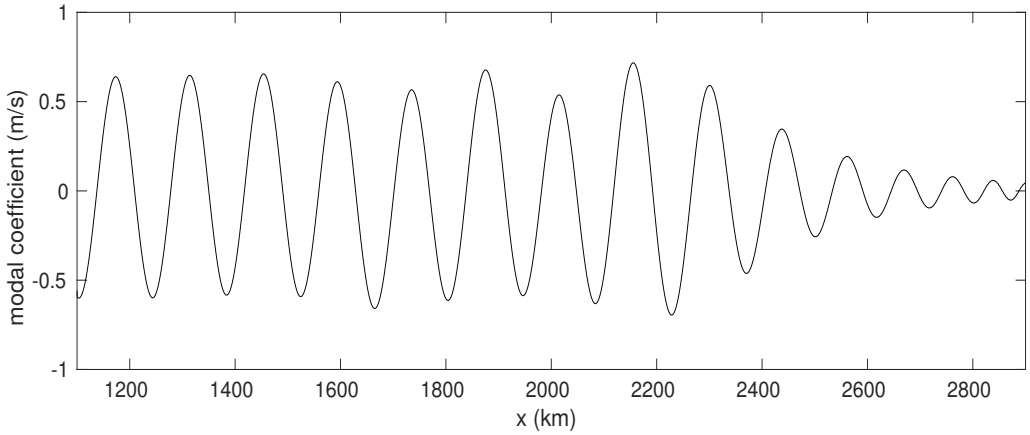

(a)

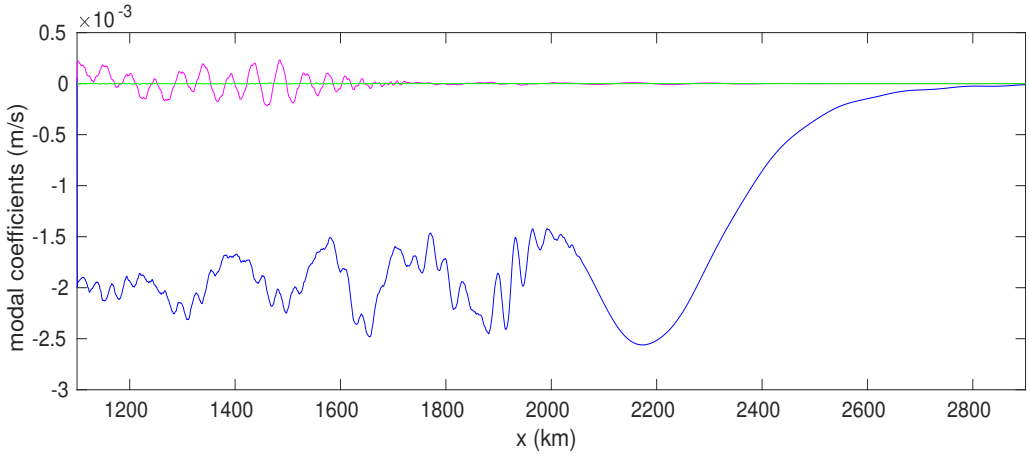

(b)

Figure 3.3: The modal amplitudes of horizontal current for a forced mode-one semi-diurnal IT at the end of the 20 tidal periods in the absence of a current. The forcing starts at $x_L = 1100$ km. $N_L^2 = N_1^2$. $f = 1 \times 10^{-4} s^{-1}$. Upper panel: u_1. Lower panel: u_2 (blue), u_3 (magenta) and u_4 (green). The amplitude of u_2 is less than 1% than that of u_1.

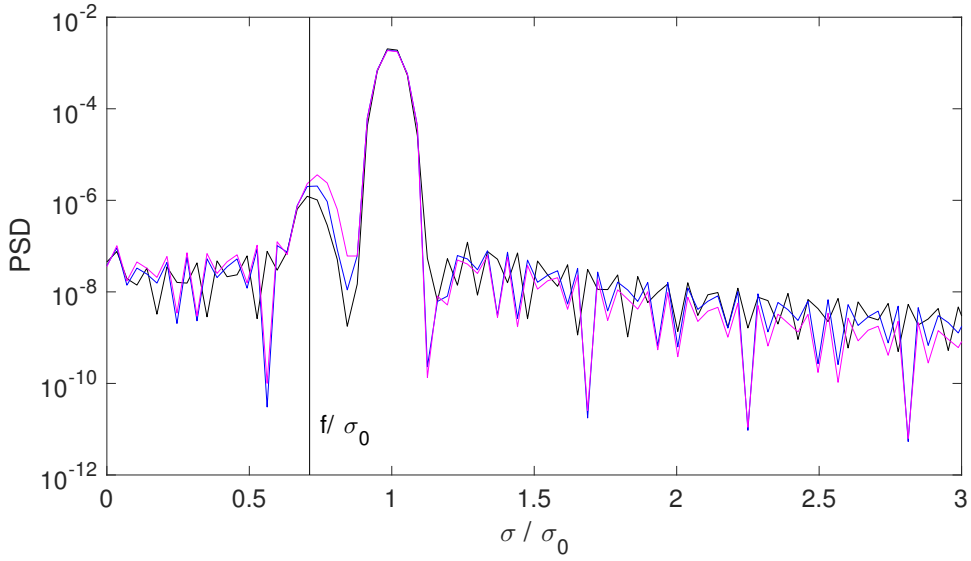

Figure 3.4: Power spectrum density estimated at $x = 1360\,\text{km}$ (black), $x = 1660\,\text{km}$ (blue) and $x = 1960\,\text{km}$ (magenta) from the horizontal velocity. No geostrophic current in this simulation.

and $\sigma < f_2$; and 3) no blocking so $\sigma > \max(f_1, f_2)$. We denote

$$\frac{k}{m} = \sqrt{\frac{\sigma^2 - f^2}{N^2 - \sigma^2}}, \tag{3.7}$$

$$\frac{k_1}{m} = \sqrt{\frac{|\sigma^2 - f_1^2|}{N^2 - \sigma^2}}, \tag{3.8}$$

$$\frac{k_2}{m} = \sqrt{\frac{|\sigma^2 - f_2^2|}{N^2 - \sigma^2}}. \tag{3.9}$$

$$r_1 = \left(\frac{\sigma}{k} - \frac{f^2}{k\sigma}\right) \Big/ \left(\frac{\sigma}{k_1} - \frac{f(f + 2\sigma_V)}{k_1\sigma}\right) = \frac{\sigma^2 - f^2}{\sigma^2 - f_1^2} \cdot \frac{k_1}{k}, \tag{3.10}$$

$$r_2 = \left(\frac{\sigma}{k} - \frac{f^2}{k\sigma}\right) \Big/ \left(\frac{\sigma}{k_2} - \frac{f(f - 2\sigma_V)}{k_2\sigma}\right) = \frac{\sigma^2 - f^2}{\sigma^2 - f_2^2} \cdot \frac{k_2}{k}, \tag{3.11}$$

$$r_{12} = \left(\frac{\sigma}{k_1} - \frac{f_1^2}{k_1\sigma}\right) \Big/ \left(\frac{\sigma}{k_2} - \frac{\sigma_2^2}{k_2\sigma}\right) = \frac{r_2}{r_1}. \tag{3.12}$$

To the left of the current $x \leq -L$, the wave field consists of the incident wave and reflected waves

$$\begin{aligned} u_0 = & \, a \sin(kx - \sigma t + kL) \cos(mz) \\ & + u_{01} \sin(kx + \sigma t + kL) \cos(mz), \\ & + u_{02} \cos(kx + \sigma t + kL) \cos(mz). \end{aligned} \tag{3.13}$$

The equations and the reflection coefficients for the three cases are summarized in the next four sub-sections.

Case 1: $\sigma_V > 0$ **and** $\sigma < f_1$

Because $\sigma < f_{eff} = f_1$ for $-L < x < 0$, the wave field varies exponentially in x in this region. It has the general form

$$\begin{aligned} u_1 = & \sin(\sigma t) \cos(mz) \cdot (u_{11} e^{k_1(x+L)} + u_{12} e^{-k_1(x+L)}) \\ & + \cos(\sigma t) \cos(mz) \cdot (u_{13} e^{k_1(x+L)} + u_{14} e^{-k_1(x+L)}). \end{aligned} \tag{3.14}$$

For $0 < x < L$ the solution has the form of a linear combination of leftward and rightward propagating waves,

$$\begin{aligned} u_2 = & \, u_{21} \sin(k_2 x - \sigma t) \cos(mz) + u_{22} \sin(k_2 x + \sigma t) \cos(mz) \\ & + u_{23} \cos(k_2 x - \sigma t) \cos(mz) + u_{24} \cos(k_2 x + \sigma t) \cos(mz). \end{aligned} \tag{3.15}$$

The wave field for $L < x$, consists of a transmitted wave regardless the sign of σ_V,

$$u_3 = u_{31} \sin(kx - \sigma t - kL) \cos(mz) + u_{32} \cos(kx - \sigma t - kL) \cos(mz). \tag{3.16}$$

Applying continuity of horizontal velocity at $x = -L$, 0, L, the matching conditions for u are

$$-a + u_{01} = u_{11} + u_{12}, \tag{3.17}$$

$$u_{02} = u_{13} + u_{14}, \tag{3.18}$$

$$u_{11} e^{k_1 L} + u_{12} e^{-k_1 L} = -u_{21} + u_{22}, \tag{3.19}$$

$$u_{13} e^{k_1 L} + u_{14} e^{-k_1 L} = u_{23} + u_{24}, \tag{3.20}$$

$$(u_{21} + u_{22}) \sin(k_2 L) + (u_{23} + u_{24}) \cos(k_2 L) = u_{32}, \tag{3.21}$$

$$(-u_{21} + u_{22}) \cos(k_2 L) + (u_{23} - u_{24}) \sin(k_2 L) = -u_{31}. \tag{3.22}$$

The pressure is also continuous at $x = -L$, 0, and L. For $x \leq -L$ it is the same for all the cases,

$$p_0 = \cos(mz)(\frac{\sigma}{k} - \frac{f^2}{k\sigma}) \cdot \Big(\sin(kx - \sigma t + kL)a \\ - \sin(kx + \sigma t + kL)u_{01} + \cos(kx + \sigma t + kL) \cdot (-u_{02}) \Big). \tag{3.23}$$

The pressure for $-L < x \leq 0$ is

$$p_1 = \cos(mz)(\frac{\sigma}{k_1} - \frac{f(f + 2\sigma_V)}{k_1\sigma}) \cdot \Big(\cos(\sigma t) \cdot (-u_{11}e^{k_1(x+L)} + u_{12}e^{-k_1(x+L)}) \\ + \sin(\sigma t) \cdot (u_{13}e^{k_1(x+L)} - u_{14}e^{-k_1(x+L)}) \Big). \tag{3.24}$$

The pressure for $0 < x \leq L$ is

$$p_2 = \cos(mz)(\frac{\sigma}{k_2} - \frac{f(f - 2\sigma_V)}{k_2\sigma}) \cdot \Big(\sin(k_2x - \sigma t)u_{21} - \sin(k_2x + \sigma t)u_{22} \\ + \cos(k_2x - \sigma t) \cdot u_{23} - \cos(k_2x + \sigma t) \cdot u_{24} \Big). \tag{3.25}$$

The pressure at $L < x$ is the same for all the cases

$$p_3 = \cos(mz)(\frac{\sigma}{k} - \frac{f^2}{k\sigma}) \cdot \Big(\sin(kx - \sigma t + kL)u_{31} + \cos(kx - \sigma t + kL) \cdot u_{32} \Big). \tag{3.26}$$

Applying continuity of pressure at the interfaces, we have the equations for the coefficients are

$$(-a - u_{01}) \cdot r_1 = u_{13} - u_{14}, \tag{3.27}$$

$$-u_{02} \cdot r_1 = -u_{11} + u_{12}, \tag{3.28}$$

$$(-u_{11}e^{k_1L} + u_{12}e^{-k_1L}) \cdot r_{12} = u_{23} - u_{24}, \tag{3.29}$$

$$(u_{13}e^{k_1L} - u_{14}e^{-k_1L}) \cdot r_{12} = -u_{21} - u_{22}, \tag{3.30}$$

$$(-u_{21} - u_{22})\cos(k_2L) + (u_{23} + u_{24})\sin(k_2L) = -u_{31} \cdot r_2, \tag{3.31}$$

$$(u_{21} - u_{22})\sin(k_2L) + (u_{23} - u_{24})\cos(k_2L) = u_{32} \cdot r_2. \tag{3.32}$$

Case 2: $\sigma_V < 0$ **and** $\sigma < f_2$

The wave field for $-L < x \leq 0$ is

$$\begin{aligned} u_1 = {} & u_{11}\sin(k_1x - \sigma t + k_1L)\cos(mz) \\ & + u_{12}\sin(k_1x + \sigma t + k_1L)\cos(mz) \\ & + u_{13}\cos(k_1x - \sigma t + k_1L)\cos(mz) \\ & + u_{14}\cos(k_1x + \sigma t + k_1L)\cos(mz), \end{aligned} \tag{3.33}$$

which is a combination of leftward and rightward propagating waves. The wave field for $0 \leq x \leq L$ varies exponentially in x,

$$\begin{aligned} u_2 = {} & \sin(\sigma t)\cos(mz)\cdot(u_{11}e^{k_2x} + u_{12}e^{-k_2x}) \\ & + \cos(\sigma t)\cos(mz)\cdot(u_{13}e^{k_2x} + u_{14}e^{-k_2x}). \end{aligned} \tag{3.34}$$

The wave field for $L < x$ is the same as that in the other cases,

$$u_3 = u_{31}\sin(kx - \sigma t - kL)\cos(mz) + u_{32}\cos(kx - \sigma t - kL)\cos(mz). \tag{3.35}$$

Applying continuity of horizontal velocity at $x = -L$, 0, L, the matching conditions for u are

$$-a + u_{01} = -u_{11} + u_{12}, \tag{3.36}$$

$$u_{02} = u_{13} + u_{14}, \tag{3.37}$$

$$(-u_{11} + u_{12})\cos(k_1L) + (u_{13} - u_{14})\sin(k_1L) = u_{21} + u_{22}, \tag{3.38}$$

$$(u_{11} + u_{12})\sin(k_1L) + (u_{13} + u_{14})\cos(k_1L) = u_{23} + u_{24}, \tag{3.39}$$

$$u_{21}e^{k_2L} + u_{22}e^{-k_2L} = -u_{31}, \tag{3.40}$$

$$u_{23}e^{k_2L} + u_{24}e^{-k_2L} = u_{32}. \tag{3.41}$$

The pressure is also continuous at $x = -L$, 0, and L. For $x \leq -L$ it is the same for all the cases,

$$\begin{aligned} p_0 = \cos(mz)(\frac{\sigma}{k} - \frac{f^2}{k\sigma})\cdot\Big(& \sin(kx - \sigma t + kL)a \\ & - \sin(kx + \sigma t + kL)u_{01} + \cos(kx + \sigma t + kL)\cdot(-u_{02})\Big). \end{aligned} \tag{3.42}$$

The pressure for $-L < x \leq 0$ is

$$p_1 = \cos(mz)(\frac{\sigma}{k_1} - \frac{f(f+2\sigma_V)}{k_1\sigma}) \cdot \Big(\sin(k_1x - \sigma t + k_1L)u_{11} - \sin(k_1x + \sigma t + k_1L)u_{12} + \cos(k_1x - \sigma t + k_1L) \cdot u_{13} - \cos(k_1x + \sigma t + k_1L) \cdot u_{14} \Big). \tag{3.43}$$

The pressure for $0 < x \leq L$ is

$$p_2 = \cos(mz)(\frac{\sigma}{k_2} - \frac{f(f-2\sigma_V)}{k_2\sigma}) \cdot \Big(\cos(\sigma t) \cdot (-u_{21}e^{k_2x} + u_{22}e^{-k_2x}) + \sin(\sigma t) \cdot (u_{23}e^{k_2x} - u_{24}e^{-k_2x}) \Big). \tag{3.44}$$

The pressure at $L < x$ is the same for all the cases

$$p_3 = \cos(mz)(\frac{\sigma}{k} - \frac{f^2}{k\sigma}) \cdot \Big(\sin(kx - \sigma t + kL)u_{31} + \cos(kx - \sigma t + kL) \cdot u_{32} \Big). \tag{3.45}$$

Applying continuity of pressure at the interfaces, we have the equations for the coefficients are

$$(-a - u_{01}) \cdot r_1 = -u_{11} - u_{12}, \tag{3.46}$$

$$-u_{02} \cdot r_1 = u_{13} - u_{14}, \tag{3.47}$$

$$\big(\cos(k_1L)(-u_{11} - u_{12}) + \sin(k_1L)(u_{13} + u_{14}) \big) \cdot r_{12} = u_{23} - u_{24}, \tag{3.48}$$

$$\big(\sin(k_1L)(u_{11} - u_{12}) + \cos(k_1L)(u_{13} - u_{14}) \big) \cdot r_{12} = -u_{21} + u_{22}, \tag{3.49}$$

$$-u_{21}e^{k_2L} + u_{22}e^{-k_2L} = u_{32} \cdot r_2, \tag{3.50}$$

$$u_{23}e^{k_2L} - u_{24}e^{-k_2L} = -u_{31} \cdot r_2. \tag{3.51}$$

Case 3: $\sigma > \max(f_1, f_2)$

The wave field for $-L < x \leq 0$ is the same as that in Case 2,

$$\begin{aligned} u_1 = {} & u_{11} \sin(k_1x - \sigma t + k_1L) \cos(mz) \\ & + u_{12} \sin(k_1x + \sigma t + k_1L) \cos(mz) \\ & + u_{13} \cos(k_1x - \sigma t + k_1L) \cos(mz) \\ & + u_{14} \cos(k_1x + \sigma t + k_1L) \cos(mz). \end{aligned} \tag{3.52}$$

The wave field for $0 \le x \le L$ is the same as that in Case 1,

$$u_2 = u_{21}\sin(k_2x - \sigma t)\cos(mz) + u_{22}\sin(k_2x + \sigma t)\cos(mz) \\ + u_{23}\cos(k_2x - \sigma t)\cos(mz) + u_{24}\cos(k_2x + \sigma t)\cos(mz). \tag{3.53}$$

The wave field for $L < x$ is the same as that in the other cases,

$$u_3 = u_{31}\sin(kx - \sigma t - kL)\cos(mz) + u_{32}\cos(kx - \sigma t - kL)\cos(mz). \tag{3.54}$$

Applying continuity of horizontal velocity at $x = -L$, 0, L, the matching conditions for u are

$$-a + u_{01} = -u_{11} + u_{12}, \tag{3.55}$$

$$u_{02} = u_{13} + u_{14}, \tag{3.56}$$

$$(-u_{11} + u_{12})\cos(k_1L) + (u_{13} - u_{14})\sin(k_1L) = -u_{21} + u_{22}, \tag{3.57}$$

$$(u_{11} + u_{12})\sin(k_1L) + (u_{13} + u_{14})\cos(k_1L) = u_{23} + u_{24}, \tag{3.58}$$

$$(u_{21} + u_{22})\sin(k_2L) + (u_{23} + u_{24})\cos(k_2L) = u_{32}, \tag{3.59}$$

$$(-u_{21} + u_{22})\cos(k_2L) + (u_{23} - u_{24})\sin(k_2L) = -u_{31}. \tag{3.60}$$

The pressure is also continuous at $x = -L$, 0, and L. For $x \le -L$ it is the same for all the cases,

$$p_0 = \cos(mz)(\frac{\sigma}{k} - \frac{f^2}{k\sigma}) \cdot \Big(\sin(kx - \sigma t + kL)a \\ - \sin(kx + \sigma t + kL)u_{01} + \cos(kx + \sigma t + kL) \cdot (-u_{02}) \Big). \tag{3.61}$$

The pressure for $-L < x \le 0$ is the same as that in Case 2,

$$p_1 = \cos(mz)(\frac{\sigma}{k_1} - \frac{f(f + 2\sigma_V)}{k_1\sigma}) \cdot \Big(\sin(k_1x - \sigma t + k_1L)u_{11} - \sin(k_1x + \sigma t + k_1L)u_{12} \\ + \cos(k_1x - \sigma t + k_1L) \cdot u_{13} - \cos(k_1x + \sigma t + k_1L) \cdot u_{14} \Big). \tag{3.62}$$

The pressure for $0 < x \le L$ is the same as that in Case 1,

$$p_2 = \cos(mz)(\frac{\sigma}{k_2} - \frac{f(f - 2\sigma_V)}{k_2\sigma}) \cdot \Big(\sin(k_2x - \sigma t)u_{11} - \sin(k_2x + \sigma t)u_{12} \\ + \cos(k_2x - \sigma t) \cdot u_{13} - \cos(k_2x + \sigma t) \cdot u_{14} \Big). \tag{3.63}$$

The pressure at $L < x$ is the same for all the cases

$$p_3 = \cos(mz)(\frac{\sigma}{k} - \frac{f^2}{k\sigma}) \cdot \bigg(\sin(kx - \sigma t + kL)u_{31} + \cos(kx - \sigma t + kL) \cdot u_{32} \bigg). \tag{3.64}$$

Applying continuity of pressure at the interfaces, we have the equations for the coefficients are

$$(-a - u_{01}) \cdot r_1 = -u_{11} - u_{12}, \tag{3.65}$$

$$-u_{02} \cdot r_1 = u_{13} - u_{14}, \tag{3.66}$$

$$\big(\cos(k_1 L)(-u_{11} - u_{12}) + \sin(k_1 L)(u_{13} + u_{14}) \big) \cdot r_{12} = -u_{21} - u_{22}, \tag{3.67}$$

$$\big(\sin(k_1 L)(u_{11} - u_{12}) + \cos(k_1 L)(u_{13} - u_{14}) \big) \cdot r_{12} = u_{23} - u_{24}, \tag{3.68}$$

$$(-u_{21} - u_{22}) \cos(k_2 L) + (u_{23} + u_{24}) \sin(k_2 L) = -u_{31} \cdot r_2, \tag{3.69}$$

$$(u_{21} - u_{22}) \sin(k_2 L) + (u_{23} - u_{24}) \cos(k_2 L) = u_{32} \cdot r_2. \tag{3.70}$$

Reflection coefficients for Cases 1,2,3

Solutions can be obtained by solving the twelve equations. The detailed solutions are obtained using Maple and they are too tedious thus omitted here. Energy flux conservation, i.e. the incident energy flux equals the sum of the reflected and the transmitted energy flux,

$$a^2 = u_{01}^2 + u_{02}^2 + u_{31}^2 + u_{32}^2 \tag{3.71}$$

has been verified. The reflection coefficient is

$$R = \frac{u_{01}^2 + u_{02}^2}{a^2} = 1 - \frac{16 r_1^2 r_2^2}{T}, \tag{3.72}$$

where, for Case 1: $\sigma_V > 0$ and $\sigma < f_1$,

$$\begin{aligned} T = {} & [(r_2^2 - 1)(r_1^2 - r_2^2)\cos^2(k_2 L) + r_1^2 + r_2^4](r_1^2 + 1)(e^{-2k_1 L} + e^{2k_1 L}) \\ & + \sin(2k_2 L)(r_2^2 - 1) r_1 r_2 (r_1^2 + 1)(e^{-2k_1 L} - e^{2k_1 L}) \\ & - 2[(r_2^2 - 1)(r_1^2 - 1)(r_1^2 + r_2^2)\cos^2(k_2 L) + r_1^4 + r_2^4 - (r_2^4 + 4r_2^2 + 1) r_1^2], \end{aligned} \tag{3.73}$$

for Case 2: $\sigma_V < 0$ and $\sigma < f_2$,

$$\begin{aligned} T = {} & [(r_1^2 - 1)(r_1^2 - r_2^2)\cos^2(k_1 L) + r_1^4 + r_2^2](r_2^2 + 1)(e^{-2k_2 L} + e^{2k_2 L}) \\ & + \sin(2k_1 L)(r_1^2 - 1) r_1 r_2 (r_2^2 + 1)(e^{-2k_2 L} - e^{2k_2 L}) \\ & - 2[(r_1^2 - 1)(r_2^2 - 1)(r_1^2 + r_2^2)\cos^2(k_1 L) + r_1^4 + r_2^4 - (r_1^4 + 4r_1^2 + 1) r_2^2], \end{aligned} \tag{3.74}$$

for Case 3: $\sigma > \max\left(f_1, f_2\right)$

$$\begin{aligned} T = 4(r_1^2-1)[((1-r_2^2)r_1^2 - r_2^4 + r_2^2)\cos^2(k_2L) + r_2^4 - r_1^2]\cos^2(k_1L) \\ + 2\sin(2k_1L)\sin(2k_2L)\cdot r_1r_2(r_1^2-1)(r_2^2-1) \\ + 4((r_2^2-1)r_1^4 - r_2^4 + r_2^2)\cos^2(k_2L) + 4(r_1^2+r_2^2)^2. \end{aligned} \tag{3.75}$$

Note the solutions in (3.73) and (3.74) are symmetric: replacing (r_1, r_2, k_1, k_2) with (r_2, r_1, k_2, k_1) in (3.73) recovers (3.74). Since our current structure is symmetric about the center $x = 0$, the reflection R does not depend on the sign of the current V_{max}. If we choose the incoming mode-1 waves with diurnal frequency $\sigma = \frac{2\pi}{24.84\cdot 3600}s^{-1} \approx 7.026\times 10^{-5}s^{-1}$, $N_L^2 = 1\times 10^{-6}s^{-1}$ and vary L, V_{max} and f, R can be computed using (3.73) and (3.74) (see Figure 3.5). In general, R increases as f_{eff} increases, which can be achieved by increasing V_{max} and f or decreasing L. The value of R saturates as f_{eff} approaches the wave frequency σ. We can see the symmetry of R regarding the signs of V_{max} in Figure 3.5 (b, c). In Figure 3.5 (a, b), $R \to 0$ as $L \to 0$ because the interaction area with large f_{eff} goes to zero. On the other hand, as L increases, f_{eff} decreases, but R does not decrease monotonically with f_{eff}. This fine detail will be explored further in the following sub-section.

General barotropic current

Now we consider a more general picture where the current can be of any barotropic structure $V(x)$.

$$u_t - fv = -p_x, \tag{3.76}$$

$$v_t + uV_x + fu = 0, \tag{3.77}$$

$$w_t = -p_z - \rho g, \tag{3.78}$$

$$u_x + w_z = 0, \tag{3.79}$$

$$\rho_t - w\frac{N^2}{g} = 0. \tag{3.80}$$

Taking the current to be a function of x only we look for solutions of the form $u = A(x)e^{-i\sigma t}\cos(mz)$ giving

$$A_{xx} + \frac{\sigma^2 - fV_x - f^2}{N^2 - \sigma^2}m^2A = 0. \tag{3.81}$$

If the hydrostatic condition is applied, equation 3.81 becomes

$$A_{xx} + \frac{\sigma^2 - fV_x - f^2}{N^2}m^2A = 0. \tag{3.82}$$

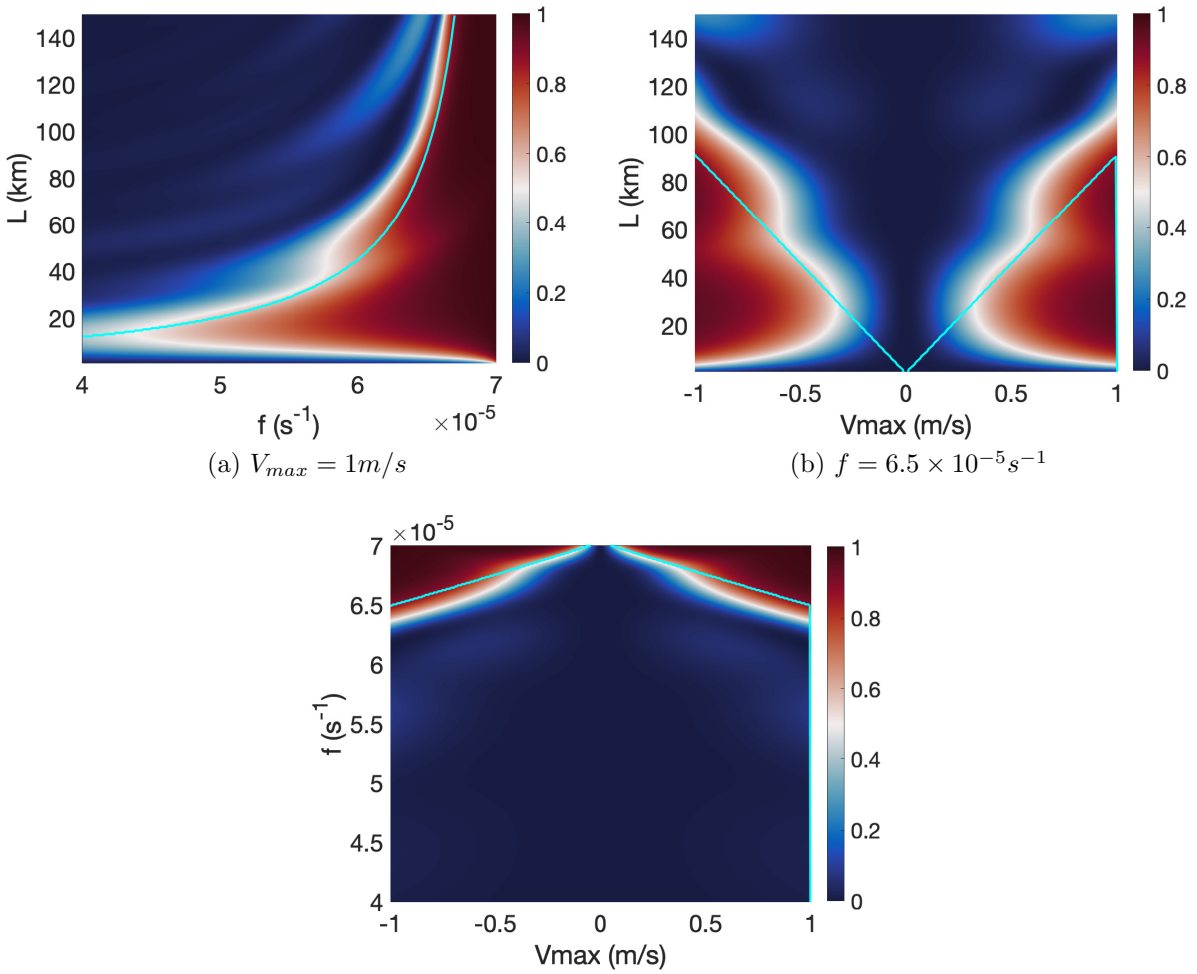

(a) $V_{max} = 1m/s$

(b) $f = 6.5 \times 10^{-5} s^{-1}$

(c) $L = 90km$

Figure 3.5: Reflection coefficient for the piecewise linear barotropic current by fixing V_{max}, f and L, respectively. $N^2 = 1 \times 10^{-6} s^{-1}$. $\sigma \approx 7.026 \times 10^{-5} s^{-1}$. The cyan line marks $f_{eff} = \sigma$. In a and b, we have $f_{eff} > \sigma$ below the cyan curve. In c, $f_{eff} > \sigma$ above the cyan curve.

Two current profiles are considered, the linear current in 3.2 to 3.4 and a Gaussian current

$$V(x) = V_{max} e^{-\frac{(x-x_0)^2}{x_r^2}}. \tag{3.83}$$

Three parameters are varied here, L (linear current) or x_r (Gaussian current), f and V_{max}. Assume the wave propagates from left to right, we solve 3.81 by initializing the transmitted wave and integrate it backwards to find the solution at the left of the current. This is done numerically using MATLAB function 'ode113'. We then separate the incoming and reflected waves and find the reflection coefficient R (see Figures 3.6 and 3.7). The main features are summarized below.

- If L or x_r is very small, e.g. $L < 10$ km in figure 3.6, R is small because the interaction area with large f_{eff} is too small. Here the incident IT wavelength is (189, 150, 129) km for $f = (6.7, 6.5, 6.3) \times 10^{-5} s^{-1}$. However, in practice it is unlikely we can have a stable current with such a small L since the Rossby number $Ro = O(\frac{V_x}{f})$ is too large [Phillips, 1963].

- If L or x_r is slightly larger but not too large, e.g. 40 km $< L <$ 90 km with $f = 6.5 \times 10^{-5} s^{-1}$ and $V_{max} = 1$ m/s in figure 3.6, we are in the region of $\sigma < (f_{eff})_{max}$ and the currents may be stable ($Ro \ll 1$). This is the region of strong reflection and also the focus of this section. With all the other parameters fixed, larger f or larger V_{max} produces larger values of f_{eff}, resulting in stronger reflections. We define L_w as the length of the blocking region where $\sigma < f_{eff}$. Large values of L_w signal strong interactions between the wave and the current. If we look at currents with linear structures (figure 3.6), R does not decrease monotonically as L increases. This is because larger L means smaller f_{eff} but larger L_w. The wave reflection depends on the competing effects of L and f_{eff}. For Gaussian currents, if we fix V_{max}, larger x_r usually indicates a smaller interaction region L_w ($\sigma < f_{eff}$) and also smaller f_{eff}, so increasing x_r or L decreases R monotonically (figure 3.7).

- As we increase L or x_r even further, we are in the region where σ remains above f_{eff}. The value of R drops to a lower level and it behaves quite differently for currents of different structures. R fluctuates up and down with the linear currents, while it monotonically approaches 0 with the Gaussian currents. This difference is a result of the competing effects of the value of f_{eff} and how fast f_{eff} increases/decreases. Figure 3.8 plots the reflection R versus $2L/\lambda$, the total width of the current divided by the incident IT wavelength, for the linear idealized current with $f \in [6.1, 6.5] \times 10^{-5} s^{-1}$. We focus in the region where $f_{eff} < \sigma$ and $R < 40\%$. In the upper panel

where $V_{max} = 1$ m/s, the local maximum of R coincides with the multiples of $2L/\lambda$. This interesting fact occurs for a large range of $f \in [5.0 \times 10^{-5}, 6.6 \times 10^{-5}]s^{-1}$, which if scaled by the wave frequency σ is $f/\sigma \in [0.71, 0.94]$. In the lower panel where f is fixed, we can see the behaviour of R is consistent for different V_{max} in that the local max always occurs at multiples of $2L/\lambda$. Figure 3.9 plots an example when $f \geq 6.7 \times 10^{-5}s^{-1}$ and the local max of R does not coincide with the multiples of $2L/\lambda$. The exception is in the lower panel where $V_{max} = 0.4$ m/s (green line), the matching pattern occurs again because decreasing V_{max} means to reduce the effective frequency in the current, which achieves a similar effect as to reduce f alone.

- The difference in R obtained by solving 3.81 and 3.82 is negligible for the cases considered here.

Now we perform fully nonlinear simulations with the Gaussian current profile and $f = 6.5 \times 10^{-5}s^{-1}$. The wavelength, phase speed and group velocity of the IWs are 150 km, 1.68 m/s and 0.24 m/s, respectively. We set the edge of the current 500 km away from the left boundary, from which it will take the IW energy about 25 tidal periods to reach the current. With this set up, we are left with two parameters to vary: V_{max} and x_r. Table 3.1 lists all the simulation results and the corresponding theoretical predictions. They are in good agreement. As we vary V_{max} and x_r, both the area L_w where $\sigma < f_{eff}$ and f_{eff} vary. The reflection depends on the combined effects of these two factors.

3.3 Weak reflections with baroclinic currents- $\sigma \gg (f_{eff})_{max}$

We begin with cases without a blocking region. In these cases the reflection from the current is relatively weak. We choose the incoming IWs to have semi-diurnal frequency $\sigma = \frac{2\pi}{12.42 \cdot 3600}s^{-1} \approx 1.41 \times 10^{-4}s^{-1}$. Two values of f are used, $6 \times 10^{-5}s^{-1}$ (lower latitude approximately 25°) and $1 \times 10^{-4}s^{-1}$ (mid-latitude approximately 43°). The IWs propagate $s = 800\ km$ before reaching the current, which is approximately 7 wavelengths. All simulations have been run for 80 tidal periods. Three stratification profiles are used for the stratification N_L^2 to the left of the current (Figure 3.10):

$$N_1^2 = 1.2 \times 10^{-5}\ \text{s}^{-1}, \tag{3.84}$$

$$N_2^2 = 2.8\,\text{sech}^2\left(\frac{z}{200}\right) \times 10^{-4}\ \text{s}^{-1}, \tag{3.85}$$

$$N_3^2 = 2.8\,\text{sech}^2\left(\frac{z}{350}\right) \times 10^{-4}\ \text{s}^{-1}. \tag{3.86}$$

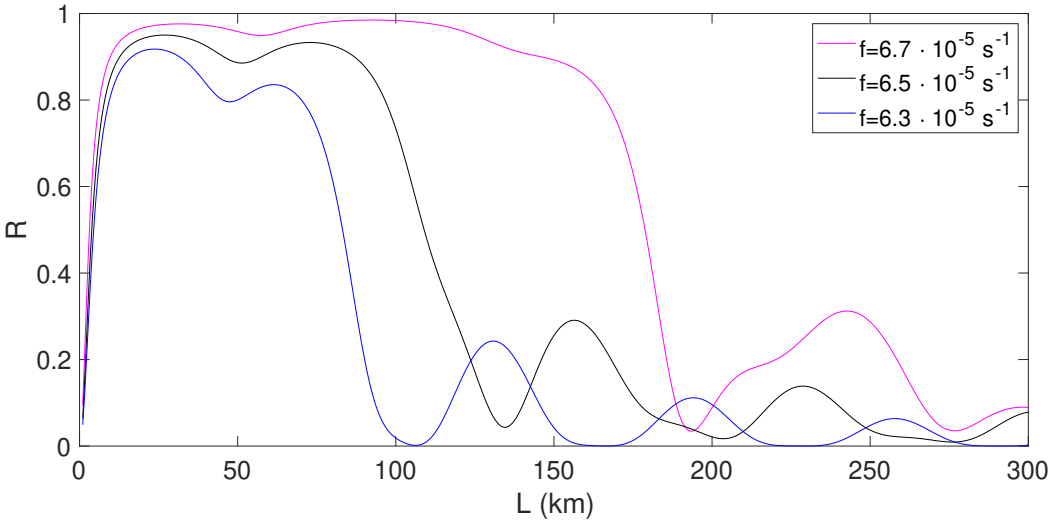

(a) $V_{max} = 1m/s$

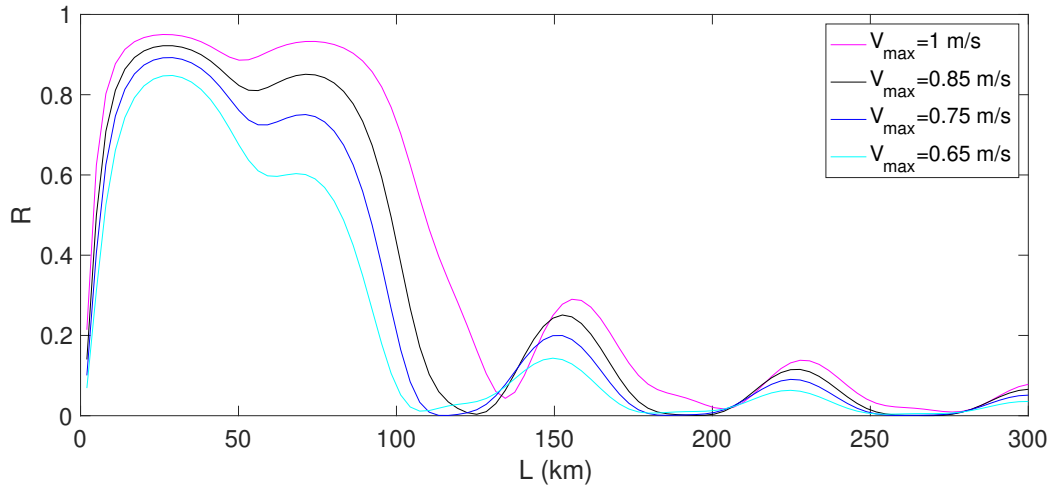

(b) $f = 6.5 \times 10^{-5} s^{-1}$

Figure 3.6: Theoretical predictions of the reflection coefficient R using 3.81 for diurnal internal waves. $H = 2$ km, $N^2 = 1 \times 10^{-6} s^{-1}$. Linear geostrophic current (see 3.2 to 3.4).

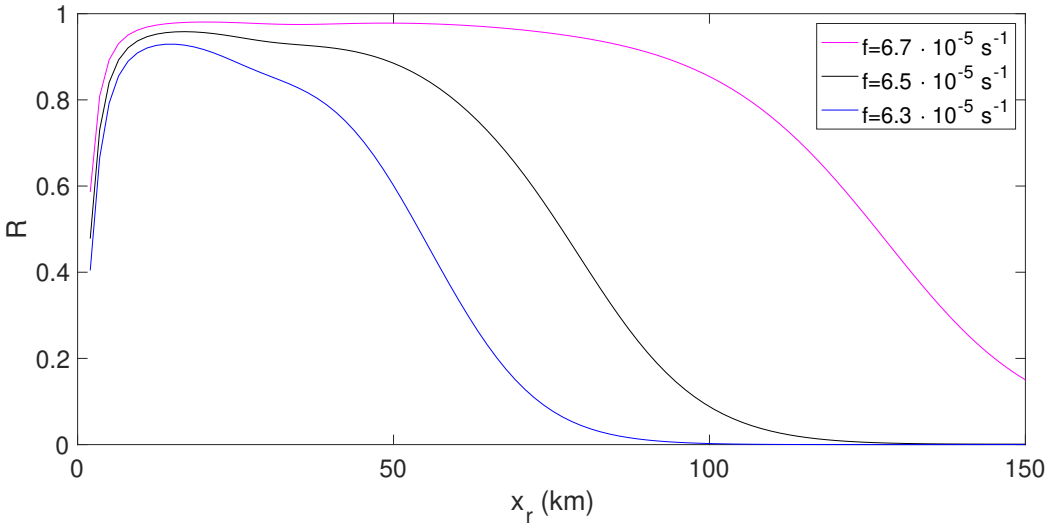

(a) $V_{max} = 1m/s$

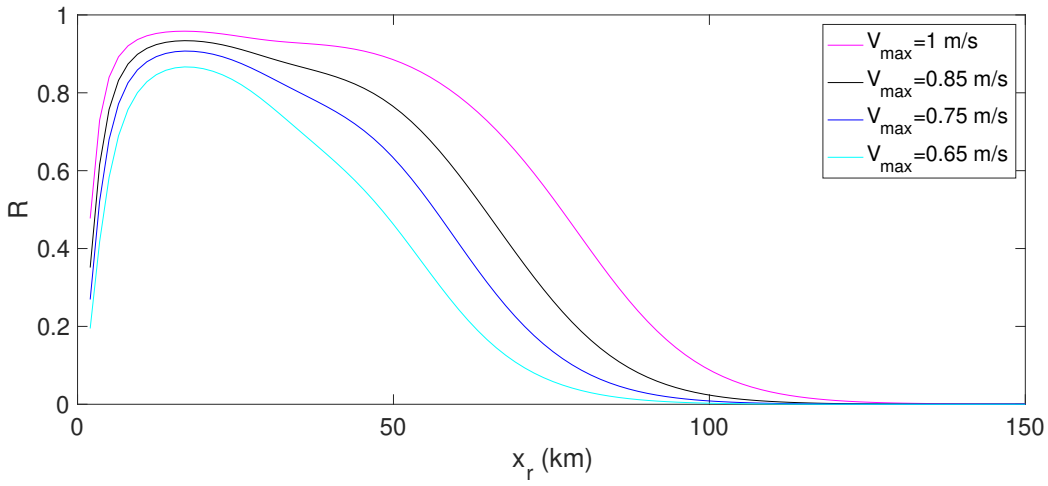

(b) $f = 6.5 \times 10^{-5} s^{-1}$

Figure 3.7: Theoretical predictions of the reflection coefficient R using 3.81 for diurnal internal waves. $H = 2$ km, $N^2 = 1 \times 10^{-6} s^{-2}$. The geostrophic current is of Gaussian structure (see 3.83) with a half width $L = 2x_r$.

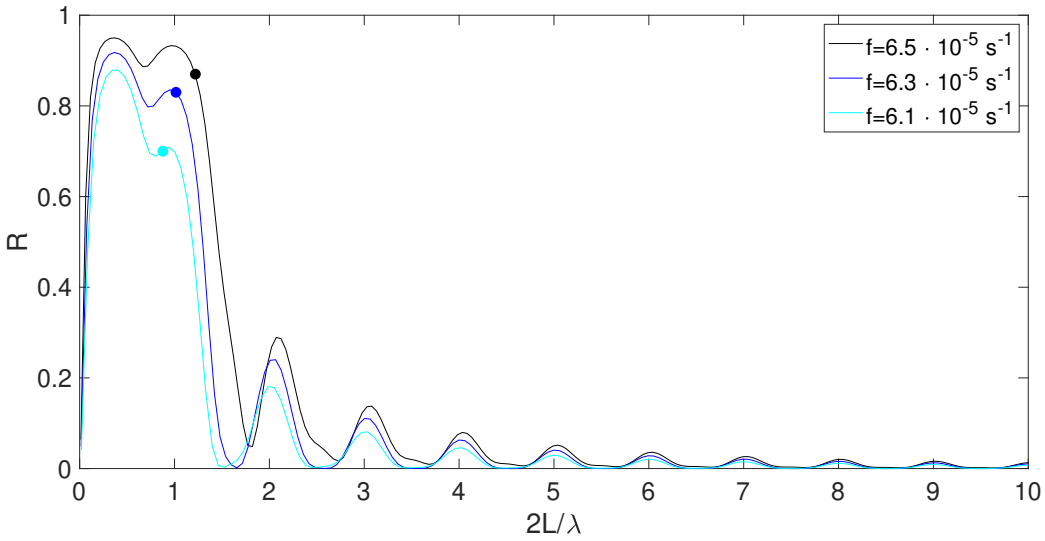

(a) $V_{max} = 1m/s$

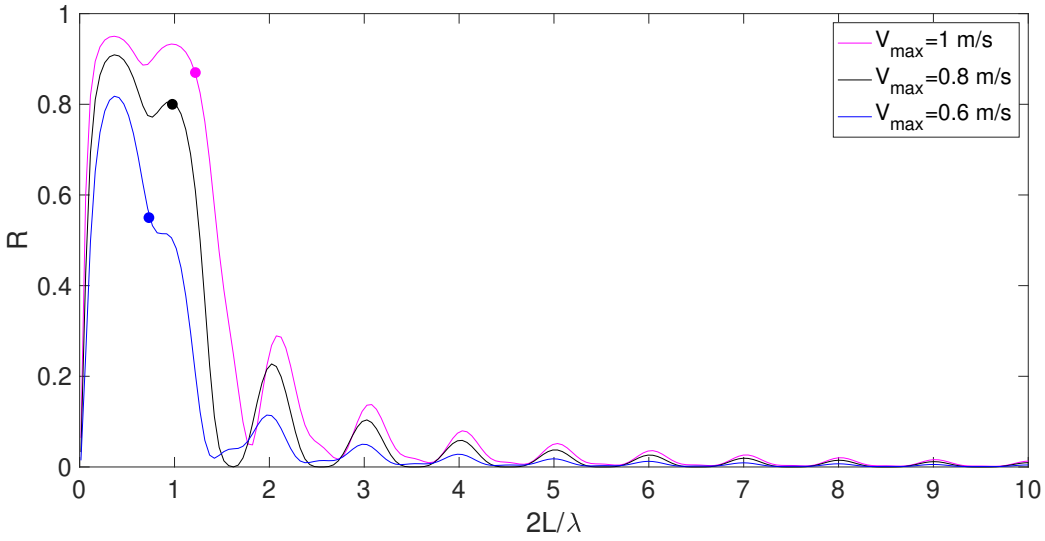

(b) $f = 6.5 \times 10^{-5} s^{-1}$

Figure 3.8: Theoretical predictions of the reflection coefficient R using 3.81 for diurnal internal waves. The x-axis is the total width of the current over the incident IW wavelength $2L/\lambda$. $H = 2$ km, $N^2 = 1 \times 10^{-6} s^{-1}$. $\sigma > f_{eff}$ to the right of the solid circles. Linear geostrophic current (see 3.2 to 3.4).

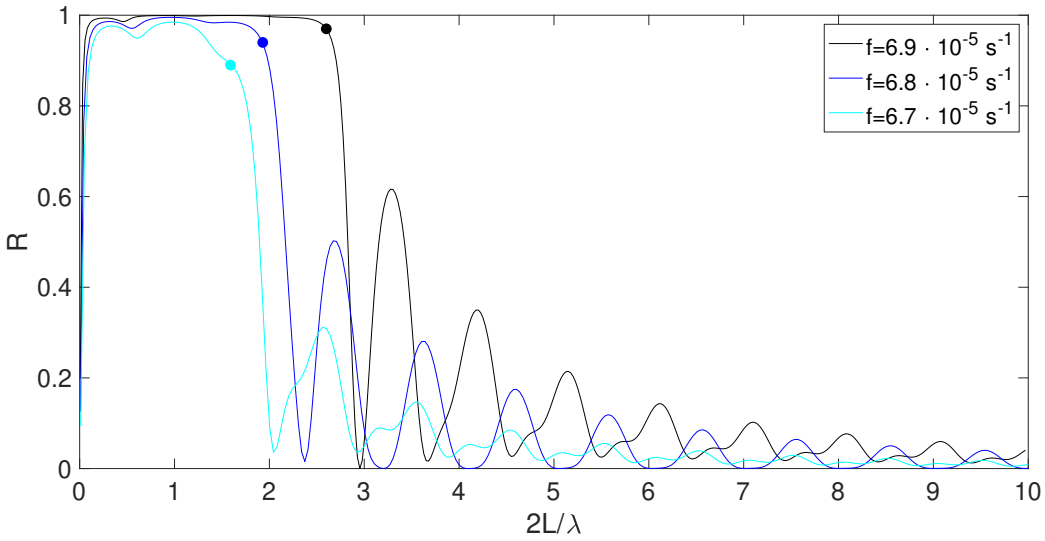

(a) $V_{max} = 1m/s$

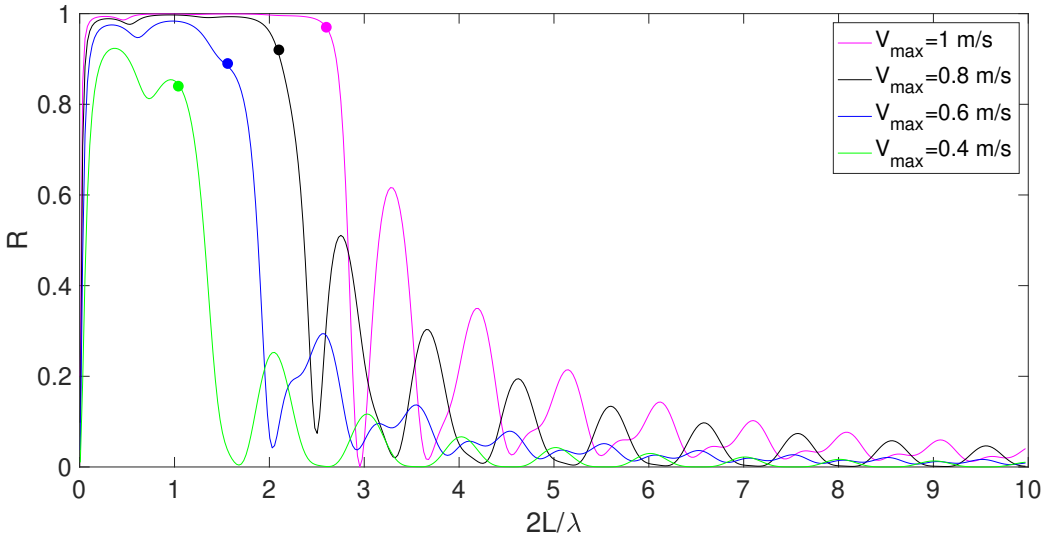

(b) $f = 6.9 \times 10^{-5} s^{-1}$

Figure 3.9: Theoretical predictions of the reflection coefficient R using 3.81 for diurnal internal waves. The x-axis is the total width of the current over the incident IW wavelength $2L/\lambda$. $H = 2$ km, $N^2 = 1 \times 10^{-6} s^{-1}$. $\sigma > f_{eff}$ to the right of the solid circles. Linear geostrophic current (see 3.2 to 3.4).

Table 3.1: Here R and $(R)_{LT}$ denote the reflection coefficients for the Gaussian current from fully nonlinear numerical simulations and linear theory predictions, respectively. $(f_{eff})_{max}$ is the maximum effective frequency in the current.

V_{max} (m/s)	x_r (km)	length L_w of $\sigma < f_{eff}$ (km)	$(f_{eff})_{max}$ (s^{-1})	R	$(R)_{LT}$
1	40	45	7.5×10^{-5}	93 %	92 %
1	50	46	7.31×10^{-5}	90 %	88 %
1	55	47	7.24×10^{-5}	86 %	85 %
1	60	42	7.18×10^{-5}	82 %	80 %
1	70	30	7.09×10^{-5}	66 %	64 %
0.85	40	38	7.36×10^{-5}	86 %	85 %
0.75	40	34	7.26×10^{-5}	78 %	76 %
0.7	40	30	7.21×10^{-5}	72 %	70 %
0.65	40	27	7.16×10^{-5}	66 %	63 %
0.6	40	22	7.11×10^{-5}	58 %	56 %

Since the background current alters the density field, N_L^2 is chosen among N_i^2, $i = 1, 2, 3$, so that the flow is stable throughout the domain, i.e., $N^2 > 0$ everywhere. An explanation for the flow stability by using N_1^2 can be found in appendix A. Note N_2^2 and N_3^2 have their maximum values at the surface, which ignores the presence of a surface mixed layer. We define the total buoyancy field $N^2(x, z) = N_L^2(z) + N_g^2(x, z)$. N_g^2 is in geostrophic balance with the current. For currents with positive velocities, the changes of buoyancy frequency and density field are illustrated in Figure 3.11. N_L^2 needs to have a large at-surface value N_L^2 to balance out N_g^2 due to the current so that the total squared buoyancy frequency $N_L^2 + N_g^2$ is positive everywhere in the domain. We chose not to add other features, such as a pycnocline below the surface, to keep this relatively simple. We also show how the current alters the effective frequency in Figure 3.12.

Similar to 3.11, density fields are made for currents with negative velocities in Figure 3.13. N_g^2 can have a thick layer of negative value below the surface. On top of this, we prefer to use one stratification profile N_L^2 for a set of varying parameters, such as x_r and z_r related to the current. This requires us to choose a stratification profile N_L^2 with a thick pycnocline in the middle of the water column due to the negative N_g^2. Table 3.2 lists wavelengths λ, phase speeds c and group velocities c_g of mode-one waves for the various stratifications and f values. The modal structures of the horizontal velocities are plotted

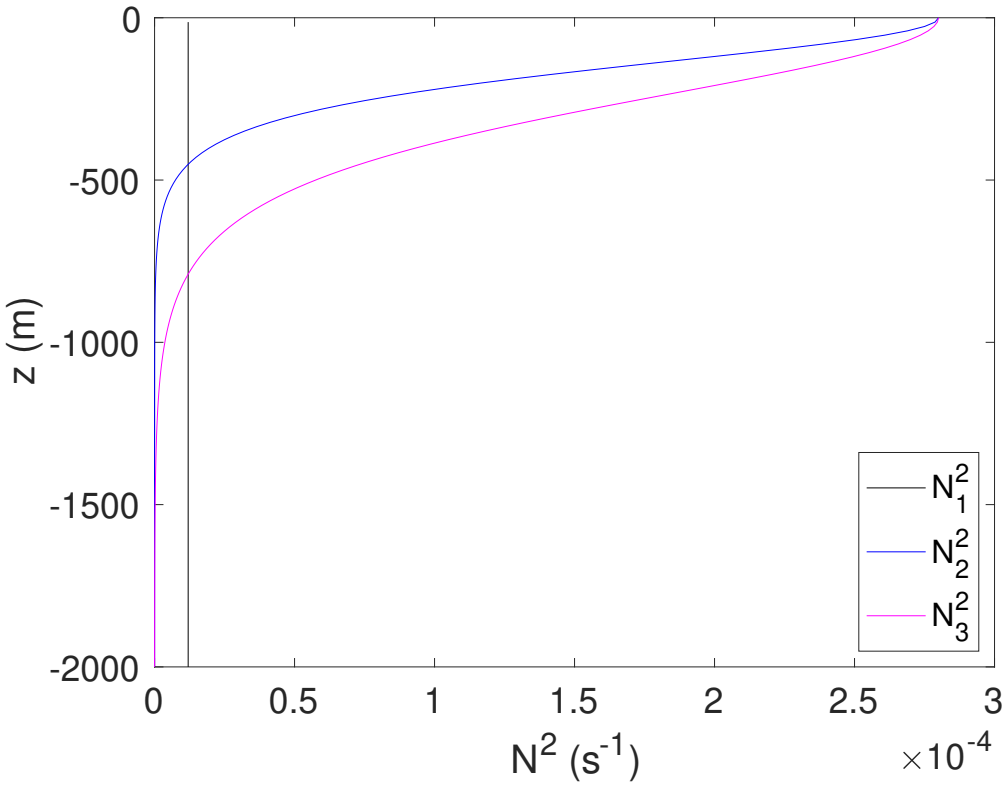

Figure 3.10: Stratification profiles used to the left of the current.

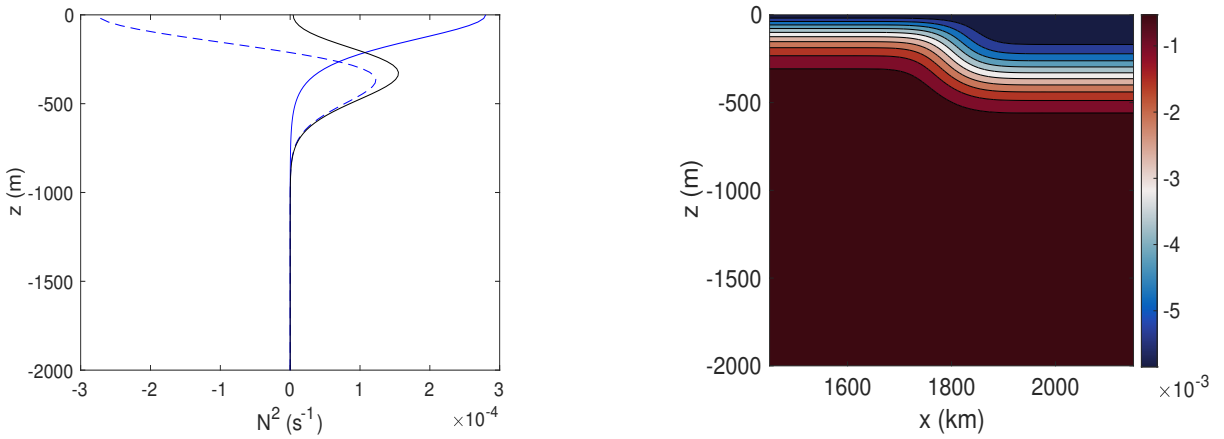

Figure 3.11: An example of the density field with the second stratification profile N_2^2 is presented, with V_{max} = 1.0 m/s, z_0 = 0, x_0 = 1800 km, x_r = 70 km, z_r = 300 m and $f = 1 \times 10^{-4}\,\mathrm{s}^{-1}$. a) A plot of buoyancy frequency squared at different locations. $N_g^2(x_0+2x_r, z)$ (blue dashed) is in geostrophic balance with the current. Note $N_g^2(x, z) = 0$ for $x < x_0 - 2x_r$. N_2^2 (blue solid) is the buoyancy frequency squared to the left of the current, where the IWs are forced. $N_g^2(x_0+2x_r, z) + N_2^2$ (black solid) is the total buoyancy frequency squared to the right of the current, which needs to stay positive for the flow to be stable. b) A contour plot of the total density field. Note the density field has been subtracted off the reference density ρ_0 and scaled by ρ_0 so it is dimensionless.

in figures 3.14, 3.15 and 3.16 for each stratification profile. Table 3.3 lists the model parameters. Since the near surface stratification of N_2^2 and N_3^2 is stronger than that of N_1^2, stronger currents can be simulated using N_2^2 and N_3^2.

All the simulations have similar features. We provide a detailed analysis for a case with N_1^2 using A = 0.02 m/s, $f = 10^{-4}s^{-1}$, V_{max} = -0.5 m/s, x_r = 45 km, z_r = 800 m and z_0 = 0. The parameters are typical for an along shelf current. In summary, for this case, we find that

- The interaction between the waves and the current is linear, confirming the validity of applying a linear decomposition to the IW field. The wave field is halved when A is reduced from 0.02 m/s to 0.01 m/s. An example of the horizontal velocities at the surface is plotted in Figure 3.17.

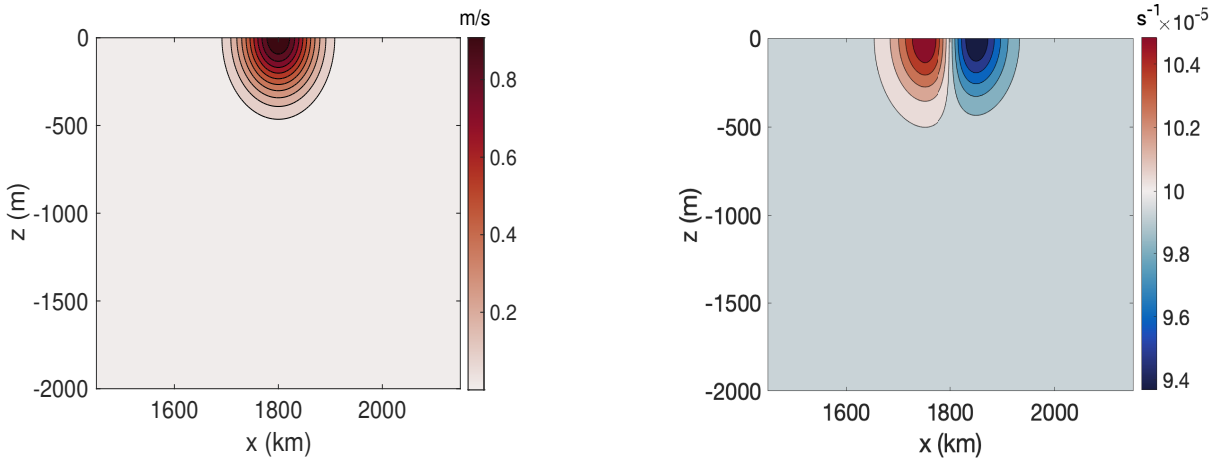

(a) (b)

Figure 3.12: a) The geostrophic current. This is the same current used to generate 3.11. b) The effective Coriolis frequency f_{eff} in the presence of this current. f_{eff} is raised to the left of the current center x_0 and it is lowered to the right of x_0. This pattern will be reversed if the sign of V_{max} is changed. Outside the current, $f_{eff} = f = 1 \times 10^{-4} s^{-1}$.

Table 3.2: Wavelengths λ, phase speeds c and group velocities c_g for mode-1 waves with the various stratification and f values. N_i^2 is the stratification to the left of the current.

	$f(s^{-1})$	$\lambda\ (km)$	$c\ (m/s)$	$c_g\ (m/s)$
N_1^2	1×10^{-4}	140	3.14	1.55
N_1^2	6×10^{-5}	109	2.44	2.0
N_2^2	1×10^{-4}	139	3.12	1.54
N_3^2	1×10^{-4}	228	5.1	2.52

Table 3.3: Parameter space

	$f(s^{-1})$	A (m/s)	V_{max} (m/s)	x_r (km)	z_r (m)	z_0 (m)
N_1^2	6×10^{-5} and 1×10^{-4}	0.01 and 0.02	[-0.5, 0.3]	[20, 200]	[300, 1000]	0 and -500
N_2^2	1×10^{-4}	0.02	[0.3, 1.0]	[28, 270]	[300, 950]	0
N_3^2	1×10^{-4}	0.02	[0.7, 2.5]	[30, 320]	[500, 1100]	0

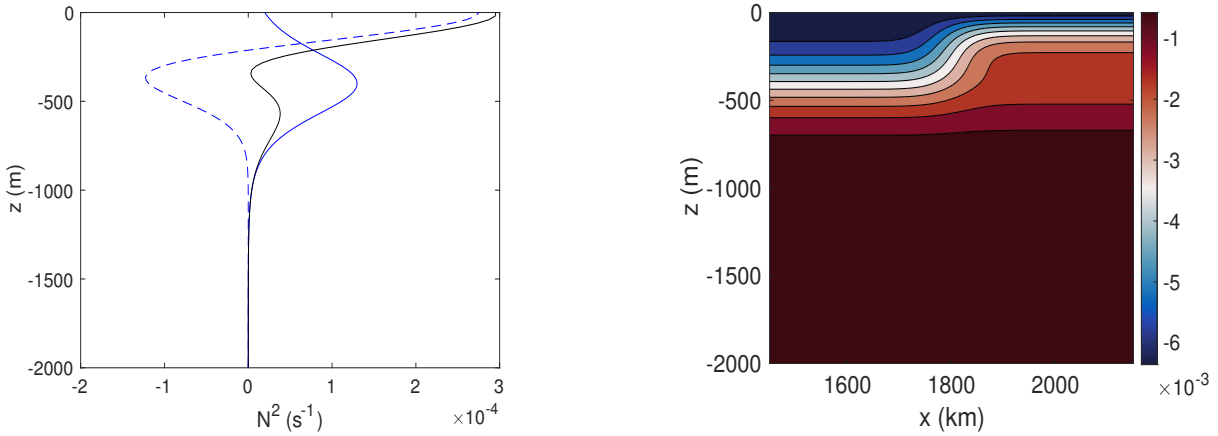

Figure 3.13: An example of the density field for V_{max} = -1 m/s, $z_0 = 0$, $x_0 = 1800\,\text{km}$, $x_r = 70\,\text{km}$, $z_r = 300\,\text{m}$ and $f = 1 \times 10^{-4}\,\text{s}^{-1}$. a) A plot of buoyancy frequency squared at different locations. $N_g^2(x_0 + 2x_r, z)$ (blue dashed) is in geostrophic balance with the current. Note $N_g^2(x, z) = 0$ for $x < x_0 - 2x_r$. N_L^2 (blue solid) is the buoyancy frequency squared to the left of the current. Note this N_L^2 is for demonstration only and is not used in any of the simulations. $N_g^2(x_0 + 2x_r, z) + N_L^2$ (black solid) is the total buoyancy frequency squared to the right of the current, which needs to stay positive for the stratification to be stable. b) A contour plot of the total density field. Note the density field has been subtracted off the reference density ρ_0 and scaled by ρ_0 so it is dimensionless.

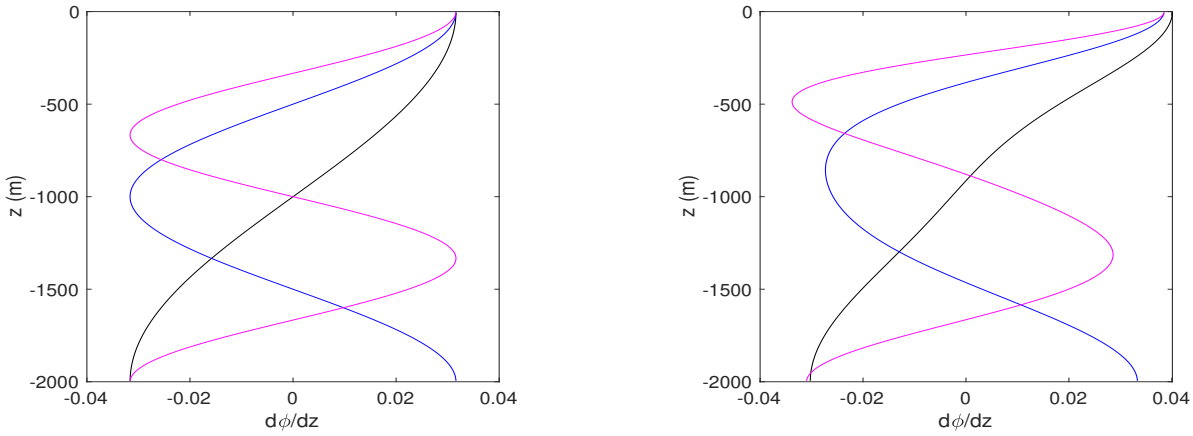

Figure 3.14: Horizontal velocity modal structures $\frac{d\phi_n}{dz}$ for n=1 (black), 2 (blue) and 3 (magenta) are plotted to the left of the current (left panels) and to the right of the current (right panels). $N_L^2 = N_1^2$. V_{max} = -0.5 m/s, x_r = 45 km and z_r = 800 m. $\frac{d\phi}{dz}$ is scaled so that $\int_{-H}^{0}(\frac{d\phi}{dz})^2\,dz' = 1$.

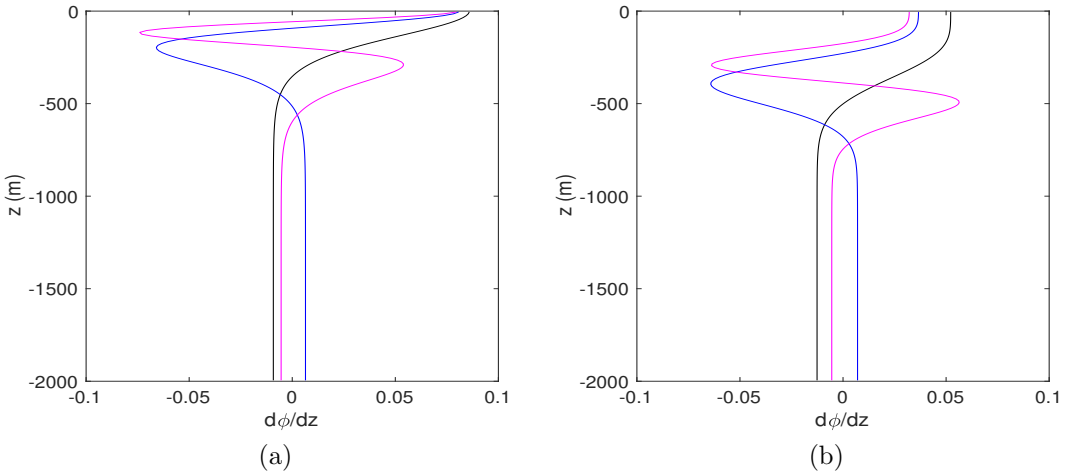

Figure 3.15: Same as 3.14, except $N_L^2 = N_2^2$. V_{max} = 1 m/s, x_r = 70 km and z_r = 300 m.

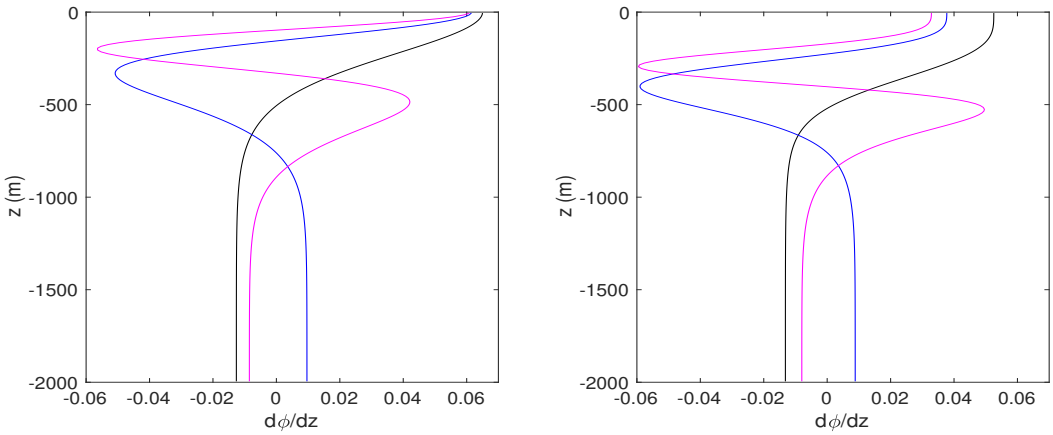

Figure 3.16: Same as 3.14, except $N_L^2 = N_3^2$. $V_{max} = 1$ m/s, $x_r = 70$ km and $z_r = 300$ m.

- Almost all of the incident wave energy is able to propagate through the current with a reflection coefficient of $R = 2.4$ %.
- The energy transfer between the current and the waves is negligible. Linear theory predicts the energy conversion takes place on the order of the second-order gradients of the current, which are small in this case and all other cases. We verify this by conducting a separate simulation so that all the parameters are the same except a wave packet is sent into the current. The total energy of a region containing the current is calculated before and after IWs propagate through the current, and the difference is negligible.
- A plot of the horizontal velocity amplitudes of the first four modes at the end of 47 tidal periods is provided in Figure 3.18. Mode-2 waves with wavelength of around 200 km are reflected from the current, as will be explained below. This wavelength matches that in figure 3.3 and only seems to appear to the left of the current. A further analysis shows this wavelength corresponds to a wave frequency $\sigma_L = 1.05 \times 10^{-4}$ s $\approx 0.75\sigma_0$, which is approximately the maximum f_{eff} inside the current. Linear theory predicts wave reflection when $\sigma < f_{eff}$. Note the reflected mode-two waves are larger than the incident mode-two waves (see previous section), which implies that the current may have converted a small fraction of the mode-one waves into the reflected mode-two waves.

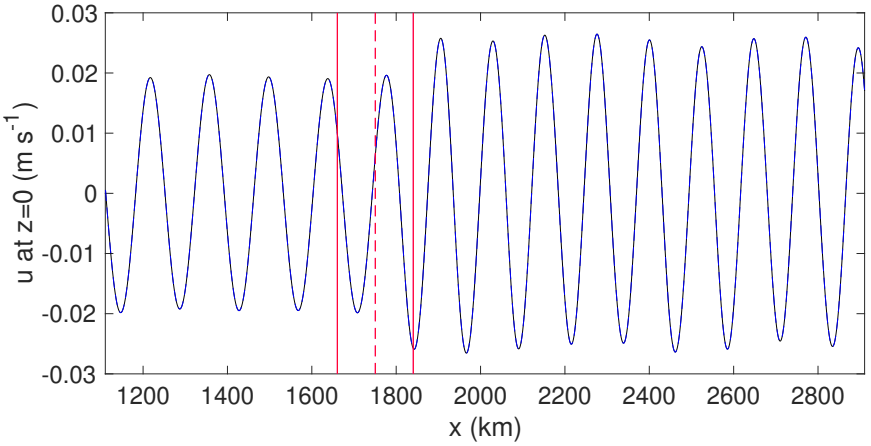

Figure 3.17: Horizontal velocities at the surface $z = 0$ at the end of the 60 tidal periods. Here $N_L^2 = N_1^2$, $f = 1 \times 10^{-4}\,\mathrm{s}^{-1}$, V_{max} = -0.5 m/s, $x_r = 45\,\mathrm{km}$, $z_r = 800\,\mathrm{m}$ and $z_0 = 0$. The two red lines are the edges of the current and the red dashed line is the center of the current. The black and the blue dashed lines represent $A = 0.02$ m/s and $A = 0.01$ m/s (scaled up by 2). The increased amplitude to the right of the current is due to the density change across the current which modifies the modal structure. It is not an indicator of increased energy.

- The fraction of the mode 2 energy to the right of the current is $P_2 = 1.6 \times 10^{-4}$. We compare this value with $P_2 = 3.2 \times 10^{-3}$ when z_0 = -500 m and all the other parameters stay the same. Lowering the center of the current increases the area of the interaction, increasing P_2. However, the exact relation between these two cases is not clear.

The reflection is generally small and R has a maximum value of 5% when $z_0 = 0$ for the three stratifications we considered. When the centre of the current is moved down to $z_0 = -500$ m the maximum value of R increases to 10 %. We will focus more on reflection in the next section where σ is lowered so that $f_{eff} \approx \sigma$ and strong reflection can occur. In all the simulations, P_n decreases with the modal number n. Only P_2 is considered, since P_3 is usually on the order of 10^{-4} or less. Increasing f or V_{max} alone generally increases P_2. For example, increasing f from $6 \times 10^{-5} s^{-1}$ to $1 \times 10^{-4} s^{-1}$ can increase P_2 by up to 10 times depending on the current parameters. This is because larger f or V_{max} results in a larger fV_z and hence a larger density gradient ρ_x, and a larger fV_x. Now if we fix f and V_{max}, we can plot contours of P_2 with respect to x_r and z_r (Figures 3.19, 3.20, 3.21). There is a range of x_r and z_r values that maximizes P_2. P_2 slowly decreases as x_r and

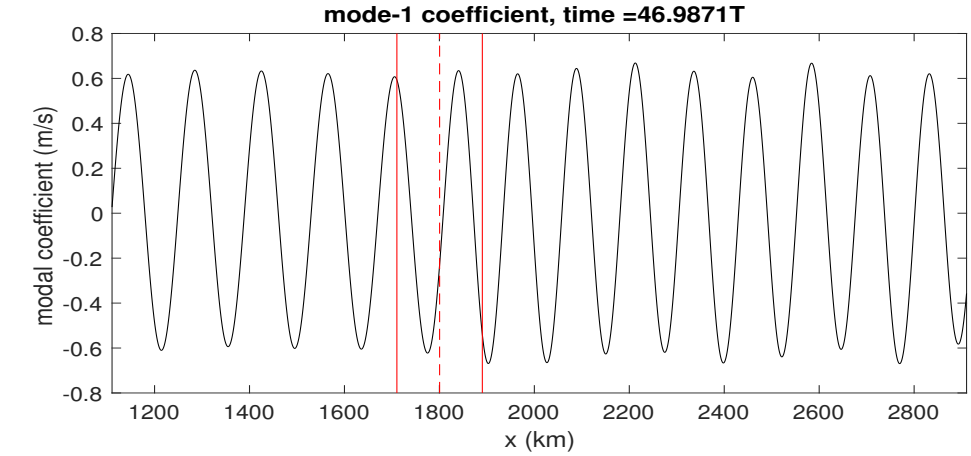

(a)

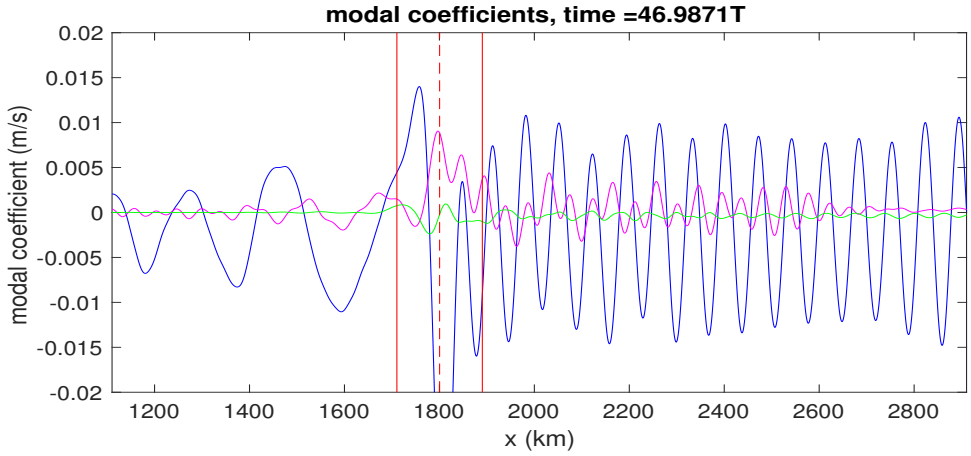

(b)

Figure 3.18: A plot of mode-1 (black), mode-2 (blue), mode-3 (magenta) and mode-4 (green) coefficients from the horizontal velocity at the end of 47 tidal periods. The parts of the domain with stretched grids are not included. Here $f = 10^{-4}s^{-1}$, V_{max} = -0.5 m/s, x_r = 45 km, z_r = 800 m, $z_0 = 0$ and $N_L^2 = N_1^2$. The red solid and dashed lines represent the edges and the center of the current, respectively.

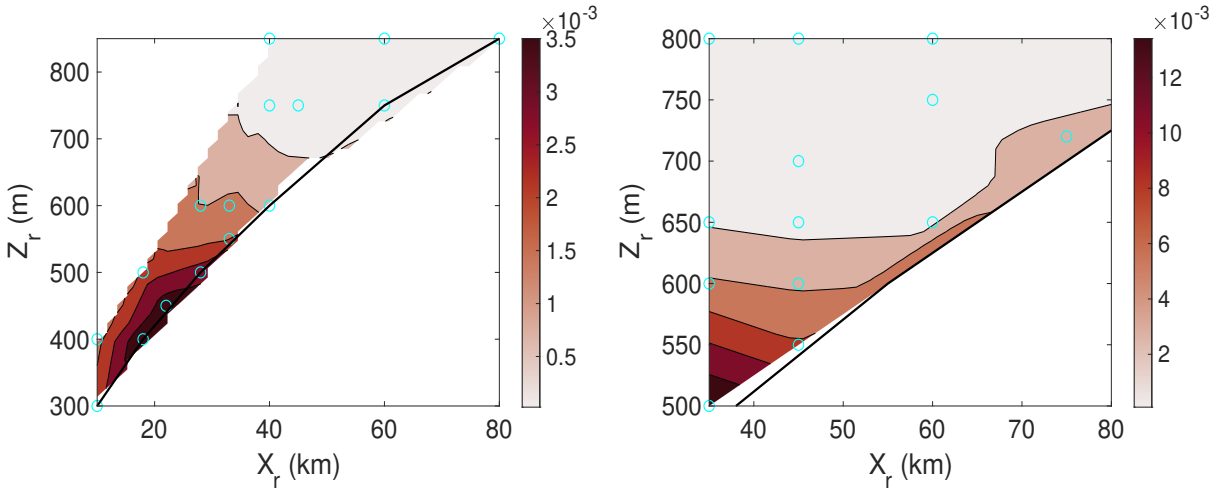

(a) $V_{max} = 0.3m/s$ (b) $V_{max} = -0.5m/s$

Figure 3.19: Contour plot of P_2 with respect to x_r and z_r. $N_L^2 = N_1^2$, $z_0 = 0$, $f = 1 \times 10^{-4}s^{-1}$. The empty circles are the simulation data and the color is a result of linear interpolation. The black line outlines the available parameter space for this stratification.

z_r move away from that region. We denote this point as (x_{m2}, z_{m2}), where 2 refers to the mode number.

Several more simulations with barotropic background currents $V_{max} = 1$ m/s for which the stratification does not vary across the current show very little modal energy transfer with $P_2 \approx 10^{-5}$ and relatively large reflection $R \leq 30\%$. This suggests that energy transfer to higher modes is mostly a result of IWs adjusting to the density gradients ρ_x. This with the previous results together implies that the major contribution to modal energy conversion comes from the combined effects of the size of the area in which the density varies horizontally, and the strength of ρ_x.

3.4 Strong reflections with baroclinic currents - $\sigma \approx (f_{eff})_{max}$

These are cases with blocking regions and cases on the edge of having a blocking region so that strong reflections are expected. We choose the incoming mode-1 waves to have diurnal frequency $\sigma = 7.026 \times 10^{-5}s^{-1}$ with amplitude $A = 0.02$ m/s. For these simulations we

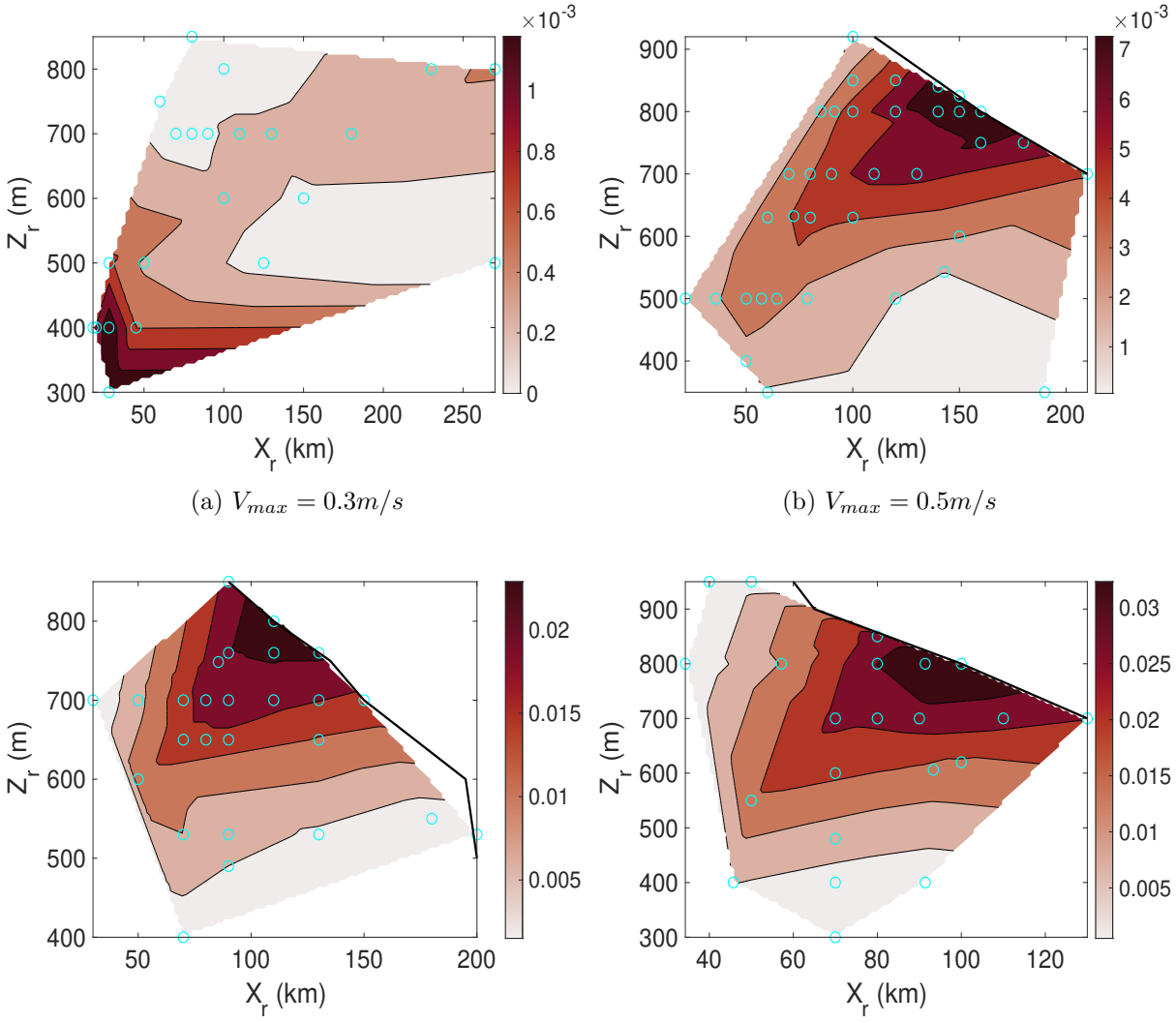

(a) $V_{max} = 0.3m/s$

(b) $V_{max} = 0.5m/s$

(c) $V_{max} = 0.7m/s$

(d) $V_{max} = 0.8m/s$

Figure 3.20: Same as Figure 3.19 but for $N_L^2 = N_2^2$.

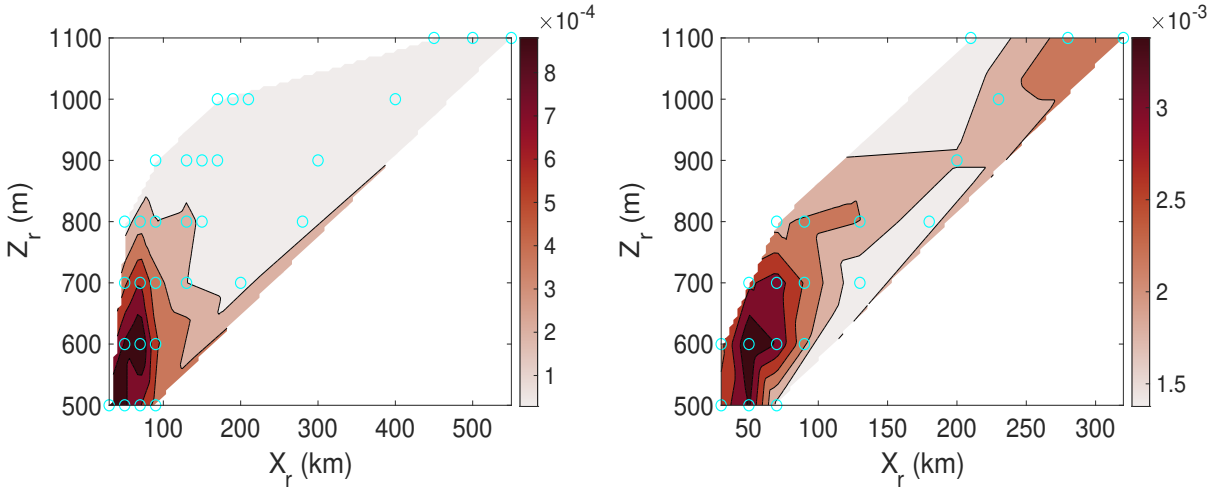

(a) $V_{max} = 0.7m/s$

(b) $V_{max} = 1.2m/s$

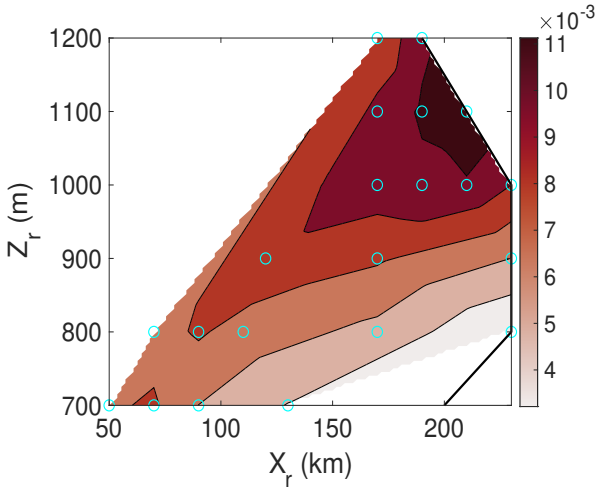

(c) $V_{max} = 1.8m/s$

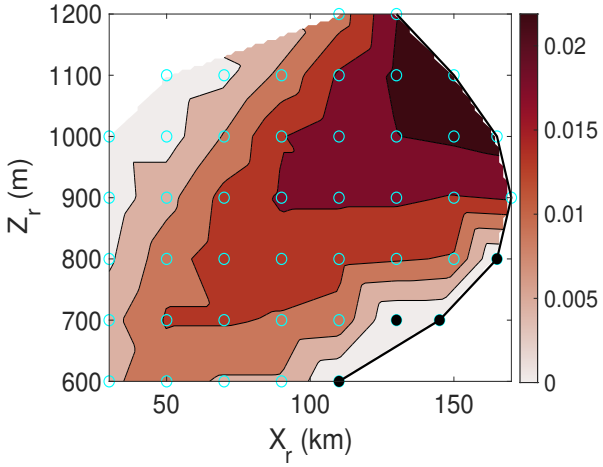

(d) $V_{max} = 2.5m/s$

Figure 3.21: Same as Figure 3.19 but for $N_L^2 = N_3^2$.

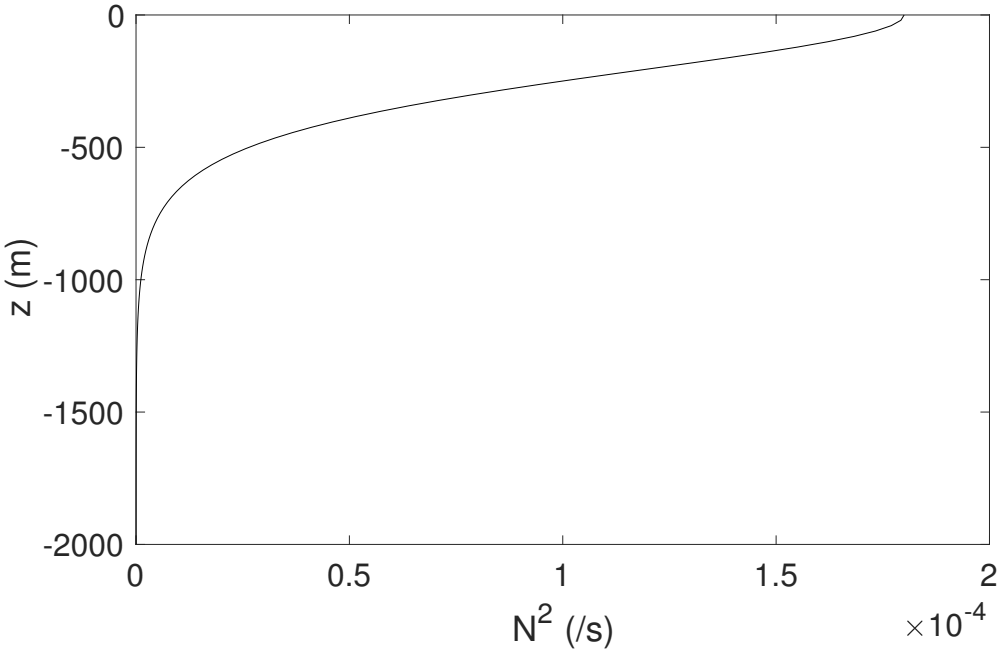

Figure 3.22: Stratification profile N_4^2.

use profile N_L^2 (Figure 3.22):

$$N_4^2 = 1.8\Big(\text{sech}(\frac{z}{310})\Big)^2 \times 10^{-4}/s \tag{3.87}$$

to the left of the current. N_4^2 has smaller surface values than our previous stratifications. This is because the internal waves forced here are near inertial waves with very long wavelength. Reducing N_L^2 decreases the wavelength and hence the computational domain. The wavelength of the ITs with N_4^2 is approximately 600 km. Note we cannot reduce the resolution for the longer waves in larger N_L^2, because we need enough resolution to describe the geostrophic current.

To test a series of negative currents, we require a stratification with a wide pycnocline in the middle of the water column, which is explained in the previous section. This is not a realistic stratification profile and it produces a very long IT wavelength making the simulation difficult. We simulated 15 negative currents using

$$N_5^2 = 8.0\Big(\text{sech}(\frac{z+600}{300})\Big)^2 \times 10^{-5} + 4.0\Big(\text{sech}(\frac{z+1500}{400})\Big)^2 \times 10^{-5}/s, \tag{3.88}$$

and $f = 6 \times 10^{-5} s^{-1}$. The incident IT wavelength is 742 km. Results from these negative currents have shown similar patterns and magnitudes of R and P_2 as the positive currents with N_4^2. For this reason, only currents with positive velocities are presented here. The current parameters are $V_{max} = 2.5$ or 1.8 m/s, $x_r \in [40, 230]$ km, $z_r \in [500, 1300]$ m and $z_0 = 0$. With $V_{max} = 2.5$ m/s, $f = 6.5 \times 10^{-5} s^{-1}$ as before, $\sigma < (f_{eff})_{max}$ for all the simulations. The blocking region is at least 75 km wide at the surface and the depth depends on the value of z_r. With $V_{max} = 1.8$ m/s, three values of f are used. $f = 6.5 \times 10^{-5} s^{-1}$, $6 \times 10^{-5} s^{-1}$ and $5 \times 10^{-5} s^{-1}$. We chose to use more f values for $V_{max} = 1.8$ m/s because this is a more realistic current speed compared to $V_{max} = 2.5$ m/s. Corresponding to the f values, σ is larger than $(f_{eff})_{max}$ when $x_r \leq 141$ km, 69 km and 32 km, respectively. An example of how the current affects the density field and the effective frequency is plotted in 3.23. The IT propagates $s = 2500$ km before reaching the current. The domain of interest has a length of $L = 4000$ km. All simulations have been run for 80 tidal periods. Contour plots of the mode 2 wave generation P_2 and the reflection R are presented in Figures 3.24 ($V_{max} = 2.5$ m/s) and 3.25, 3.26, 3.27 ($V_{max} = 1.8$ m/s).

Previously we denote (x_{m2}, z_{m2}) as the point that maximizes P_2. We now denote (R_x, R_z) as the point that maximizes R. The results are summarized below.

- There exists a set of x_r and z_r values, denoted as (x_{m2}, z_{m2}) and (R_x, R_z), where P_2 and R are maximized, respectively. P_2 or R slowly decreases as x_r and z_r move away from that region. This pattern was also found in the weak reflection cases in section 3.3.

- When $V_{max} = 1.8$ m/s and $f = 6.5 \times 10^{-5} s^{-1}$, we have two sets of (x_{m2}, z_{m2}), where P_2 has a local maximum (Figure 3.25 a)). 1) The first point $p_1 = (x_{m2}, z_{m2})$ located at (70 km, 1300 m) coincides with (R_x, R_z). 2) The second point p_2, located at (140 km, 1000 m), lies on the line $\sigma = f_{eff}$. We have run an extra simulation with all the same parameters except the current is barotropic. P_2 is now negligible and the reflection R has gone up from 32% to 41% due to the larger interaction area where f_{eff} varies. This result indicates that the modal energy conversion P_2 mostly depends on the horizontal variation of the stratification, which requires vertical shear V_z. Note the z_{m2} value of p_2 is the same as the z_{m2} value for the other values of f (Figures 3.26 a and 3.27 a). Though f changes, the stratification profile to the left of the current N_L^2 and V_z still remain the same. The horizontal density variation $\rho_x \propto f V_z$ varies with f linearly. Decreasing f reduces ρ_x and P_2 but the pattern stays almost the same.

- In each of the three figures 3.25 (b), 3.26 (b) and 3.27 (b), R generally increases as x_r decreases (larger f_{eff}) and z_r increases (larger area with $\sigma < f_{eff}$). This is consistent

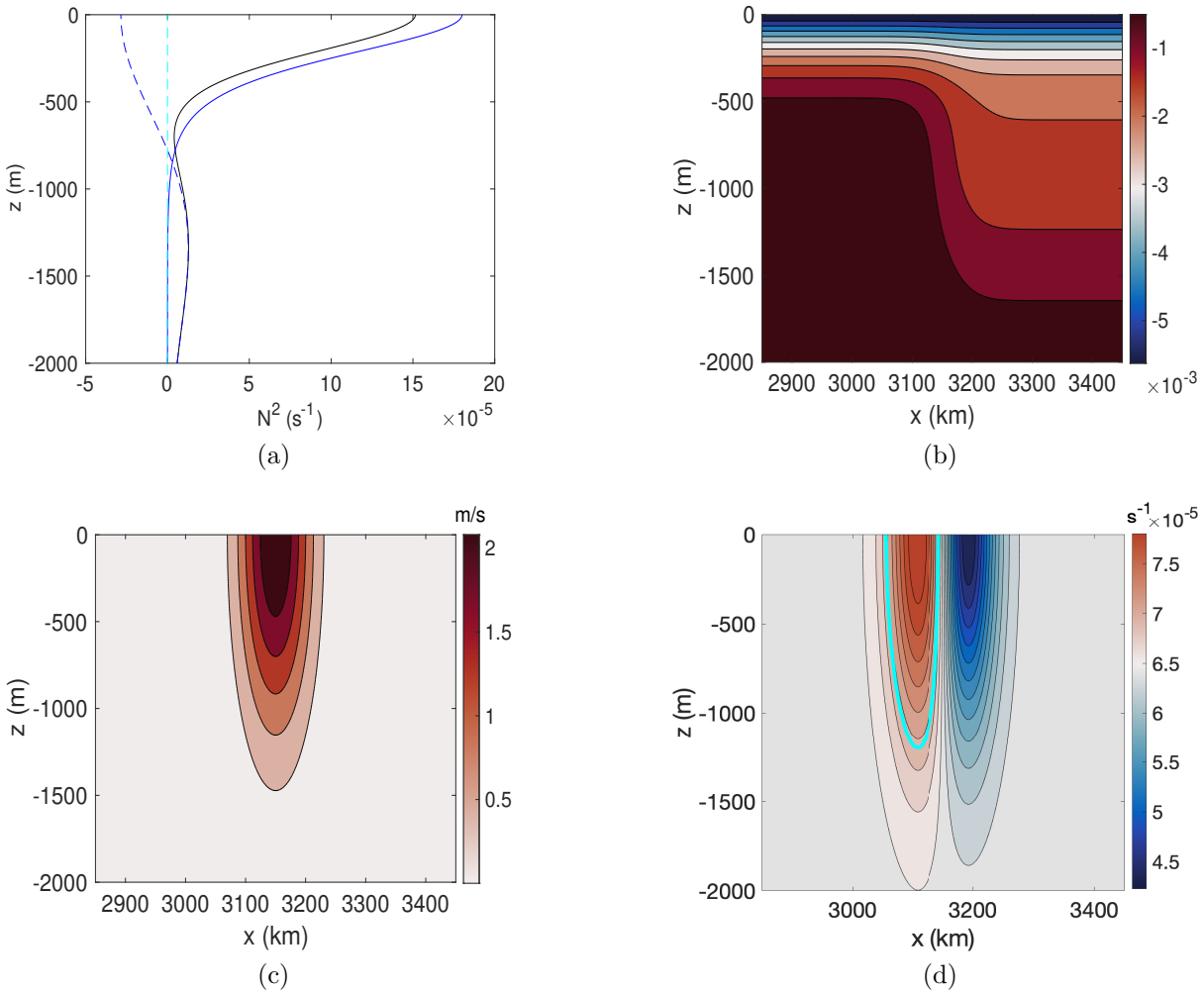

Figure 3.23: The current parameters are $V_{max} = 2.5$ m/s, $x_r = 60$ km, $z_r = 1100$ m, $x_0 = 3150$ km and $z_0 = 0$. a) A plot of buoyancy frequency squared at different locations. $N_g^2(x_0+2x_r, z)$ (blue dashed) is in geostrophic balance with the current. Note $N_g^2(x, z) = 0$ for $x < x_0-2x_r$. N^2 (blue solid) is the buoyancy frequency squared to the left of the current, where the IWs are forced. $N^2 = N_g^2(x_0 + 2x_r, z) + N_L^2$ (black solid) is the total buoyancy frequency squared to the right of the current, which needs to stay positive for the flow to be stable. $z = 0$ (cyan dashed) is plotted. b) The total density field in the presence of the current. c) The geostrophic current. d) The effective frequency f_{eff}. The cyan line marks $\sigma = f_{eff}$. The wave frequency used in this section is $\sigma = 7.026 \times 10^{-5} s^{-1}$. Outside of the current, $f_{eff} = f = 6.5 \times 10^{-5} s^{-1}$.

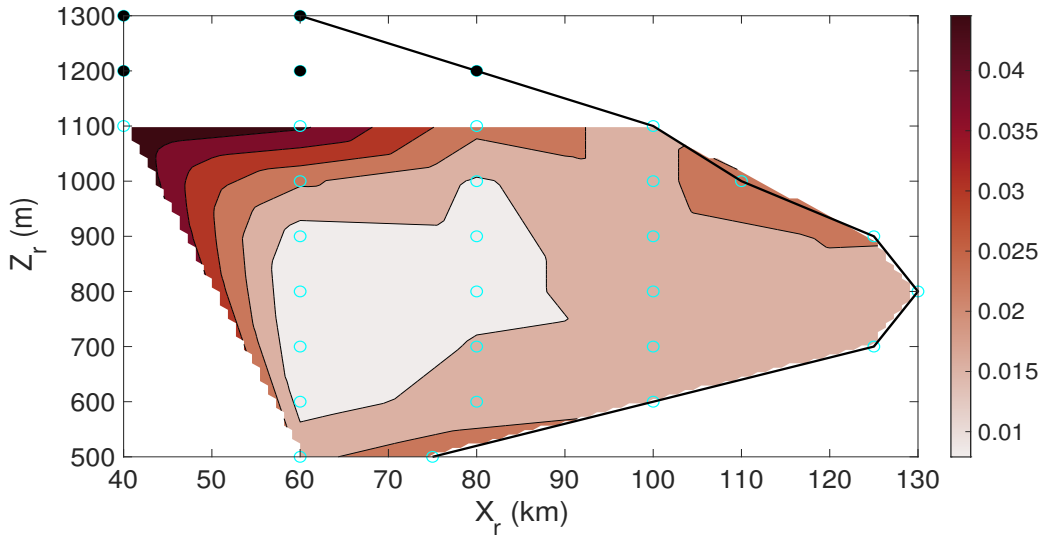

(a) $V_{max} = 2.5$ m/s. Mode 2 wave generation P_2.

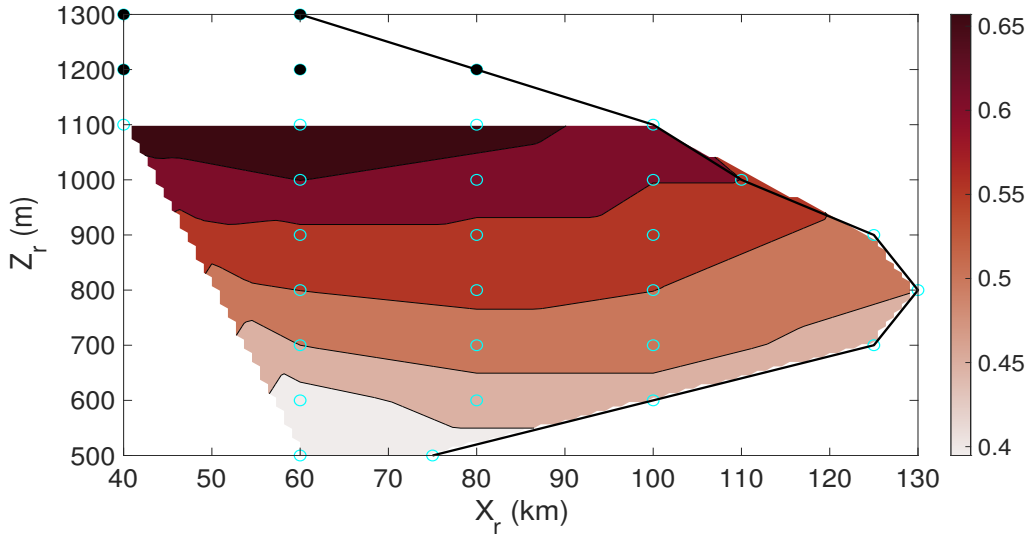

(b) $V_{max} = 2.5$ m/s. The reflection coefficient R.

Figure 3.24: The empty circles in the figures are the simulation data, and the color contours are the linear interpolation. The black solid line outlines the available parameter space according to this model set up. The wave frequency is always smaller than the maximum of the effective frequency, i.e., $\sigma < (f_{eff})_{max}$. The black solid circles represent cases where the simulation results are noisy.

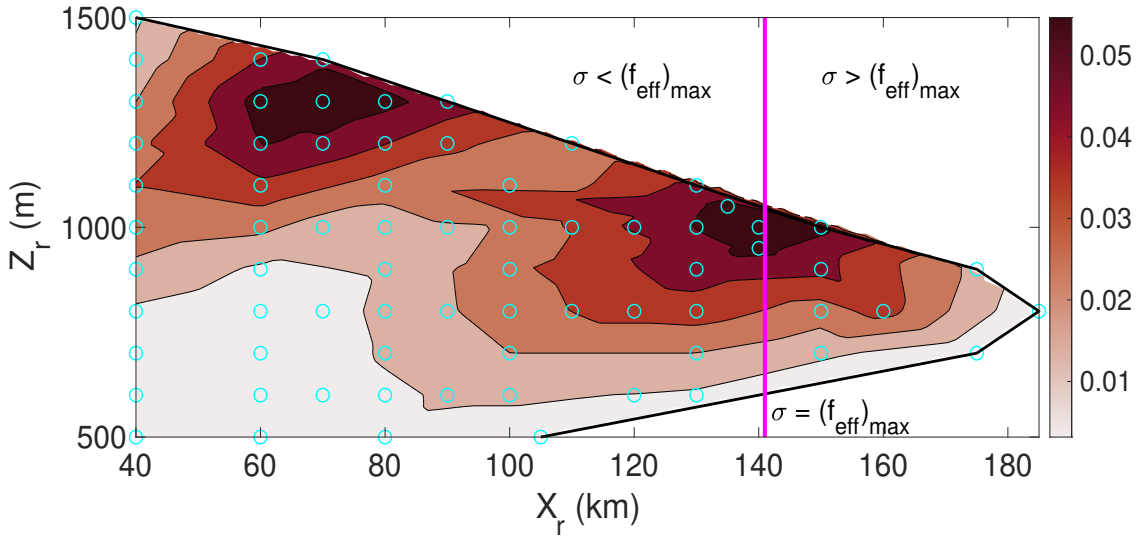

(a) $V_{max} = 1.8$ m/s. Mode 2 wave generation P_2.

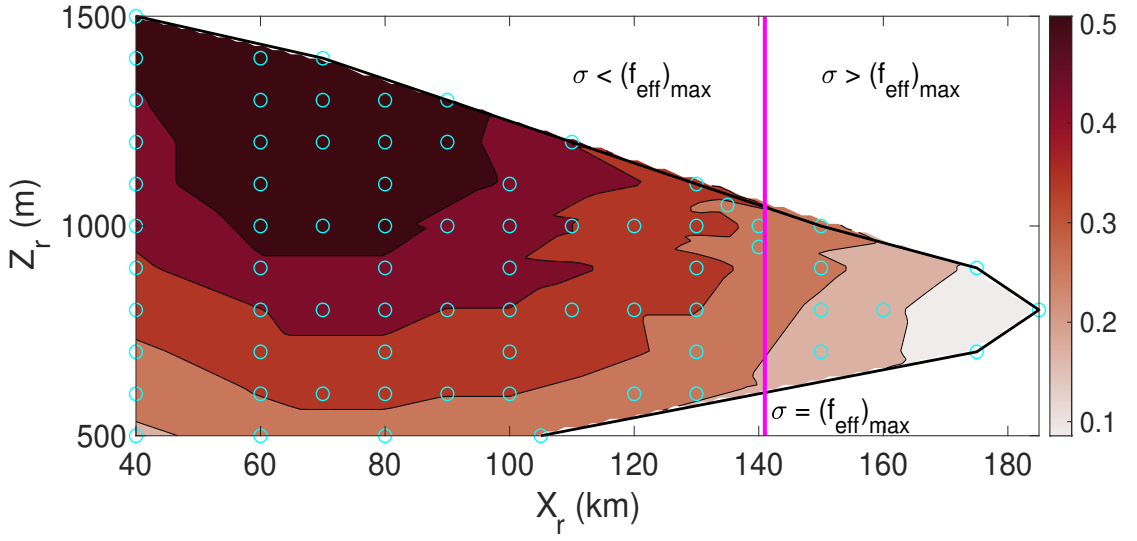

(b) $V_{max} = 1.8$ m/s. The reflection coefficient R.

Figure 3.25: $f = 6.5 \times 10^{-5} s^{-1}$. The empty circles in the figures are the simulation data, and the color contours are the linear interpolation. The black solid line outlines the available parameter space according to this model set up. The magenta line represents the value of x_r where $\sigma = (f_{eff})_{max}$. To the left of this line, $\sigma < (f_{eff})_{max}$.

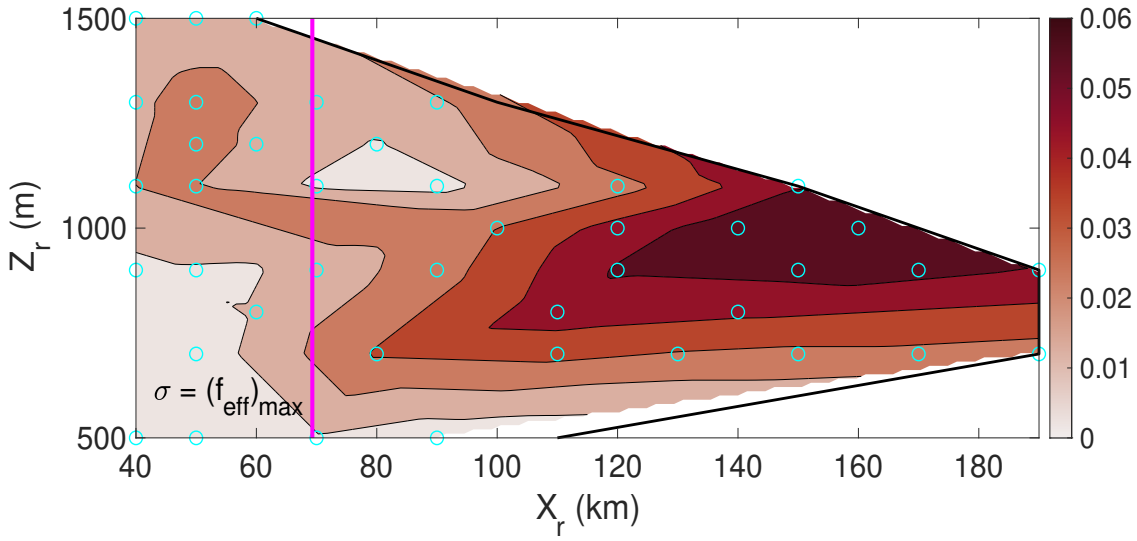

(a) $V_{max} = 1.8$ m/s. Mode 2 wave generation P_2.

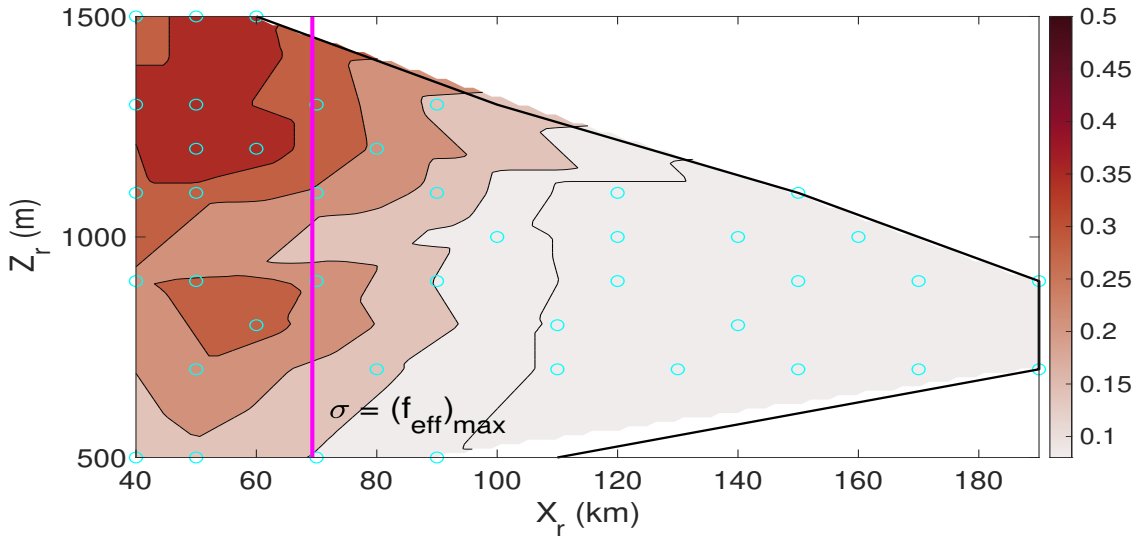

(b) $V_{max} = 1.8$ m/s. The reflection coefficient R.

Figure 3.26: Same as 3.25 except $f = 6 \times 10^{-5} s^{-1}$.

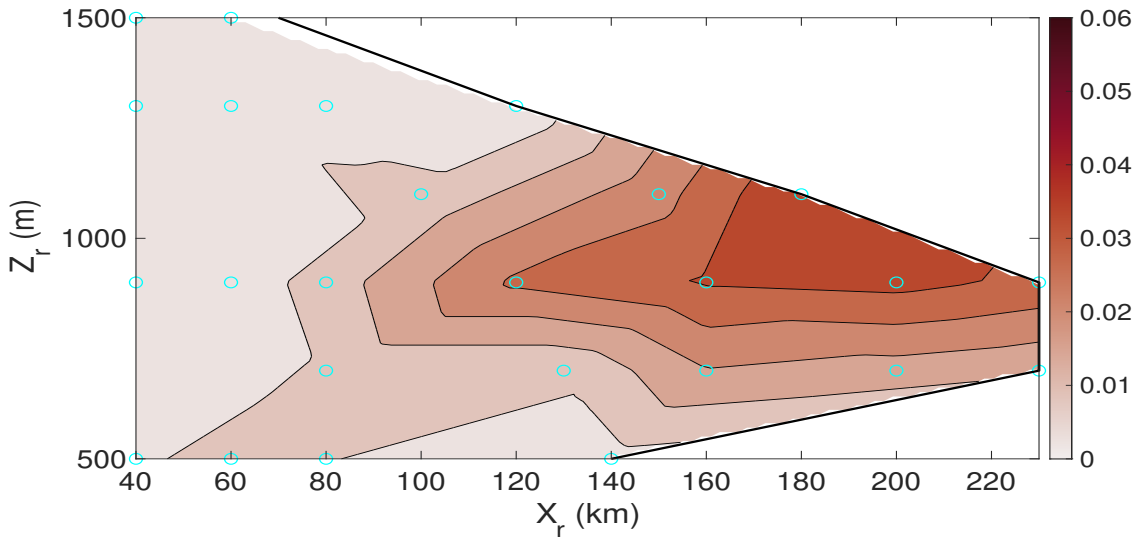

(a) $V_{max} = 1.8$ m/s. Mode 2 wave generation P_2.

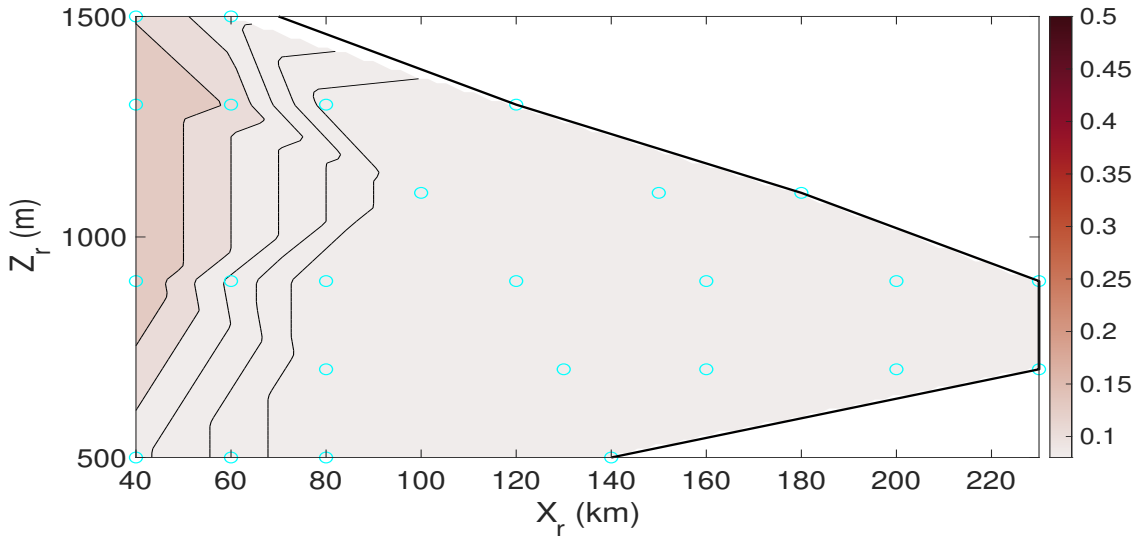

(b) $V_{max} = 1.8$ m/s. The reflection coefficient R.

Figure 3.27: Same as 3.25 except $f = 5 \times 10^{-5} s^{-1}$.

with our conclusions in the linear theory, though it is formulated based on barotropic currents. R is determined by the effective frequency f_{eff} and how quickly f_{eff} varies horizontally and vertically.

- Both P_2 and R decrease as f decreases (Figures 3.25, 3.26, 3.27). This is expected because decreasing f decreases the horizontal density variations $(\rho_g)_x \propto f$ and the effective frequency $f_{eff} = \sqrt{f^2 + fV_x}$.

- Compared to the weak reflection cases $\sigma \gg (f_{eff})_{max}$ in the previous section, cases here ($\sigma \approx (f_{eff})_{max}$) have a much larger reflection rate R and generally a larger modal energy conversion P_2.

- If we only vary V_{max}, larger V_{max} yields a larger reflection R but not necessarily a larger P_2. This is different from the conclusion in the previous section. For example, if we fix $f = 6.5 \times 10^{-5} s^{-1}$, $[x_r, z_r] = [130$ km, 800 m$]$, $[R, P_2] = [50\%, 1.7\%]$ and $[34\%, 4\%]$ for $V_{max} = 2.5$ and 1.8 m/s, respectively. The explanation is similar to that in our previous argument: larger reflection results in less energy available for modal conversion, which may reduce P_2.

- The reflection coefficient R can go up to 50% while the maximum of the modal energy conversion P_2 is only around 6%.

- When $f = 5 \times 10^{-5} s^{-1}$ and $x_r \leq 60$ km (Figure 3.27), there are regions over the slope where $f_{eff} < \sigma/2$. P_2 is small and we did not notice large deformation of the wave field. This confirms the results in previous works (Alford et al. [2007], Zhao et al. [2010], Hazewinkel and Winters [2011]) that parametric subharmonic instability (PSI) does not appreciably disrupt the propagation of the ITs even though f is below half the tidal frequency.

Chapter 4

The interaction of surface tide, topography and a geostrophic current

4.1 General set-up

Built upon the toy model in the previous chapter, we add an idealized bathymetry with a single slope and an along-shelf geostrophic current lying near the shelf break. Instead of forcing the ITs at the boundary, we force a diurnal K_1 barotropic current $\bar{U} = A\cos(\sigma t)$ at the western and eastern boundaries with $\sigma \approx 7.2935 \times 10^{-5} s^{-1}$. It has a period of 23.93 hours. $A = 0.02$ and 0.2 m/s in the deep water $H = 2$km and the shallow water $h = 200$ m respectively. A rigid lid is applied at the surface. The bathymetry $h(x)$ is modelled by:

$$h(x) = -H + \frac{s}{2}\Big(f(x, 0, d) - f(x, \frac{1800}{s}, d)\Big), \tag{4.1}$$

and

$$f(x, a, s) = \begin{cases} 0, & \textit{if } \frac{x-a}{s} < -20, \\ 2(x-a), & \textit{if } \frac{x-a}{s} > 20, \\ x - a + s\Big(\ln\big(\cosh(\frac{x-a}{s})\big)\Big) & \textit{otherwise.} \end{cases} \tag{4.2}$$

The bottom of the bathymetry starts at around $x = 0$. s is the slope of the bathymetry except near the shelf break and the bottom, where it is smoothed out via the parameter $d = 5000$ m. We use a Gaussian function to model the barotropic current (Figure 4.1a),

$$V(x) = V_{max} \exp\Big(-\frac{(x - x_0)^2}{x_r^2}\Big). \tag{4.3}$$

Table 4.1: Parameter space.

$f(s^{-1})$	γ (no current)	s	V_{max} (m/s)	x_0 (km)	x_r (km)
6.7×10^{-5}	0.029	0.023	-1 and 1	36 and 50	[40, 75]
6.0×10^{-5}	0.041	0.033	[-2, 2]	[13,43]	[15, 75]
5.0×10^{-5}	0.053	0.042	[-0.2, 2]	[15, 37]	[4, 40]

The parameters that can be varied under this setting are:

$$\begin{aligned} f: &\quad \textit{the Coriolis parameter,} \\ s: &\quad \textit{the slope of the bathymetry,} \\ x_0: &\quad \textit{the location of the center of the current,} \\ V_{max}: &\quad \textit{the velocity of the geostrophic current at } x = x_0\ , \\ x_r: &\quad \textit{this determines the width of the current.} \end{aligned}$$

We use a linear stratification for which the buoyancy frequency square is constant $N^2 = 1 \times 10^{-6} s^{-1}$ (Figure 4.1b). The slope of an internal wave characteristics under the hydrostatic approximation is

$$\gamma = \sqrt{\frac{\sigma^2 - f_{eff}^2}{N^2}}. \tag{4.4}$$

Here $f_{eff}^2 = f^2 + fV_x$ is the effective Coriolis frequency squared. We consider bathymetries with slope s so that in the absence of a current, $\frac{s}{\gamma} \approx 0.8$ (Figure 4.2). The values of the relevant parameters are listed in Table 4.1.

The central domain of interest has a length $L = 200$ km with uniform resolution $dx = 25$ m. The vertical grid is nonuniform with a total of $nz = 400$ points, in which 80 points are in the shallow water. The finest resolution $dz = 2.5$ m in the upper 200 m and it linearly stretches to $dz = 8$ m in the deep water (Figure 4.3). Analogous to our set up in the previous flat bottom cases, on either side of the central domain there is a layer in which the grid is slowly stretched horizontally with successive grid cell lengths increased by 0.5 %.

The horizontal viscosity is parameterized with a nonlinear Smagorinsky scheme (Smagorinsky [1993])

$$A_{hsmag} = \left(\frac{\text{Smag}}{\pi}\right)^2 (dx)^2 \sqrt{u_x^2 + v_x^2} \tag{4.5}$$

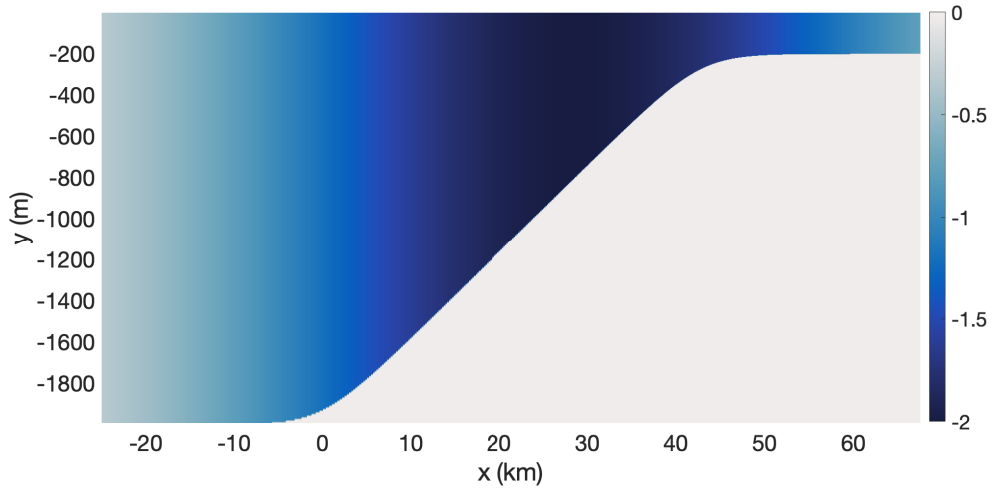

(a)

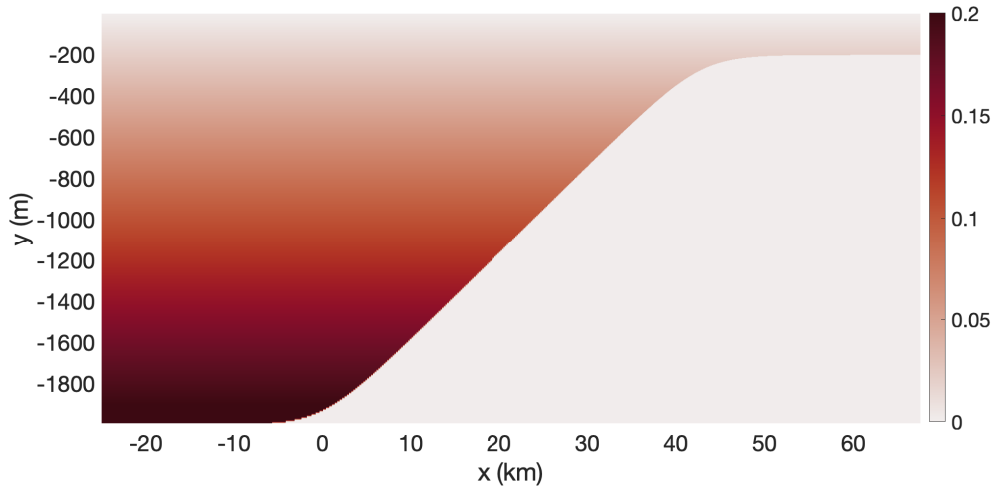

(b)

Figure 4.1: $f = 5 \times 10^{-5} s^{-1}$ and the slope of the bathymetry $s = 0.042$. a) Plot of a Gaussian barotropic current with V_{max} = -2 m/s, $x_0 = 29$ km and $x_r = 40$ km. b) Plot of the initial density field. Units for the colorbar: a) m/s and b) dimensionless.

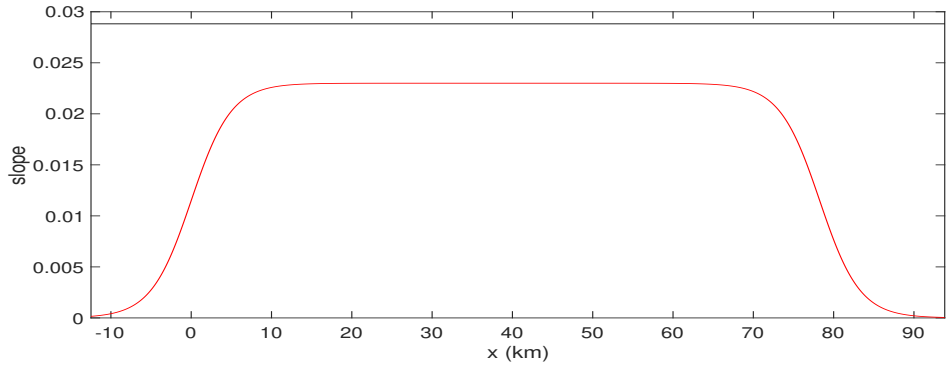

(a)

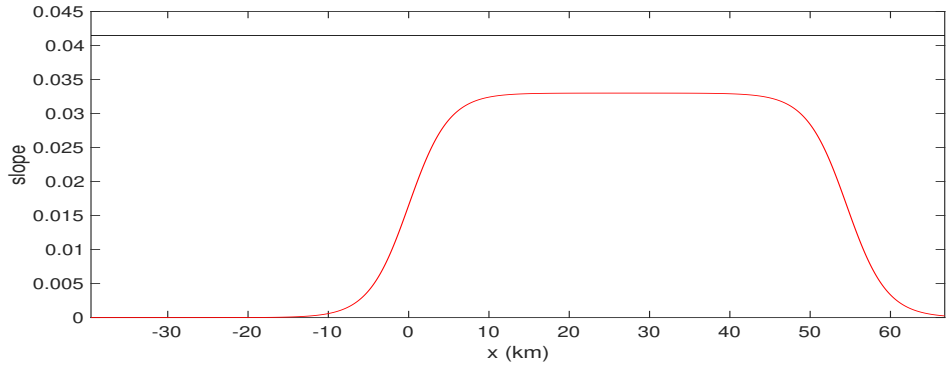

(b)

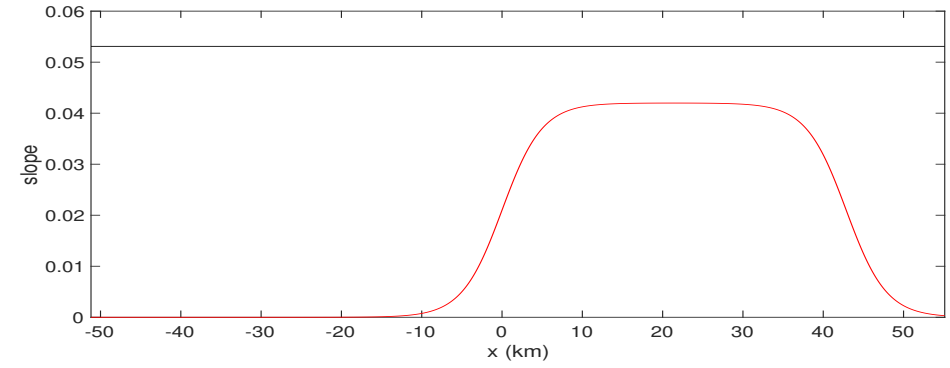

(c)

Figure 4.2: Plot of the IW wave characteristics γ (black) and the bathymetry (red) in the absence of geostrophic currents. a) $f = 6.7 \times 10^{-5} s^{-1}$, $\gamma = 0.029$, $s = 0.023$. b) $f = 6.0 \times 10^{-5} s^{-1}$, $\gamma = 0.041$, $s = 0.033$. c) $f = 5.0 \times 10^{-5} s^{-1}$, $\gamma = 0.053$, $s = 0.042$.

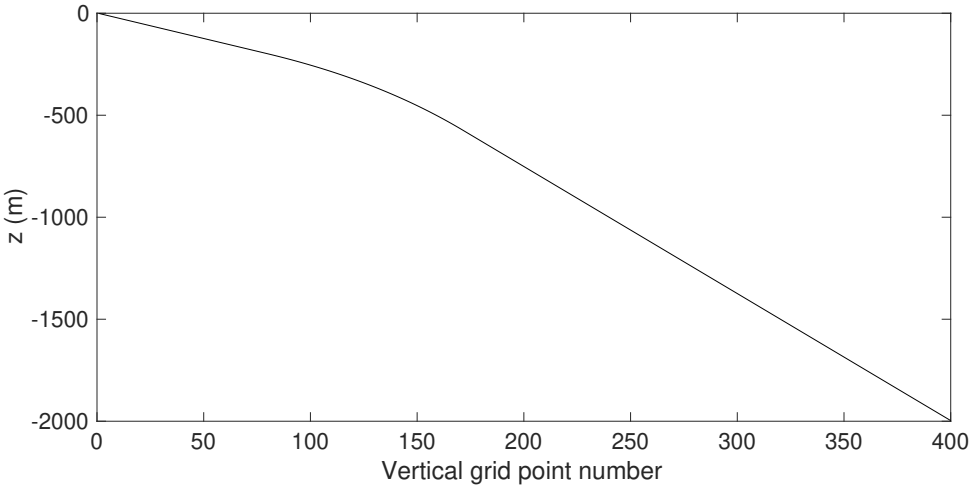

(a)

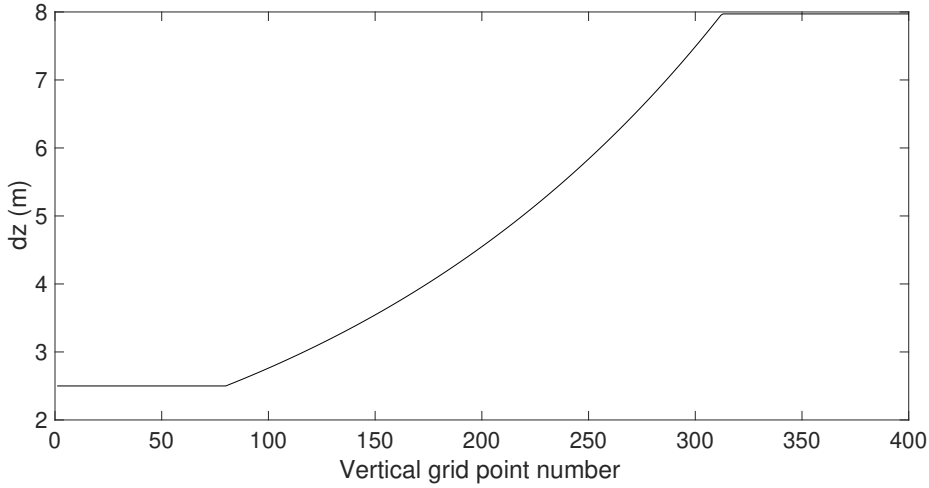

(b)

Figure 4.3: Plot of vertical grids shows (a) water depth varying with the grid point and (b) the grid resolution dz at each grid point, respectively.

with Smag = 2. We use PP81 to model the vertical viscosity μ and diffusivity κ (Pacanowski and Philander [1981]).

$$\mu = \frac{\mu_0}{(1+\alpha_0 \mathrm{Ri})^n} + \mu_b, \tag{4.6}$$

$$\kappa = \frac{\mu}{1+\alpha_0 \mathrm{Ri}} + \kappa_b. \tag{4.7}$$

Here $\mathrm{Ri} = N^2/(u_z^2 + v_z^2)$ is the Richardson number. $\mu_b = 10^{-5}\ m^2 s^{-1}$ and $\kappa_b = 10^{-5}\ m^2 s^{-1}$ are the background viscosities. $\mu_0 = 1.5 \cdot 10^{-2}\ m^2 s^{-1}$, $\alpha_0 = 5$ and $n = 1$ are the adjustable parameters (same parameters used in Stashchuk et al. [2017]).

Our analysis is mainly focused on 1) the conversion rate C and 2) the frequency of the generated baroclinic waves. C is defined previously in the section 1.3. We discuss the effect of an alongshore current on the magnitude and the pattern of C. We define the conversion rate C to be positive C_p when the energy is converted from barotropic to baroclinic flow, while it is negative C_n when the reverse topographic energy conversion takes place. Over the continental slope, the total conversion rate is positive but the local conversion can be either positive or negative. Since we have a rigid lid instead of a free surface, we will not be able to calculate the barotropic energy loss thus the percentage of the energy transferred to baroclinic waves. However, it is computationally cheaper to use a rigid lid and the aspects we are interested in are not altered in any essential ways.

4.2 Conversion rate C

The vertical average of the conversion rate $\overline{C}$ given by 1.100 is comprised of a linear term $\overline{\rho g W}$ and a nonlinear term $C_1 = U\left(\overline{u u_x} + \overline{w u_z}\right) + V\left(\overline{u v_x} + \overline{w v_z}\right)$. It has been shown (Kang and Fringer [2012]) that $\overline{C}$ is dominated by the linear term, which is also true for all the simulations we have done. We briefly verify this conclusion by using 3 cases with different f values (Figure 4.4). We approximate $\overline{C} = \overline{\rho g W}$ and drop the overbars in the rest of this chapter unless stated otherwise. All the values of the conversion rates are tidally averaged.

The current $V_g(x)$ has a direct impact on the slope of the IT characteristics γ and the slope criticality $\alpha = \frac{s}{\gamma}$. A separate set of simulations with different bathymetric slopes s were run to verify the importance of slope criticality α in determining the total conversion rate (Figure 4.5). No currents are included. Total C increases as the slope becomes critical. The leftward and right fluxes are listed in table 4.2. The leftward and rightward fluxes do not add up to the total conversion rate because of the dissipation.

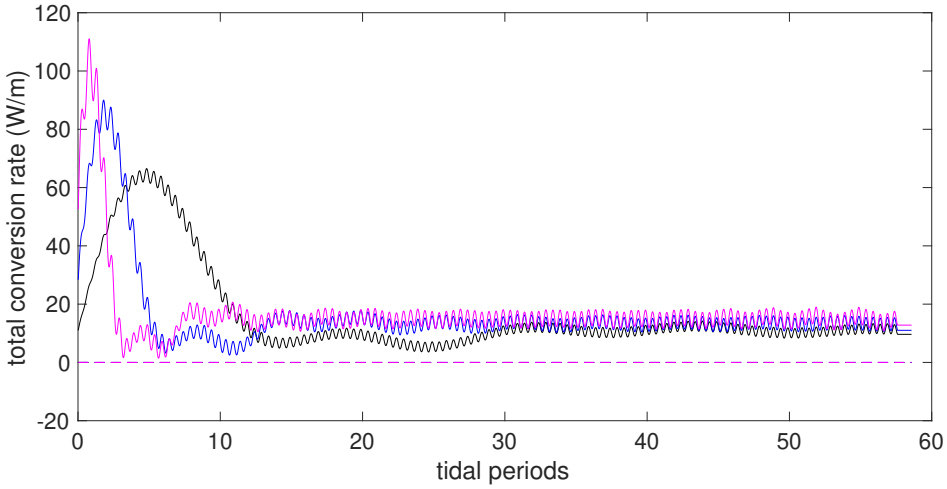

(a)

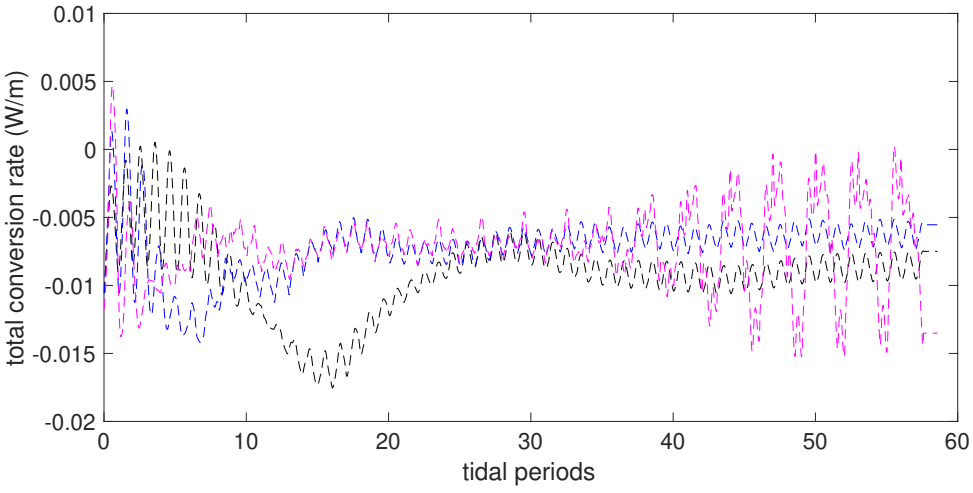

(b)

Figure 4.4: Total conversion rates (tidally averaged) integrated over the entire region. The linear and the nonlinear terms are represented by the solid and the dashed lines, respectively. Black lines: $f = 6.7 \times 10^{-5} s^{-1}$, $s = 0.023$. Blue lines: $f = 6.0 \times 10^{-5} s^{-1}$, $s = 0.033$. Magenta lines: $f = 5.0 \times 10^{-5} s^{-1}$, $s = 0.042$. No geostrophic currents.

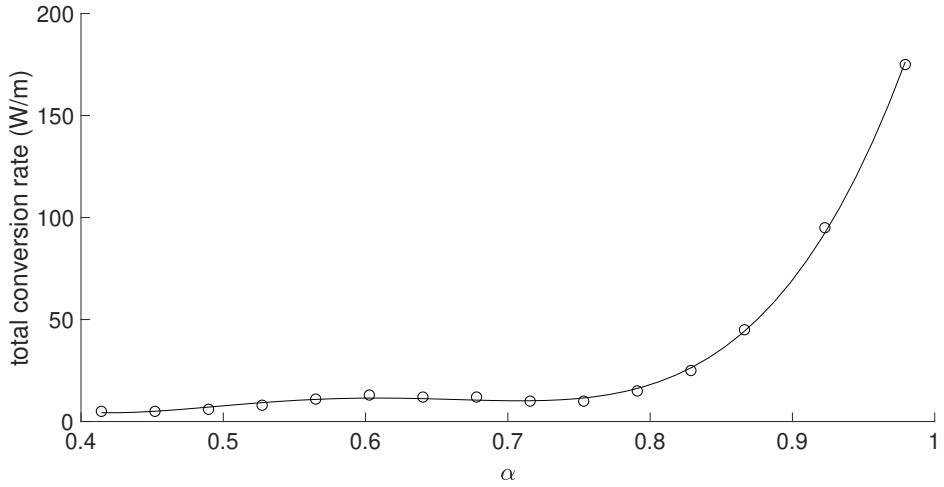

(a)

Figure 4.5: Total conversion rates for different slope criticality α. $f = 5.0 \times 10^{-5} s^{-1}$. The only variable is the bathymetric slope s, which is scaled by the IT characteristics γ to give α. The black empty circles represent the simulation data points, while the black solid line is a curve of best fit. No geostrophic currents.

Due to the large number of simulations done, only selected cases are presented here. The A and B series represent cases when $f = 6.7 \times 10^{-5} s^{-1}$ and $6.0 \times 10^{-5} s^{-1}$, respectively. Table 4.3 lists the parameters used for the two series. We define r_m as the part of the slope where $\alpha > 0.99\alpha_{max}$ and r_b as the x value of the location around which the beam is emitted. α_{max} is the maximum value of α. x_c and x_{c0} are critical points. The slope is supercritical (subcritical) to the left (right) of x_c, and vice versa for x_{c0}. A stretch of the slope with $f_{eff} > \sigma_T$ is called a blocking region. The slope criticality α is undefined in blocking regions. The details on f_{eff}, γ, C and $C_{p(n)}$ for each case are plotted in Figure 4.6. Viscosity tests were done for selected cases (Table 4.4). Generally if the viscosity is large, more energy is dissipated over the slope and less energy can propagate away from the generation site, leading to a smaller value of E_f/C.

4.2.1 Scenario I: no current

We begin with the simplest cases A0 and B0 for which there are no background currents (magenta solid lines in Figure 4.6). These provide a reference for cases with currents. The shelf slope lies between 0 and 81 (55) km for the A (B) series. We can see a large transient

Table 4.2: Comparison of baroclinic energy fluxes E_f and total conversion rates C. $f = 5.0 \times 10^{-5} s^{-1}$. No geostrophic currents.

Slope criticality	Total C (W/m)	Leftward E_f (W/m)	Rightward E_f (W/m)	Total E_f/C
0.98	175	110	2	64%
0.92	95	45	2.5	50%
0.87	45	20	2	49%
0.83	25	10	1.5	46%
0.79	15	4	2	40%
0.75	10	3	1.8	48%
0.72	10	3.7	2	57%
0.68	12	4.5	1.5	50%
0.64	12	5.6	1.5	59%
0.6	13	6	1.3	56%
0.57	11	4.5	1.2	52%
0.53	8	3	2	63%
0.49	6	1.9	1.75	61%
0.45	5	1.9	1.25	63%
0.42	5	2	1.25	65%

Table 4.3: Parameters in A and B series. V_{max}, x_0 and x_r are maximum velocity, the center and the width of the current. r_m is the part of the slope where $\alpha > 0.99\alpha_{max}$. x_c and x_{c0} are critical points. r_b is the x value of the location around which the beam is emitted.

f (s^{-1})	case	V_{max} (m/s)	x_0 (km)	x_r (km)	r_m (km)	x_c (km)	x_{c0} (km)	r_b (km)
6.7×10^{-5}	A0	NA			[5, 80]	NA	NA	20
	A1	1	50	60	blocking	45	NA	55
	A2	1	36	60	blocking	31	NA	41
	A3	1	64	60	blocking	59	0	69
	A4	1	92	60	blocking	77	7	80
	A5	-1	36	60	blocking	NA	50	65
6.0×10^{-5}	B0	NA			[5, 60]	NA	NA	20
	B1	1	41	40	[10, 14]	30	3	35
	B2	0.5	30	40	[8, 11]	NA	NA	25
	B3	-1	23	40	[47, 52]	53	31	53
	B4	-0.5	30	40	[42, 47]	NA	NA	45

Table 4.4: Viscosity tests. Horizontal viscosities are either Smag (Smagorinsky) or viscAh (constant viscosity). Vertical viscosities are chosen from pp81, KL10 or viscAz (constant viscosity). The suffix in the case numbers represents different viscosity choices based on the original case shown in the prefix, e.g. A0v1,...A0v8 are all based on case a0.

cases	Smag	viscAh	pp81	KL10	viscAz	C	Total E_f/C
A0	2	No	Yes	No	No	12	22 %
A0v1	1	No	Yes	No	No	7	34 %
A0v2	0	No	Yes	No	No	5	42 %
A0v3	0	0.2	Yes	No	No	7	29 %
A0v4	0	0.1	Yes	No	No	6	30 %
A0v5	2	No	No	Yes	No	7	31 %
A0v6	0	No	No	Yes	No	10	36 %
A0v7	2	No	No	No	10^{-5}	5	40 %
A0v8	2	No	No	No	10^{-4}	5	40 %
A5	2	No	Yes	No	No	30	47 %
A5v1	1	No	Yes	No	No	33	42 %
B0	2	No	Yes	No	No	13	35 %
B0v2	0	No	Yes	No	No	8	56 %

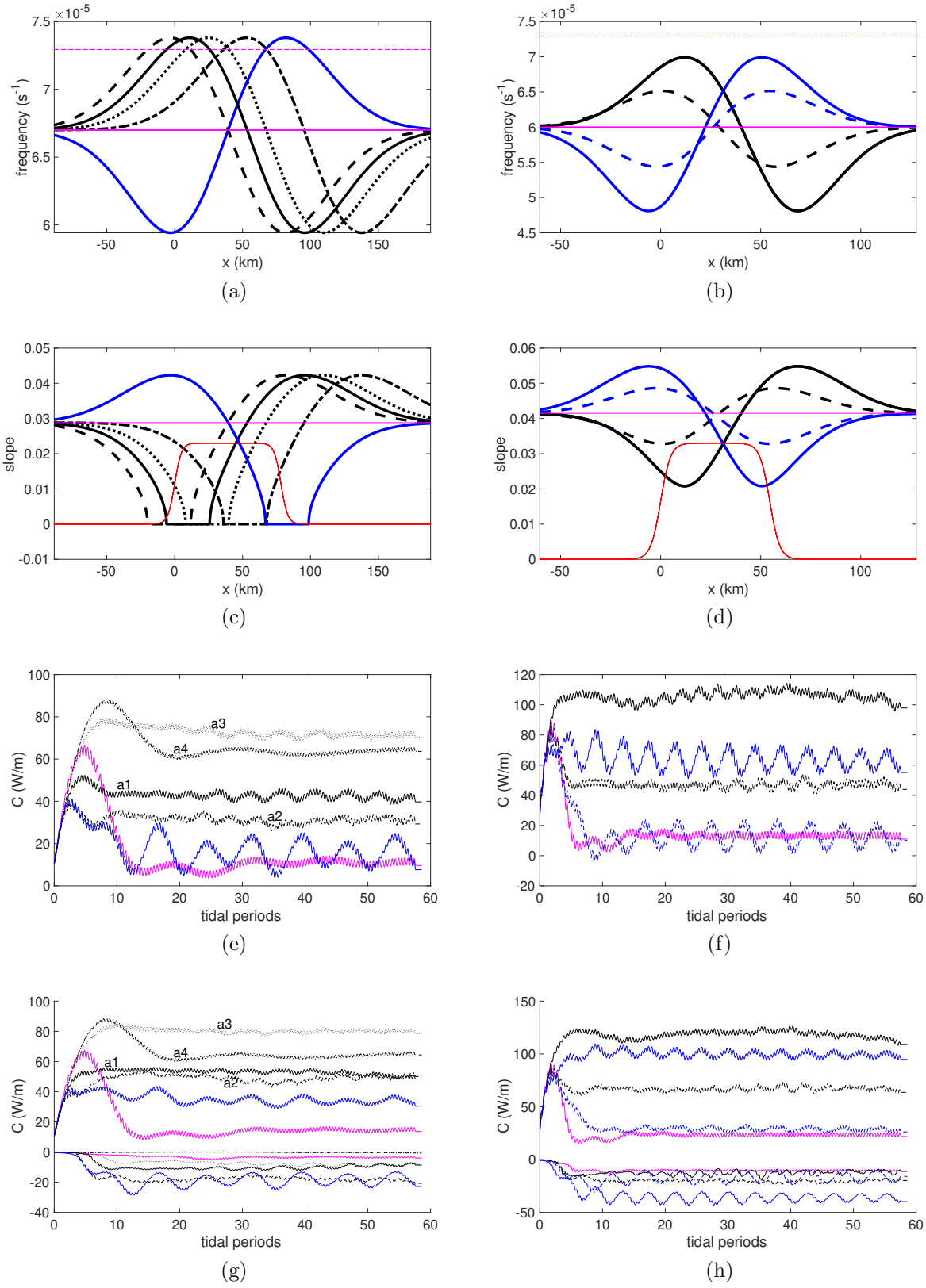

Figure 4.6: (a, b): Effective frequencies. Magenta dashed (solid) line is σ_T (f). (c, d): Slope of IT characteristics γ. The red line is the bathymetric slope. (e, f): Total conversion rates C. (g, h): C_p and C_n. Left column: A series. (Magenta, black, black dashed, black dotted, black dash-dot, blue) = (A0, A1, A2, A3, A4, A5). Right column: B series. (Magenta solid, black, black dashed, blue, blue dashed) = (B0, B1, B2, B3, B4).

behaviour in the time evolution of the conversion rate $\overline{C}$ (Figures 4.6 (e, f), 4.7 (a, b)). At the beginning of the simulations, the wave field needs time to adjust to the sudden onset of the tidal forcing. It takes about 10 and 5 tidal periods for A0 and B0 to reach a quasi-steady state. α is constant on the majority of the slope, and ITs are generated along the whole slope. The bathymetry is smoothed out near the bottom, so α is small near the base at $x = 0$ and near the shelf break and it has its maximum value at the centre of the slope. For these cases r_m is approximately the region [5 km, shelf break - 5 km]. For both cases IT beams are emitted from a neighbourhood of $r_b \approx 20$ km (Figure 4.7 (g, h)) approximately 100 m above the bottom (Figure 4.7 (c, d)). In those figures, the green circles mark the x value of the location r_b on the slope and beams are emitted from the area around it. The beam emanates slightly above the bathymetry because the slope is subcritical to the left of r_b and the beam on the left can only be emitted if the location is above the bottom. To the left of $r_b \approx 20$ km is a beam with $\vec{c}_g$ propagating to the base of the slope then reflecting up to the left, and to the right a more intense beam propagates to the upper right. Figures 4.7 (e, f) plot the horizontal baroclinic velocity u' as a function of time and selected water depths at a particular x-location. The plot does not indicate the scale of u' because these plots are only used to illustrate the phase not the magnitude of u'. The phase of the rightward beam propagates downward (Figure 4.7 (e, f)) and the energy goes upward until it hits the surface and gets reflected (Figure 4.7 (g, h)). The characteristic IT beam path shown in green (Figure 4.7 (c,d)) is in general calculated using a ray tracing technique although in the absence of a background current they are straight lines. The beam energy continues to propagate onshore while being reflected by the surface and bottom. The beams generated near r_m are a common feature in all of our simulations, and it is related to positive conversion C_p. Each time the beam reflects, the sign of the conversion $\overline{C}$ changes (Figure 4.7 (a, b)).

4.2.2 Scenario II: no critical point

We include a current $V(x)$ with relatively small V_x so that $\alpha < 1$ everywhere. We consider cases B2 and B4, which only differ in the sign of V_{max} (blue dashed and black dashed lines in the right column of Figure 4.6). Unlike the previous cases A0 and B0, the slope criticality α here varies along the slope due to the presence of the current. In B2 (positive current), α is increased (decreased) to the left (right) of the current center x_0. α reaches its maximum near the bottom at $r_m \approx 10$ km and its minimum is at $x \approx 50$ km. Two beams emanate from $r_b \approx 25$ km (Figure 4.8 (c, g)).This difference in the x-location between beam emission and α_{max} (r_b and r_m) is presumably due to the strengthening of the barotropic current with decreasing water depth. To the right of $r_b \approx 25$ km, the phase of the beam

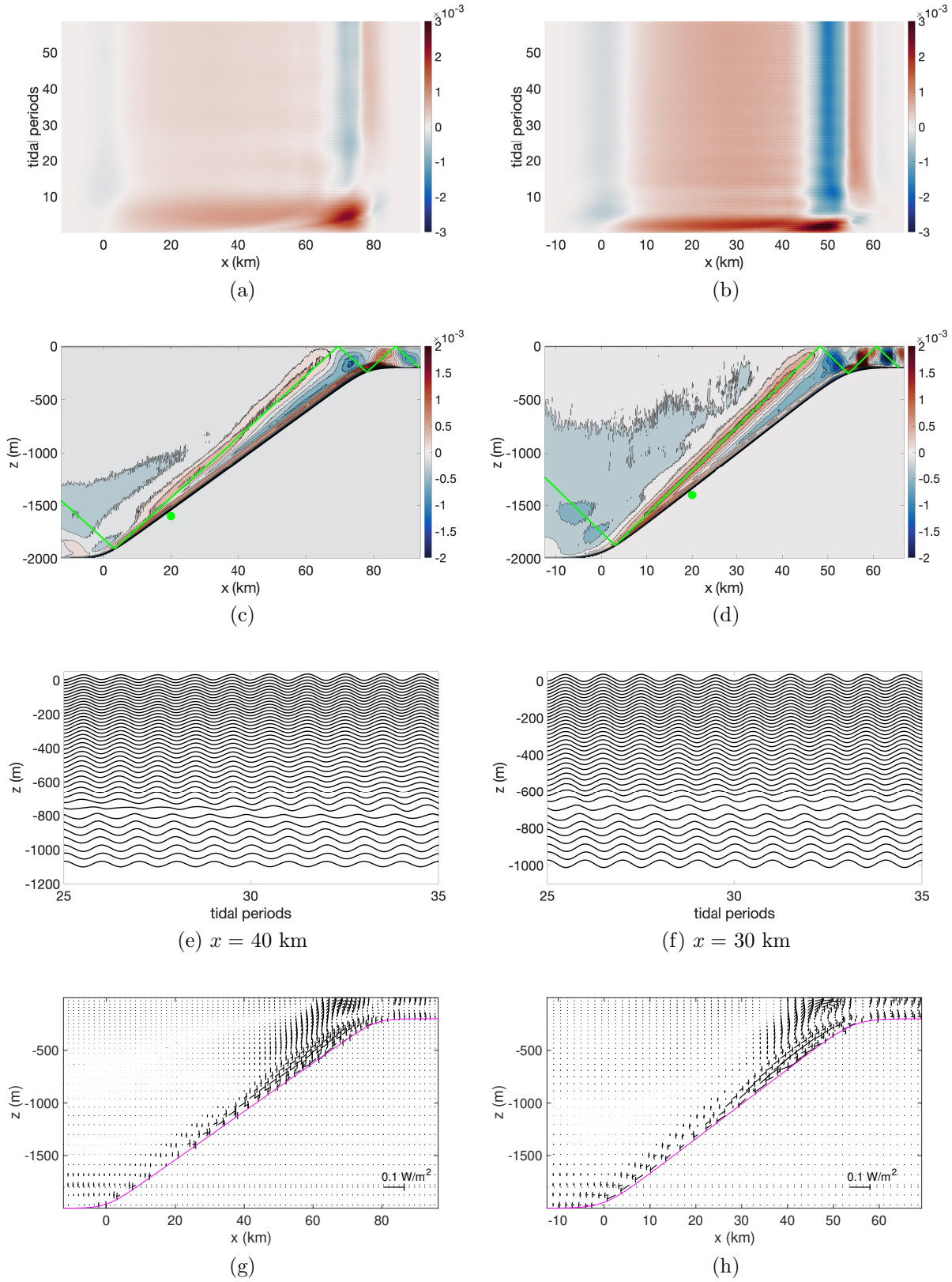

(a) (b) (c) (d) (e) $x = 40$ km (f) $x = 30$ km (g) (h)

Figure 4.7: Left column: case A0. Right column: case B0. (a,b) Contour plot of the vertical integration of $\overline{C}$ (W/m^2) varying on the spatial and time scale. (c,d) Contour of the density perturbation ρ' at the end of 30 tidal periods. Green lines are the characteristics of IT beams. Green circles mark the location where the beam is emitted. (e,f) The horizontal baroclinic velocity u'. (g,h) Energy flux $< (u', w')p' >$.

propagating downwards (Figure 4.8 (e)) indicates that energy propagates upwards (Figure 4.8 (g)). Note the slope of the beam is curved due to the varying f_{eff}. The beam is emitted from a location similar to that in case B0 but the slope is closer to critical with $\alpha_{max} =$ 0.97. As a result, the total conversion rate C in B2 is larger than in case B0 (black dashed line in Figure 4.6 (f)).

In B4 with V_{max} = -0.5 m/s, $\alpha_{max} = 0.97$ occurs near the shelf break ($r_m \approx 45$ km) and it is smallest at $x \approx 15$ km. Three beams are emitted from the left and right of $r_b \approx r_m$ (Figure 4.8 (d)) Since the slope is subcritical on both sides of r_b, for the left downward propagating beam to be generated, the generation location must be above the slope. To verify this beam pattern, an extra simulation was conducted in which the water depth was increased by 400 m everywhere and the deep water barotropic current was increased so that the same barotropic tidal forcing is applied in the shallow water region. This makes the three IT beams more distinguishable. Details are omitted here. To the upper-left of r_b there is a wide beam, and to the lower-left and right of r_b there are two narrow beams. They each propagate onwards until hitting the surface/bottom and as illustrated in Figure 4.8 (d, h) for case B4. The upward phase propagation at $x = 30$ km (Figure 4.8(f)) confirms the downward $\vec{c}_g$ propagation. Due to the different beam patterns in B4, the regions of positive C_p (negative C_n) conversion (Figure 4.8(b)) is different from those in cases B2 and B0. C_p in B4 only exists for $x >$ 30km, which results a smaller total conversion rate C (dashed lines in Figure 4.6 (f, h)).

4.2.3 Scenario III: No blocking + critical point

We now double the current so that $\alpha \geq 1$ for some portion of the slope. We consider cases B1 with V_{max} = 1 m/s and B3 with V_{max} = -1 m/s (black and blue lines in the right column of Figure 4.6). There are 2 critical points in both cases.

In B1, one critical point $x_c = 30$ km lies in the middle of the slope, and the other $x_{c0} = 3$ km is near the bottom. Between these two critical points the slope is supercritical. There are two intense beams emanating from $r_b \approx 35$ km near x_c (Figure 4.9 (g)) but no beams near x_{c0}. This is because the slope is supercritical (subcritical) to the left (right) of x_c. However, the slope is subcritical (supercritical) to the left (right) of x_{c0}. No beams with a positive slope can be emitted from x_{c0}. Note the beam generation location r_b is up-slope of x_c due to the strengthening of the barotropic current in the shallower water. An intense beam is emitted from right of r_b and propagates upwards until it hits the surface at around $x = 53$ km (Figure 4.9(c)). It gets reflected from the surface and keeps propagating onto the shelf while being reflected between the surface and the bottom. Analogously, the

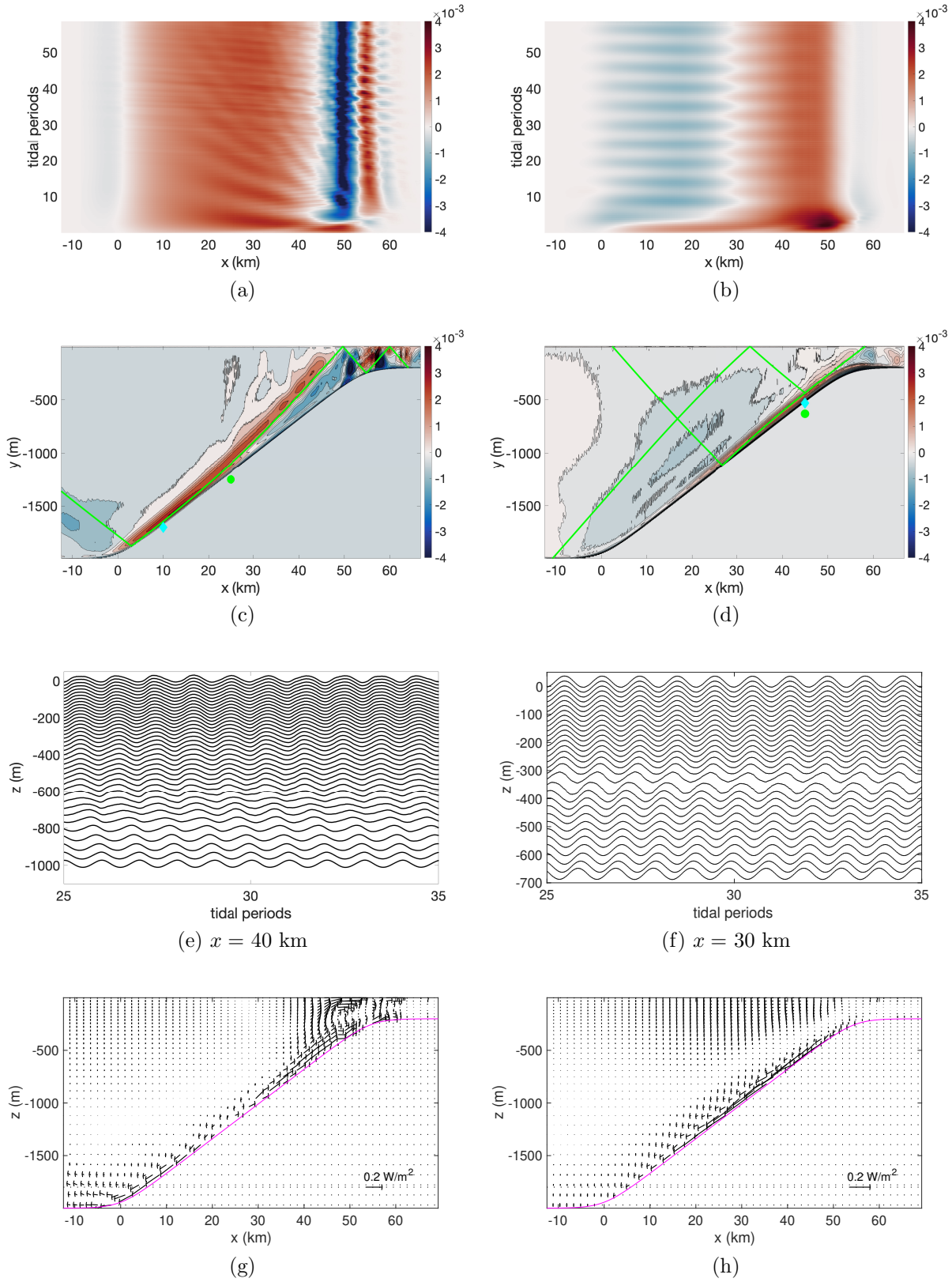

Figure 4.8: Same as Figure 4.7, except for case B2, with V_{max} = 0.5 m/s (left column) and case B4, with V_{max} = -0.5 m/s (right column). The cyan diamond marks r_m where α_{max} occurs. Green circles mark the location where the beam is emitted.

other intense beam emanates from the left of r_b with phase propagating upwards (Figure 4.9(e)) and energy propagating downward (Figure 4.9 g)) until it hits the bottom at around x = -10 km and gets reflected. The reflection location corresponds to the change of sign of $\overline{C}$ (Figure 4.9(a)). The conversion rate $\overline{C}$ vanishes around x = -10 km because the bathymetry is flat and $W = 0$.

In case B3, the two critical points are at $x_c = 53$ km near the shelf break and $x_{c0} = 31$ km in the middle of the slope. The slope is subcritical (supercritical) to the left (right) of x_{c0} while the other way around for x_c. As a result, beams can be generated at $r_b = x_c$ but not at x_{c0}. Three beams are emitted from $r_b = 53$ km (Figure 4.9(d)). One beam emanates from the right of r_b and propagates to the upper right. Two beams emanate from the left of r_b. One of them propagates downwards until it reflects from the bathymetry at $x = 13$ km. The other beam propagates upwards and reflects from the surface at $x = 40$ km, the reflected beam subsequently propagates downward until it hits the bottom at x = -5 km. The upward phase propagation at $x = 30$ km (Figure 4.9(f)) confirms the downward energy propagation. Similar to case B4, a separate simulation with water depth increased by 400m everywhere has been conducted to verify this beam pattern. Details are omitted here. The three beams emitted directly from r_b contribute to the positive conversion C_p, while their reflected beams contribute to the negative conversion C_n. The resulting conversion rate pattern $\overline{C}$ (Figure 4.9(b)) is a combination of C_p and C_n.

Since strong generation occurs near the critical point x_c, B1 and B3 have the largest total conversion rate C in the B series (black and blue in Figure 4.6(f)). On the other hand, due to the different beam patterns, B3 has a much larger region of negative C_n than B1 (Figure 4.9 (a, b)). As a results, B3 has a smaller C than b1 (black and blue lines in Figure 4.6 (f, h)).

4.2.4 Scenario IV: Blocking near the bottom/shelf break

We now consider a strong current such that $f_{eff} > \sigma_T$ along a stretch of the slope which we call a blocking region. Freely propagating internal waves do not exist in this region but tunneling may occur. We analyze results from the A series with a focus on cases A1 (V_{max} = 1 m/s) and A5 (V_{max} = -1 m/s). For this series the slope lies between $x = 0$ and 81 km.

In A1, there is a blocking region, $x \in$ [-5, 26] km, near the bottom of the slope (black line in Figure 4.6(c)). There is a critical point at $x_c = 45$ km. To the left (right) of the critical point, the slope is supercritical (subcritical). Two strong narrow IT beams are emitted from $r_b \approx 55$ km near x_c (Figure 4.10 (c, g)). This pattern is similar to case B1.

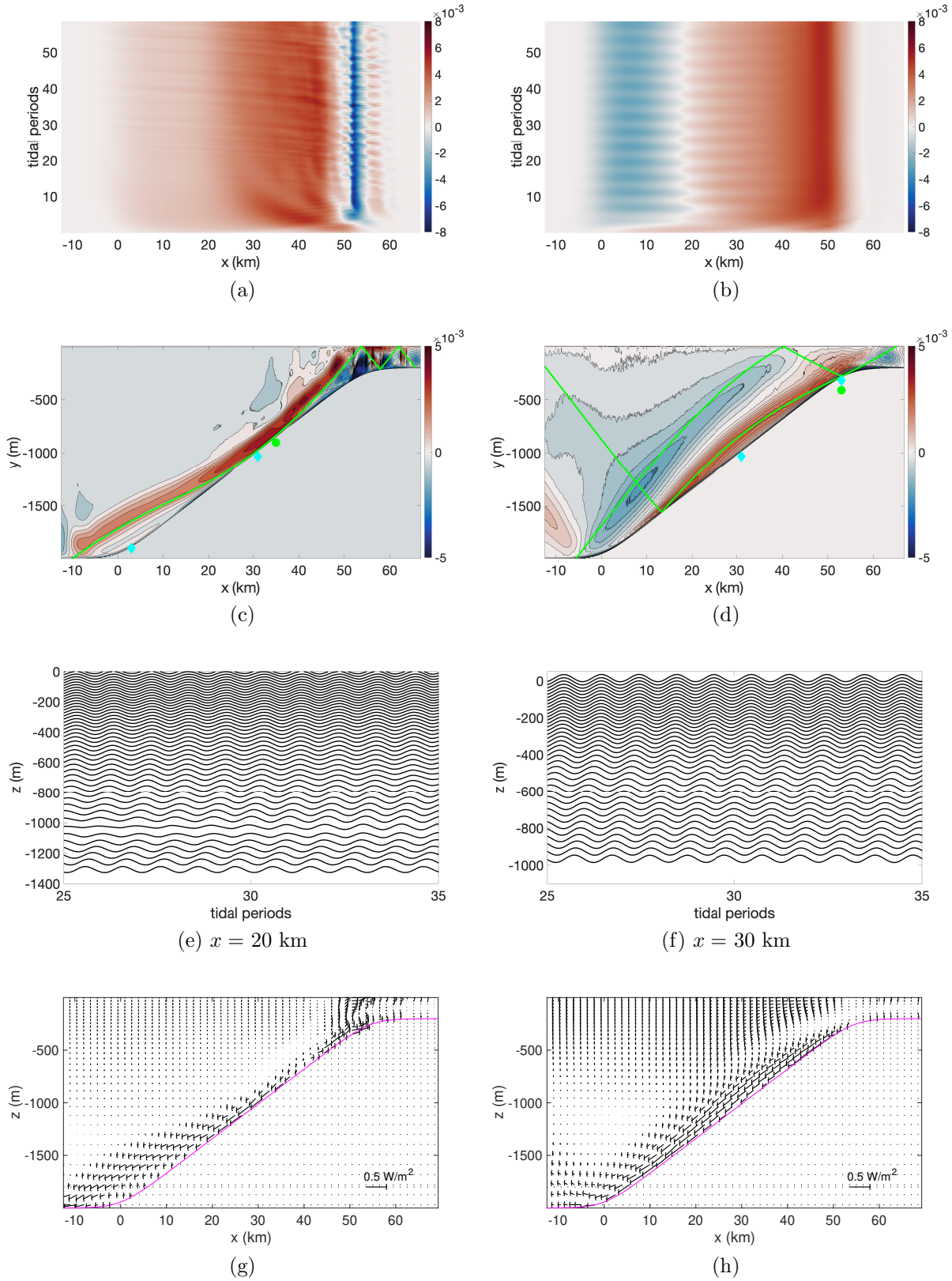

Figure 4.9: Same as Figure 4.7, except for case B1 (left column) and case B3 (right column). The cyan diamonds mark the critical points x_c and x_{c0}. Green circles mark the location where the beam is emitted.

The difference is here the amplitude of the beams with tidal frequency σ_T decays quasi-exponentially to the left in the region -5 km $\leq x \leq$ 26 km, where $f_{eff} > \sigma_T$. IT beams cannot be generated in this blocking region either. As a result, the conversion C in the blocking region is very weak (Figure 4.10(a)). For $x >$ 26 km, the change of sign in C follows the IT beam reflection location.

Relative to A1, the center of the current x_0 in cases A2, A3 and A4 is shifted up or down slope (Figure 4.6(a)). There is a critical point x_c and a blocking region in each of these four cases. In general, the conversion rate C increases as x_c moves closer to the shelf break, since the barotropic tidal forcing reaches its maximum in the shallow water. In this case, we have $C(A3) > C(A1) > C(A2)$ (Figure 4.6(c)). On the other hand, as the blocking region gets closer to the shelf break, C decreases explaining $C(A3) > C(A4)$.

In case A5, the current is negative and the blocking region, $x \in$ [65, 100] km, is near the shelf break (blue line in Figure 4.6(c)). There is a critical point $x_{c0} = 50$ km, but no beams with positive slope can be emitted there because the slope is subcritical (supercritical) to the left (right) of x_{c0}. Since beams with tidal frequency cannot propagate upward due to the blocking region and the slope is supercritical to the right of x_{c0}, two leftward propagating beams are generated approximately 300 m above the slope at $r_b \approx 65$ km, which is near the edge of the blocking region (Figure 4.10 (d, h)). One beam propagates downward and hits the slope at $x = 10$ km. The other beam propagates upwards and gets reflected at the surface $x = 50$ km. The upward phase propagation at $x = 40$ km (Figure 4.10(f)) confirms the downward energy propagation. A separate simulation with water depth increased by 400 m everywhere has been conducted to confirm this beam pattern. Details are omitted here. The reflected (pre-reflected) beam contributes to the negative (positive) conversion C_n (C_p). The resulting conversion pattern is a combination of these two (Figure 4.10 (b)). This puts $C(A5)$ the smallest among the five cases with currents in the A series.

4.3 Frequencies of the generated waves

It is well known that most of the energy in the tide-topography generated waves lies in waves with tidal frequency σ_T (e.g. Bell [1975], Craig [1987], Prinsenberg et al. [1974] etc.). In this section, we focus on the frequency of generated waves in the presence of a current. Since the center of the current lies on the slope, there will always be a region on the slope where $f_{eff} > f$ and another region where $f_{eff} < f$. We restrict our attention on the latter by first investigating the occurence of parametric subharmonic instability (PSI). PSI occurs where waves with approximately half of the primary wave frequency,

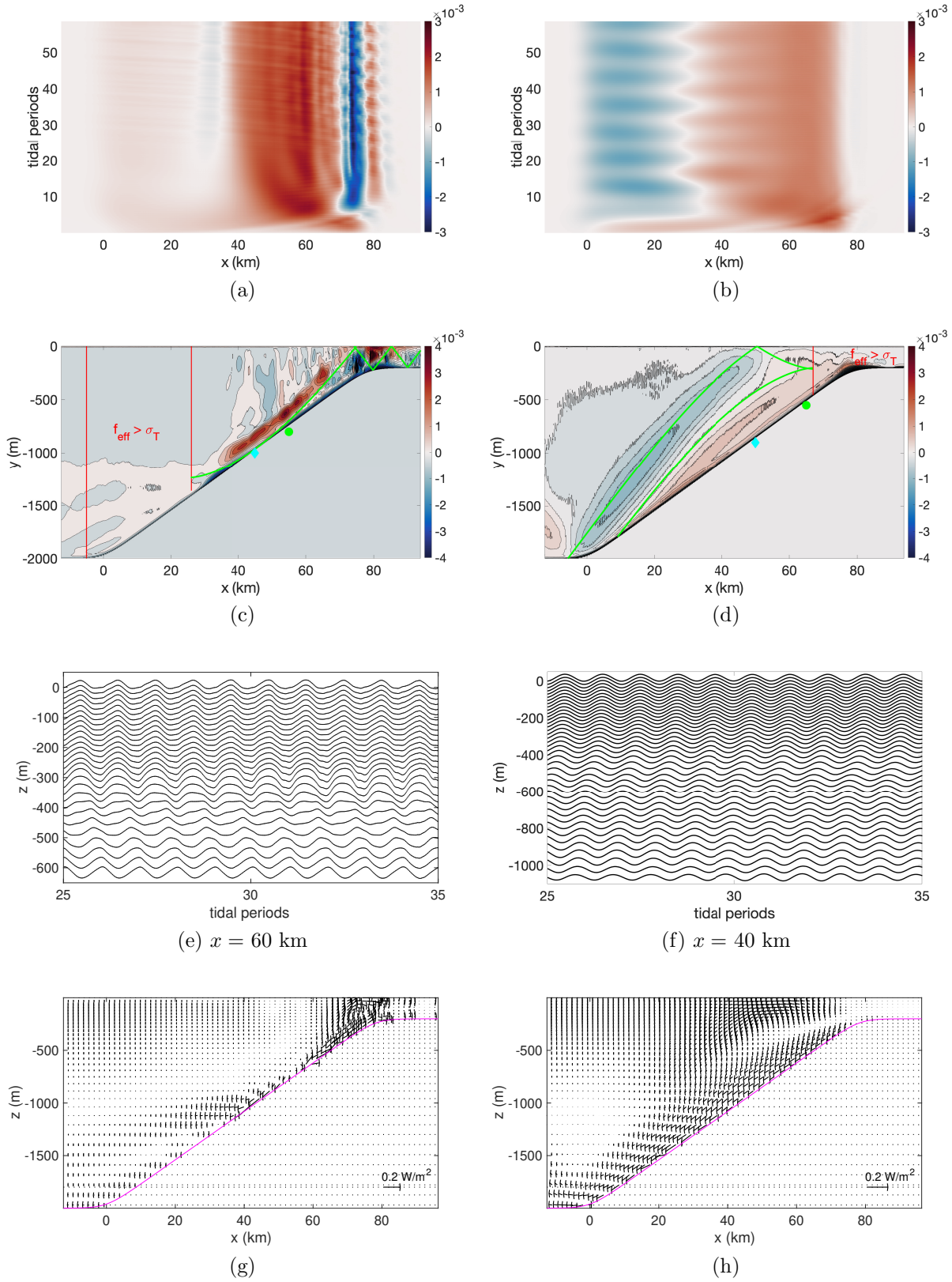

Figure 4.10: Same as Figure 4.7, except for case A1 (left column) and case A5 (right column). The cyan diamonds mark the critical points x_c and x_{c0}. Green circles mark the location where the beam is emitted. The red lines mark the edges of the blocking region.

Table 4.5: Parameters in C series. V_{max}, x_0 and x_r are maximum velocity, the center and the width of the current.

f (s^{-1})	case	V_{max} (m/s)	x_0 (km)	x_r (km)
5.0×10^{-5}	C0	no current		
	C1	2	29	30
	C2	2	29	40
	C3	2	21	40
	C4	-2	29	40
	C5	-2	21	40

in this case $\frac{\sigma_T}{2}$, are generated. It is a particular case of the triad resonant instability (TRI). TRI refers to the destabilization of a primary wave through the interaction among the primary wave and two secondary waves. The frequencies and wave vectors of these three waves satisfy the resonance conditions, $k_0 = k_+ + k_-$ and $\sigma_0 = \sigma_+ + \sigma_-$, where the indices 0 and $\pm$ correspond to the three waves. PSI is the most unstable triad interactions (e.g. Hazewinkel and Winters [2011], Karimi and Akylas [2014], Dauxois et al. [2018] etc.). Following the discussion of PSI, we consider other triad interactions, particularly interharmonics, observed in our simulations. Lastly, strong tidal harmonics are considered.

4.3.1 PSI

Experiments with a lower $f = 5.0 \times 10^{-5} s^{-1}$ (C series), giving $f/\sigma_T = 0.69$, are conducted in order to examine the PSI. Table 4.5 lists the parameters for the C series. These large currents are chosen because we want to have a large area for $f_{eff} < \sigma_T/2$. The details on f_{eff} and γ are plotted in Figure 4.11. All of the cases in the C series have PSI. The current velocity V_{max} in cases C4 and C5 is negative while it is positive for cases C2 and C3. C4 and C5 differ only in the location of the current center x_0. This is the same for C2 and C3. The length of the region where $f_{eff} \leq \sigma_{psi} = \sigma_T/2$ is around 40 km in all cases. In C1, C2 and C3, this is near the shelf break where strong overturning happens at the same time. Figure 4.12 plots the density perturbation ρ' at the end of 60 tidal periods in case C2 and C3. There is a critical point x_c at $x = 20$ and 15 km respectively for C2 and C3, where the IT beams are emitted. As we move closer to the shelf break, the IT beam is unrecognizable. We see strong breaking and some horizontal patches, which lies in the region $f_{eff} \leq \sigma_T/2$ (black lines in Figure 4.11a) and they are probably a result of PSI.

We focus on the simpler cases C4 and C5 to illustrate the PSI effects, where PSI occurs

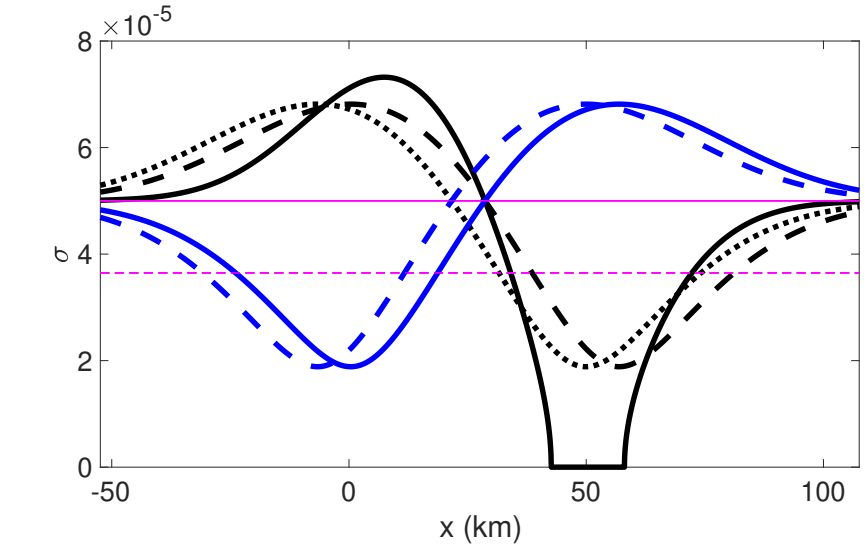

(a)

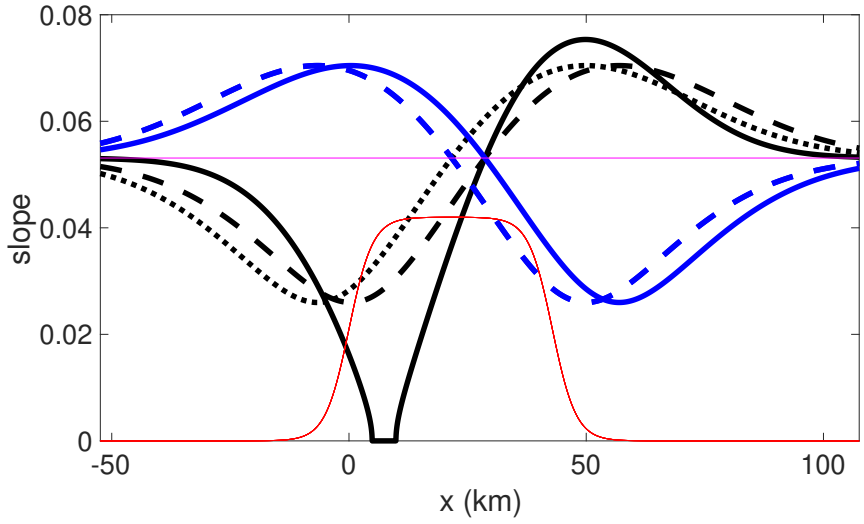

(b)

Figure 4.11: (a): Effective frequencies. Magenta solid (dashed) is f ($\sigma_T/2$). (b): Slope of IT characteristics γ. The red line is the bathymetric slope. (Magenta solid, black solid, black dashed, black dotted, blue solid, blue dashed) = (C0, C1, C2, C3, C4, C5).

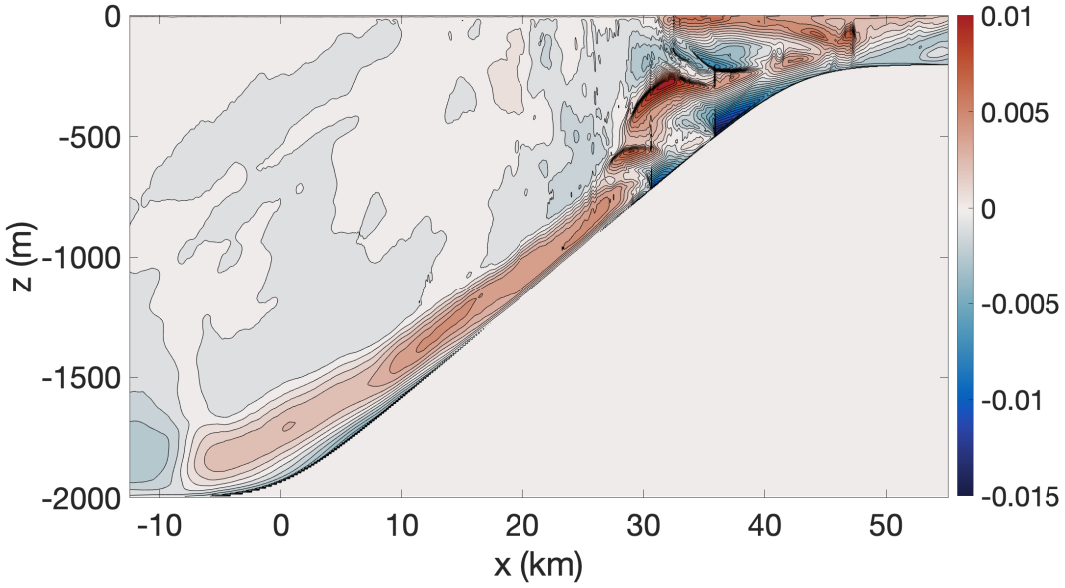

(a)

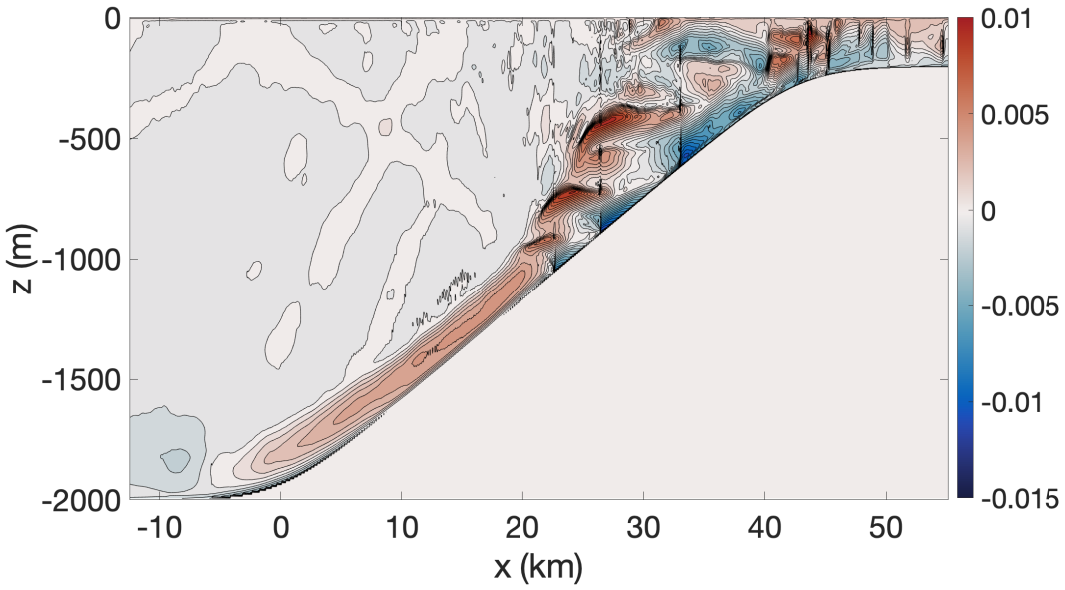

(b)

Figure 4.12: Contours of the density perturbation ρ' at the end of 60 tidal periods. a) case C2. b) case C3.

near the base of the bathymetry and there is no complication of strong breaking. At the end of 60 tidal periods, figures 4.13 and 4.14 plot contours of ρ' and u for cases C4 and C5, respectively. The slope of the IW characteristics $\gamma = \sqrt{\frac{\sigma^2 - f_{eff}^2}{N^2}}$. Waves with lower frequencies have smaller slopes γ. The lower frequency wave signals in C4 is much weaker than that in C5. To see the waves of σ_{psi} more clearly, we multiply the horizontal baroclinic u field by $\cos(\sigma_{psi}t)$ and $\sin(\sigma_{psi}t)$ separately, which gives us a wave field $A(t)$ and $B(t)$. We then take the time-average over the last four of the PSI wave periods, i.e. a time of length $4 \cdot \frac{2\pi}{\sigma_{psi}}$, so we have $< A(t) >$ and $< B(t) >$. The amplitude of the waves with σ_{psi} is calculated as $\sqrt{< A >^2 + < B >^2}$. The result is shown in Figure 4.15. We can start to see the secondary waves with $\sigma = \sigma_{psi}$ in C4, while in C5 these waves are already formed.

Over the slope, $x \in [-5, 50]$ km, γ is generally larger in C4 than in C5 (blue lines in Figure 4.11 b) giving an overall smaller slope criticality $\alpha = s/\gamma$ in C4 than C5, and there are two critical points in C5 but none in C4. These lead to weaker generation and less energy in IT beam in C4. Figure 4.16 plots the conversion rates in C4 and C5. Case C5 has larger C and C_p than C4. This confirms that the bathymetric slope in C5 is closer to be critical and more IT energy is generated compared to that in C4. Waves with σ_{psi} feed on the primary waves, i.e. the IT beam. Since the rate of energy put into the IT beam is smaller in C4 than C5, the PSI in C5 is stronger than that in C4 after running for the same amount of time. If we keep running case C4 for another 60 tidal periods, we can clearly see the PSI signals (Figures 4.17 and 4.18).

PSI mostly occurs when the IT beam reflects from the bathymetry, where the incident and reflected beam intersect and create large disturbances. In case C4, there is no critical point (blue solid line in Figure 4.11 b). The maximum of the slope criticality α_{max} occurs near the top of the slope at $x \approx 37$ km. Figure 4.19 plots the conversion rate $\overline{C}(x,t)$, contours of ρ' and the energy flux for C4 and C5. Three beams emanate from $x \approx 40$ km. One intense beam propagates downward and hits the topography at $x \approx 25$ km. PSI is first generated near this location and the resulting secondary wave propagates to the left. Figure 4.18 plots the amplitude of the horizontal velocity $|u|$ of the PSI. The PSI signals flatten out at $x \approx$ -24 km. This is because $f_{eff} \leq \sigma_{psi}$ when $x \in$ [-24, 18] km (blue solid line in Figure 4.11 a). Not much reflections are observed in Figure 4.18 so we assumed most of the PSI energy was dissipated. Since dissipation is not the focus of this thesis, we will not dive into it any further. From the energy flux plot (Figure 4.19 g), there is weak generation of an IT beam near the base of the bathymetry. This explains the positive generation pattern $x \in$ [0, 12] km in the contour plot of $\bar{C}(x,t)$ (Figure 4.19 a). This beam is not plotted in the density contour plot in Figure 4.19 c.

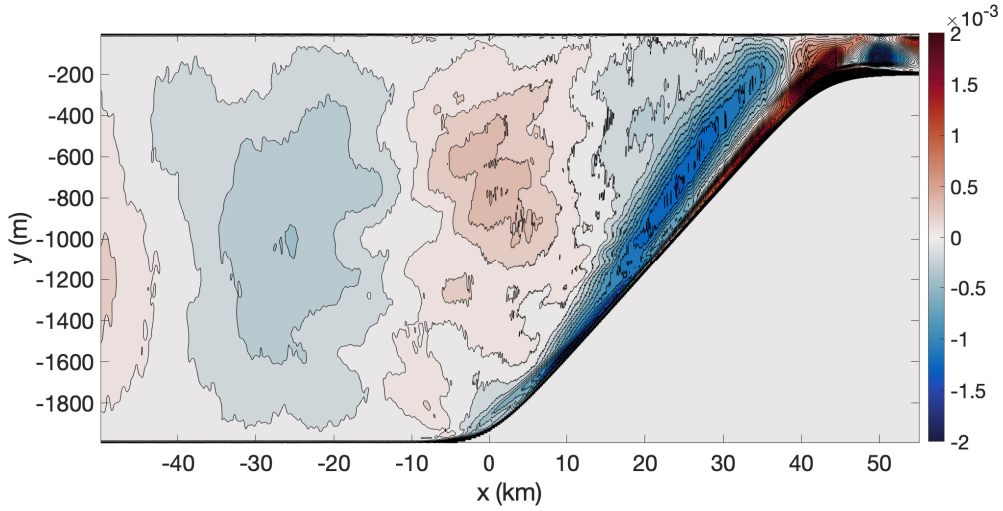

(a)

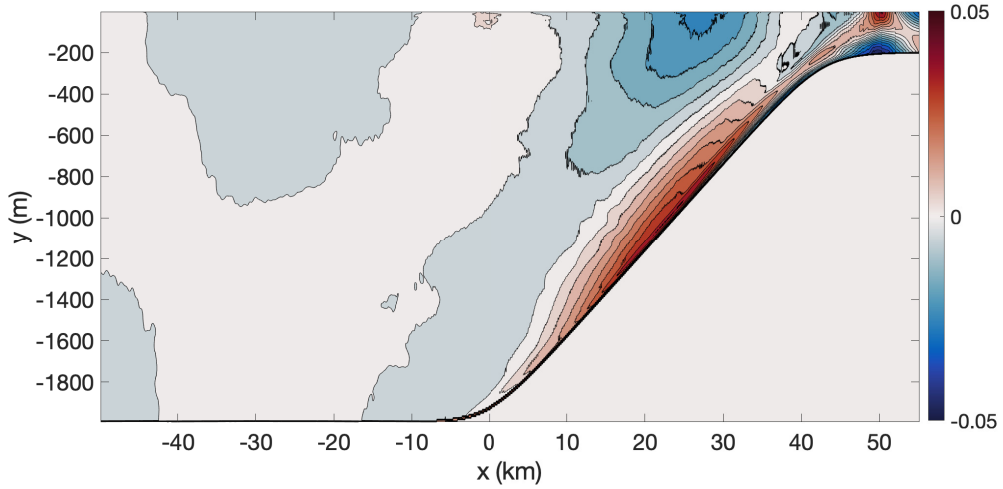

(b)

Figure 4.13: Case C4. Contours of (a) the density perturbation ρ' and (b) baroclinic horizontal velocity u at the end of 60 tidal periods.

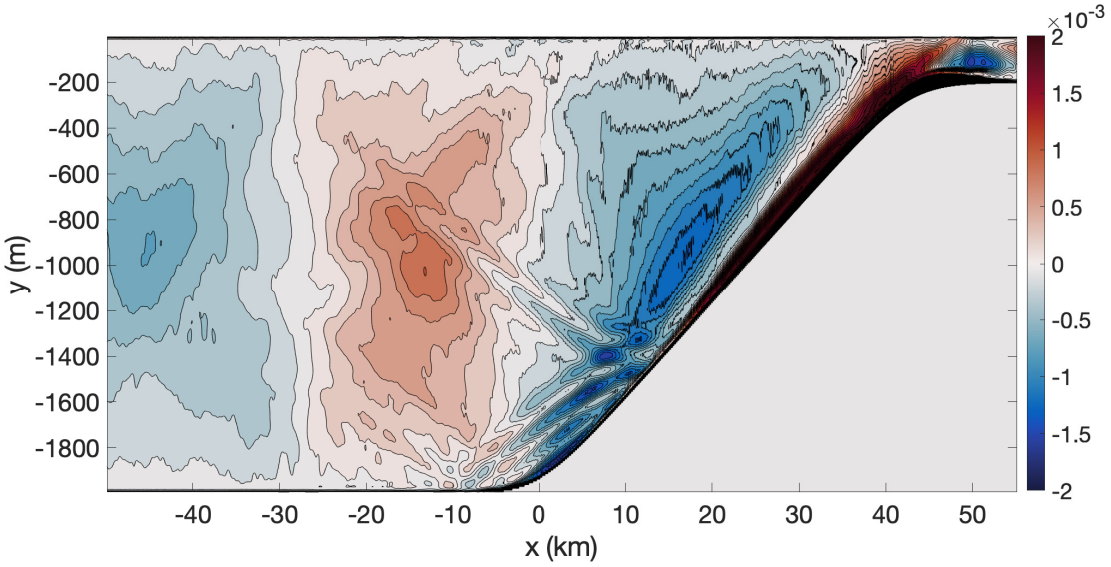

(a)

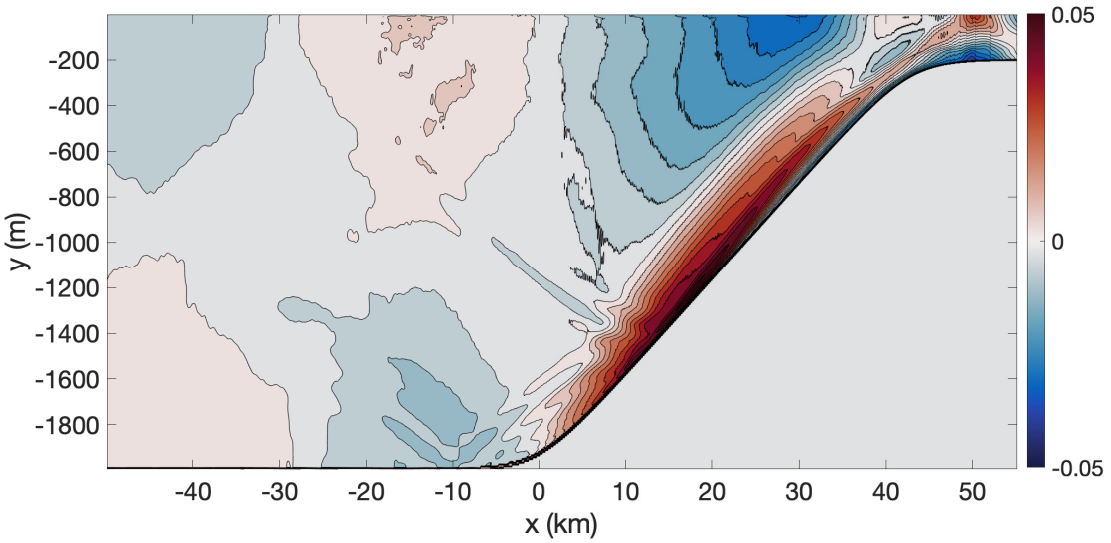

(b)

Figure 4.14: Case C5. Contour of (a) the density perturbation ρ' and (b) baroclinic horizontal velocity u at the end of 60 tidal periods.

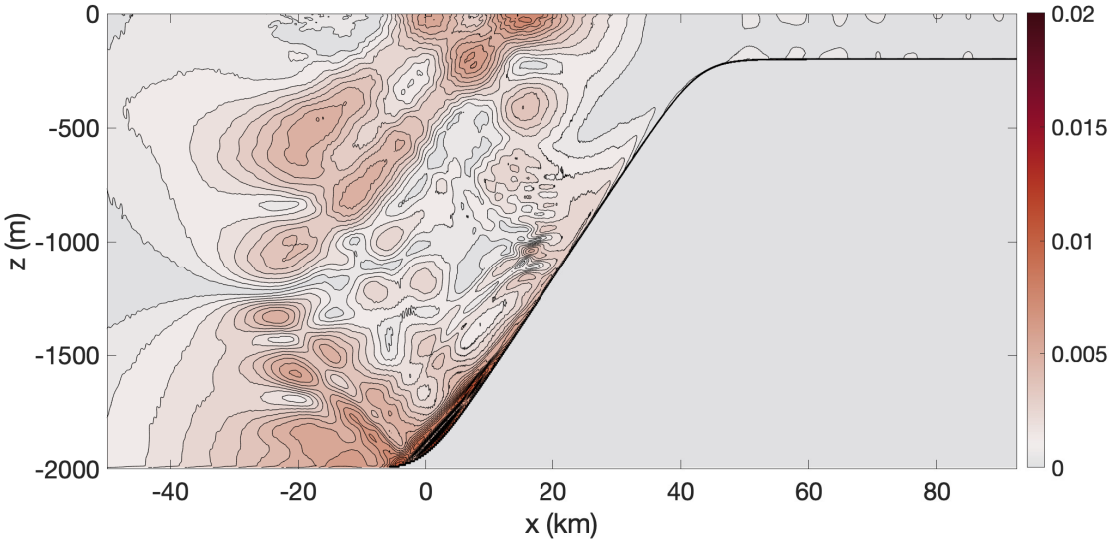

(a)

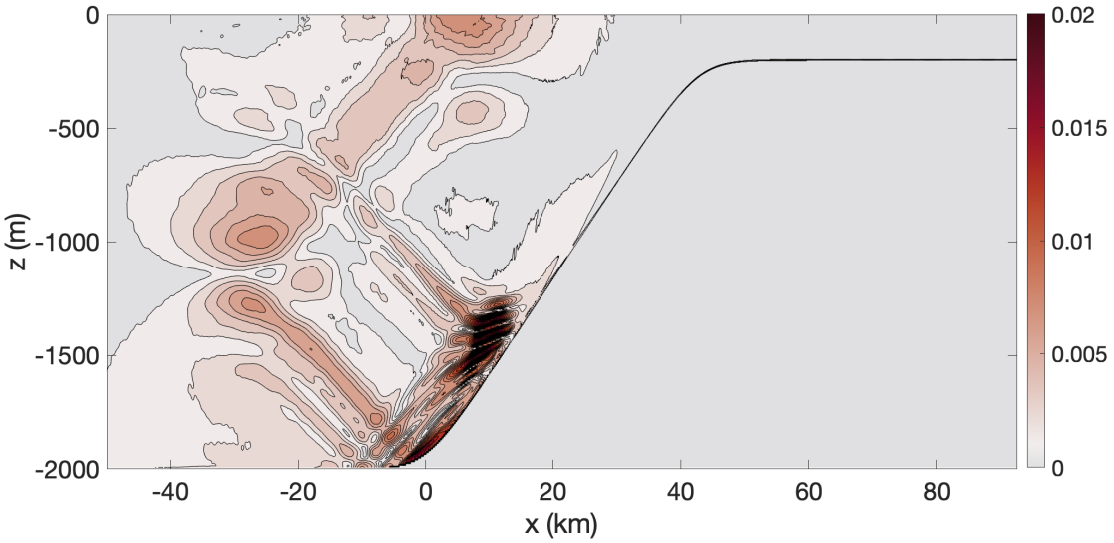

(b)

Figure 4.15: Magnitude $|u|$ for waves of frequency σ_{psi} at the end of 60 tidal periods. a) Case C4. b) Case C5.

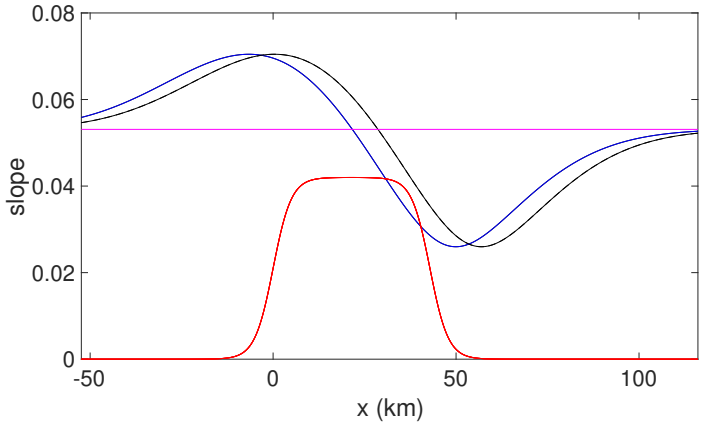

(a)

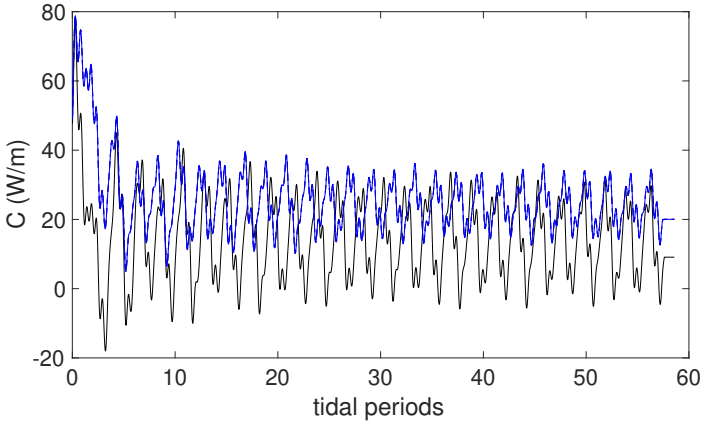

(b)

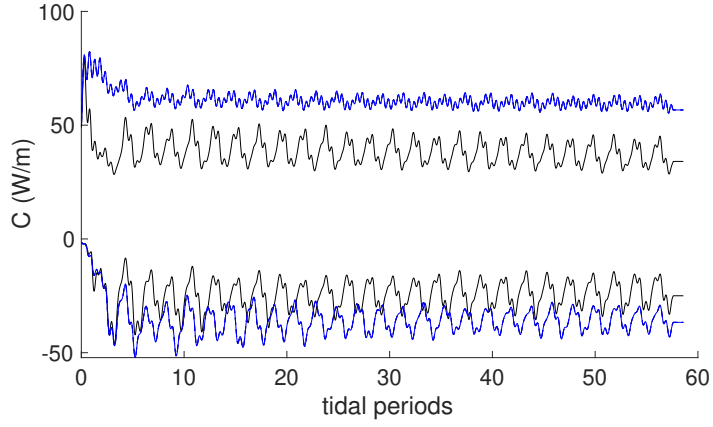

(c)

Figure 4.16: Plot of slope criticality γ (a) and conversion rates (b, c). (b) Total conversion rates C. (c) Conversion rates C_p and C_n. (Magenta, red) = (f, bathymetric slope). C4 (black). C5 (blue).

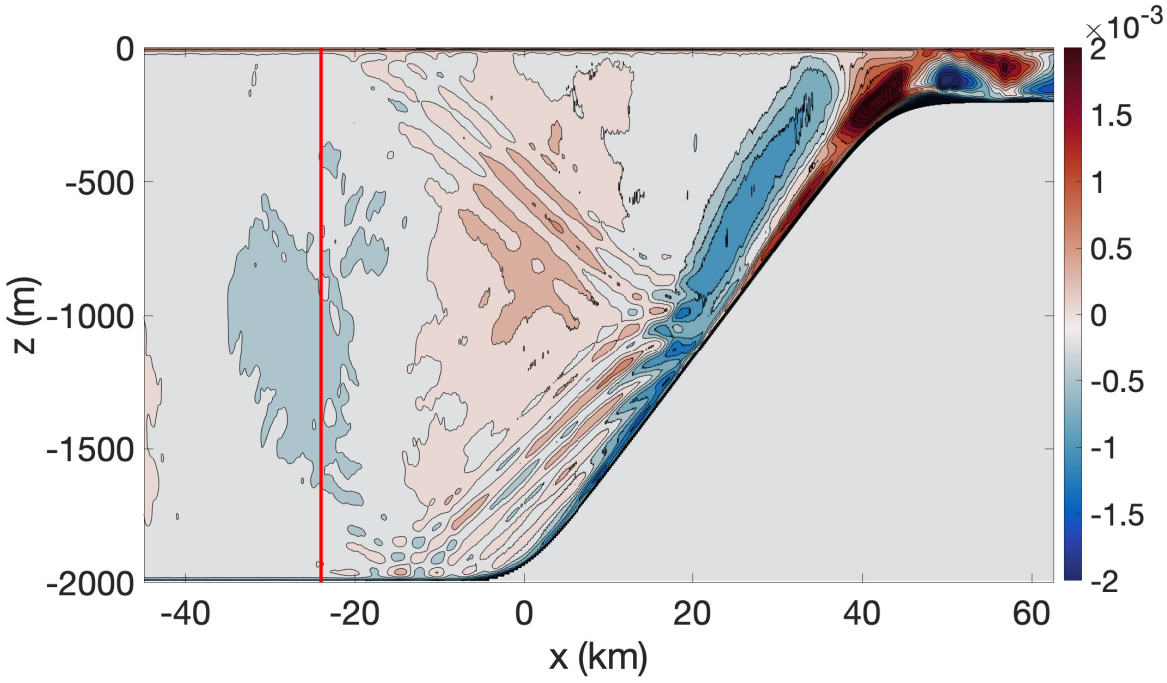

(a)

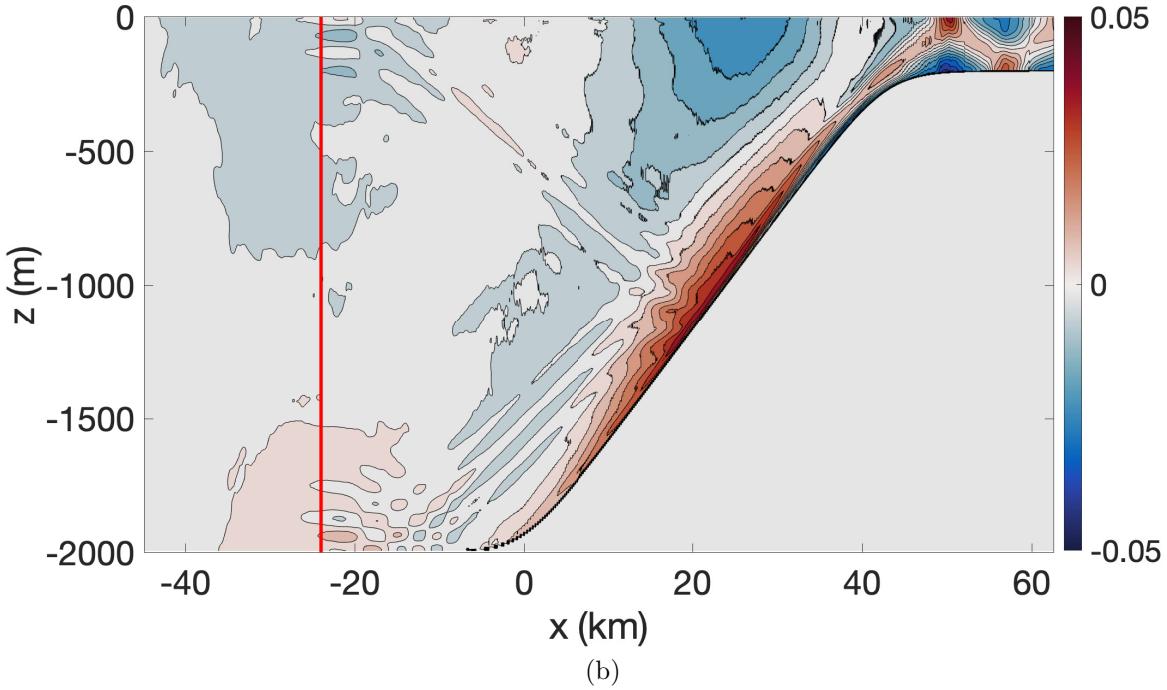

(b)

Figure 4.17: Case C4 at the end of 120 tidal periods. Contours of (a) the density perturbation ρ' and (b) baroclinic horizontal velocity u. Red lines mark the edge where $f_{eff} = \sigma_{psi} = \sigma_T/2$.

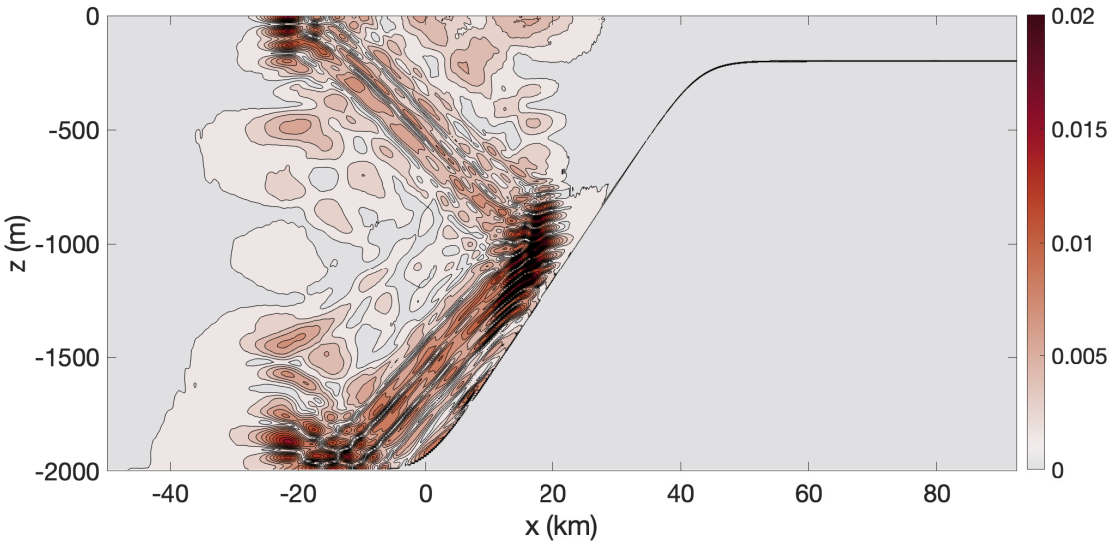

(a)

Figure 4.18: Case C4. Horizontal velocity u for waves of frequency σ_{psi} at the end of 120 tidal periods.

In case C5, there are two critical points x_c = 40 km and x_{c0} = 30 km (blue dashed line in Figure 4.11 b). Three beams emanate from x_c (Figure 4.19 d). One intense beam propagates downwards and hits the bathymetry at $x \approx 20$ km. This is where the secondary waves with $\sigma = \sigma_{psi}$ are generated (Figure 4.15 b). $f_{eff} \leq \sigma_{psi}$ when $x \in$ [-30, 12] km (blue dashed line in Figure 4.11 a). This is probably why the secondary waves stop propagating at $x \approx$ -30 km after being generated at $x \approx 20$ km (Figure 4.15 b). The other two IT beams both propagate upwards and reflect off the surface at x = 32 km and 52 km, respectively. f_{eff} at these two locations are far larger than σ_{psi} so no PSI occurs. There are a number of works on the growth rates and appearance of PSI instability (e.g. Simmons [2008], Koudella and Staquet [2006] etc). Since this is not the focus of our work here, we will not provide any further details.

4.3.2 Interharmonics

Following the previous analysis on PSI, we now focus on the general interharmonics, i.e. waves with σ in between multiples of tidal frequencies σ_T. We extract the horizontal baroclinic velocity $u(x, z, t_n)$ by removing the barotropic component $U(t)$. The analytic

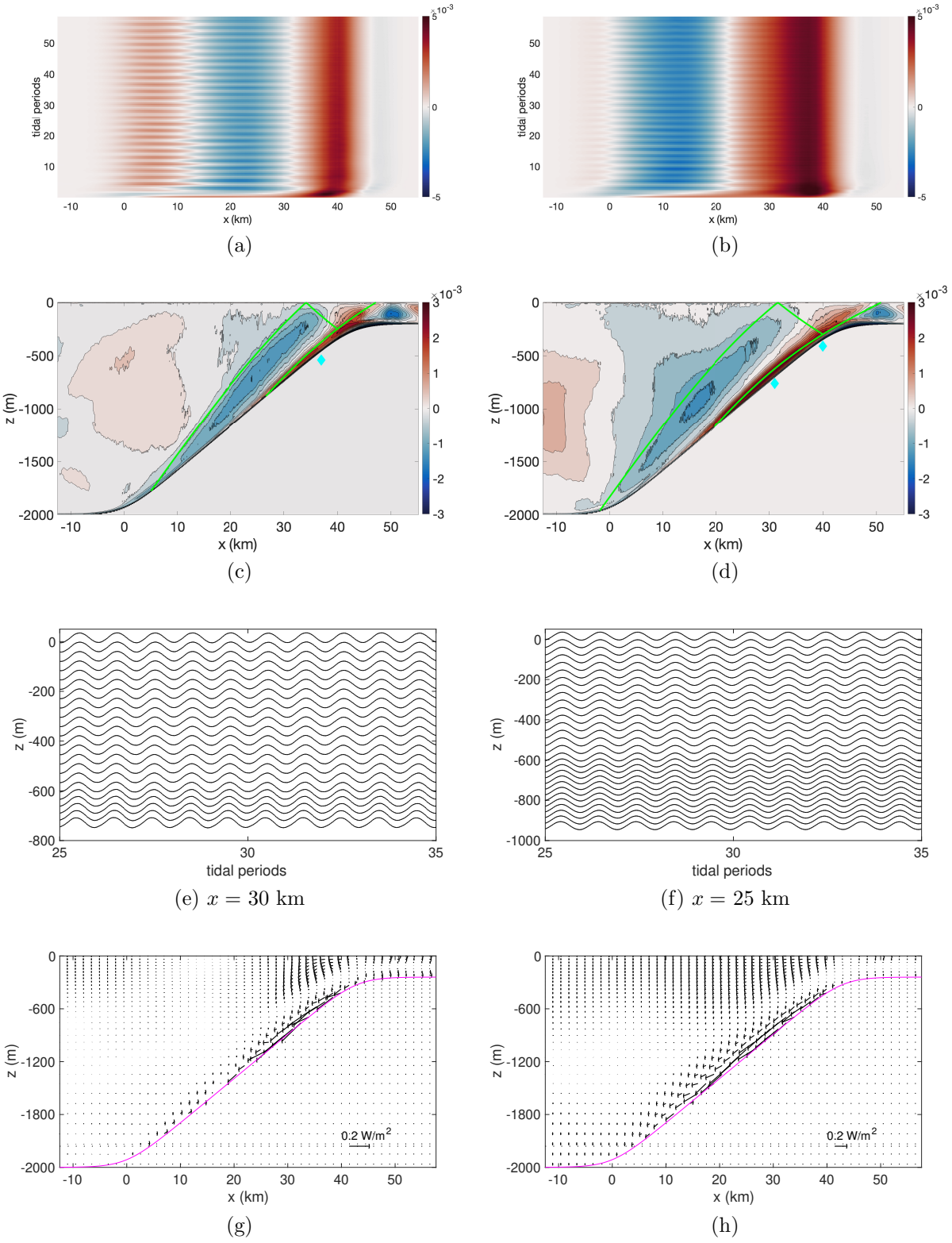

(a) (b) (c) (d) (e) $x = 30$ km (f) $x = 25$ km (g) (h)

Figure 4.19: Same as Figure 4.7, except for case C4 (left) and C5 (right). The cyan diamonds mark r_m where α_{max} occurs (C4) and the critical points (C5).

expression for $U(t)$ is used. We perform the analysis here in constant water depth outside of the slope region so U is independent of x. For each starting location (x_0, z), we take $u_L(x_0, z, t_n) = u(x_L, z, t_n)$ to eliminate the advection effects from the barotropic current, where $x_L = x_0 + \int_{t_0}^{t_n} U(t)\, dt$. $U(t)$ does not depend on x because we only perform this analysis on the shlef where the water depth is constant. Most of the time x_L does not fall right on a grid point. In this case we linearly interpolate the value of u_L by using the velocities at the two closest grid points.

The spectrum $\hat{S}_{ij}(\sigma)$ is computed for each spatial location (x, z). We use the direct spectral estimator described in Percival et al. [1993].

$$\hat{S}(\sigma) = \frac{\Delta t}{\pi} \Big| \sum g_n r_n \exp(-i\sigma t_n) \Big|^2, \quad \sigma \in [0, \sigma_{Nyq}) \tag{4.8}$$

where $\sigma_{Nyq} = \frac{\pi}{\Delta t}$ is the Nyquist frequency. r_n is the sample value. g_n is the data window satisfying

$$\sum g_n^2 = 1. \tag{4.9}$$

We saved the data every 1296s, meaning $\sigma_{Nyq} = 0.00241\,\mathrm{rad\,s^{-1}}$. The time series of $u_L(x, z, t_n)$ for the last 35 tidal periods are windowed using a Hamming window, giving the frequency resolution $= \frac{1}{35}\sigma_T$. MATLAB's fft is used to calculate the discrete Fourier transform. Lastly, we vertically average $\hat{S}_{ij}(\sigma)$ to obtain a vertical average spectrum $\Upsilon_i(\sigma) = \frac{1}{N}\sum_j \hat{S}_{ij}(\sigma)$, where N is the total number of points in the vertical.

All of our cases have similar features. We use case A1 (Table 4.3) as an example for the spectrum (Figure 4.20). The shelf break is at $x \approx 80$ km in case A1 (Figure 4.2 (a)). Since we are not able to show an animation, spectra $\Upsilon_i(\sigma)$ calculated at $x_0 = 88$, 113, 128 km are shown, where the sub-tidal frequency peaks are strong. The tidal advection distance is approximately 2750 m and the shelf break is at $x \approx 80$ km, so the Lagrangian points x_L always stay on the shelf.

- Strong interharmonics with frequencies lower than σ_T and equal to the local f_{eff} are observed (Figure 4.20 b, c, d). We denote any of such frequencies as σ_L and for all our cases $\sigma_L \approx f_{eff}(x)$. The minimum value of the effective frequency $(f_{eff})_{min}$ occurs at $x = 94$ km. Between the shelf break $x = 80$ km and $x = 94$ km, f_{eff} varies slowly and stays in the vinicity of $(f_{eff})_{min}$. As x increases from $x = 94$ km, f_{eff} increases monotonically from $(f_{eff})_{min}$ to f. Since freely propagating waves must have $\sigma > f_{eff}$, waves with frequency $f_{eff}(x')$ generated from anywhere in $x < x'$

cannot propagate to the right of $x = x'$. Such waves accumulate at $x = x'$. As a result, we see this strong peak of the spectrum at the local effective frequency. No PSI is detected because $(f_{eff})_{min} \gg \frac{\sigma_T}{2}$.

- At $x = 88$ km (Figure 4.20 b) the closest of our three locations to the shelf break, σ_L is slightly smaller than the local effective frequency f_{eff}. There are at least two possible reasons. The first one is related to the overturning that occurs near the shelf break. See a plot of the density perturbation and the total density at the end of 60 tidal periods in Figure 4.21. In addition, on the other side of the current in the region $x \in [0,\ 20]$ km, $f_{eff} > \sigma_T$. Leftward propagating ITs generated at the shelf break will be reflected back and enhance the breaking. The second reason is the spectra resolution. Figure 4.22 plots the frequency resolution. There are 35 points in one tidal frequency. σ_L here is approximately the minimum of f_{eff}, where there is no point representing σ_L so the peak of the spectrum is shifted to one of the two adjacent points.

- There are signals of subinertial disturbances which are trapped non-propagating oscillations with frequencies below the effective frequency. Literature on this area is scarce. Young et al. [2008] first provided the theoretical framework on the occurrence of subinertial unstable disturbances by predicting that PSI extends the IW band to slightly subinertial frequencies. Korobov and Lamb [2008] noticed a weak forced wave signal in their two dimensional numerical simulations of tide-topography interaction. Zhang and Duda [2013] found a forced wave signal at half of the semi-diurnal tide in their three dimensional numerical simulations confirming Young et al.'s theory.

  To better examine the forced waves signal, a log scale of the spectrum $\Upsilon(\sigma)$ at $x = 88$ km for $\sigma \in [0, 2\sigma_T]$ is plotted (Figure 4.23 a). With the strong waves at σ_T and σ_L, the peak at $\sigma_{11} = \sigma_T - \sigma_L$ is a forced wave. Note at this location, $\sigma_L \approx (f_{eff})_{min}$. σ_{12} can be formed from two interactions $\sigma_{12} = \sigma_T + \sigma_L$ or $\sigma_{12} = 2\sigma_T - \sigma_{11}$, where the former is a result of TRI and the latter involves the forced wave with σ_{11}. Similarly, the peak at σ_2 can also be written as $\sigma_2 = \sigma_T + \sigma_{11}$ or $\sigma_2 = 2\sigma_T - \sigma_L$, where the former involves the forced wave σ_{11} and the latter is from TRI. Following this pattern, the peak at $\sigma_3 = \sigma_2 - \sigma_L = 2\sigma_T - 2\sigma_L = 2\sigma_{11}$. $\sigma_4 = \sigma_3 + \sigma_T = 3\sigma_T - 2\sigma_L$. $\sigma_5 = \sigma_4 - \sigma_L = 3\sigma_T - 3\sigma_L = 3\sigma_{11}$. $\sigma_6 = \sigma_5 + \sigma_T = 4\sigma_T - 3\sigma_L$. Peaks at σ_3 and σ_5 are forced waves. Any of these interharmonic signals can be a result of more than one triad interaction. For example, the peak at σ_3 can be involved in three interactions: σ_2 and σ_L, $2\sigma_T$ and $2\sigma_L$ or σ_{11} and itself. Some of the interactions include higher tidal harmonics. This may be valid because waves at higher harmonics are generated at this location (Figure 4.23 b).

Now we look at a similar plot for the spectrum at $x = 113$ km (Figure 4.24). Since both the signals at σ_L and σ_T are weaker here than at $x = 88$ km (Figure 4.20 b, c), the nonlinear interactions and the secondary waves are weaker. No distinct higher harmonics can be seen (Figure 4.24 b). As a result, we can only recognize five instead of seven signals in addition to the major tidal component σ_T and $\sigma_L = f_{eff}(x = 113\ km)$. Analogous to the scenario at $x = 88$ km, we have $\sigma_1 = \sigma_L - \sigma_T$, $\sigma_2 = \sigma_T + \sigma_1$, $\sigma_3 = \sigma_2 - \sigma_L$, $\sigma_4 = \sigma_3 + \sigma_T$ and $\sigma_5 = \sigma_4 - \sigma_L$. Since the higher harmonics are weak here, we do not include them in the triad interaction like we did with $x = 88$ km.

Figure 4.25 shows the log scale plot of the spectrum Υ at $x = 128$ km. The signals at σ_L and σ_T are the weakest among the three locations (Figure 4.20 b, c, d). Following our previous analysis, the nonlinear interactions here are the weakest. Except for the major signals at σ_L and σ_T, only three signals stand out. Similar to the two locations above, we have $\sigma_1 = \sigma_L - \sigma_T$. However, the peaks at σ_2 and σ_3 are different. Though they still satisfy $\sigma_3 + \sigma_L = \sigma_2$, σ_2 is no longer $\sigma_T + \sigma_1 = 2\sigma_T - \sigma_L$ but the closest we can find is $\sigma_2 = 2\sigma_T - 2(f_{eff})_{min} + \sigma_L$. At $x = 128$ km, $\sigma_L > (f_{eff})_{min}$. However, at $x = 88$ and 113 km, $\sigma_L \approx (f_{eff})_{min}$, so the formulation here will be valid too. On the other hand, the spectrum resolution in our analysis $1/35\sigma_T$ may be too coarse to recognize these fine details. At this stage, it is unclear to us what triad interactions are mostly responsible for each of the interharmonics, how strong the forced waves can be and what the generation mechanisms are.

4.3.3 Tidal harmonics

We take case C1 as an example because of its prominent generation of tidal harmonics. The density perturbation ρ' and u at the end of 60 tidal periods are plotted in figure 4.26. There are two critical points $x_c = 24$ km and $x_{c0} = 0$ (black solid line in Figure 4.11 b). No beams are generated near x_{c0} because the slope is subcritical (supercritical) to the left (right) of x_{c0}. Two beams emanate from x_c. One of them is emitted from the right of x_c propagating upwards and reflects from the surface $x = 41$ km (the reflected beam is not plotted). To the left of x_c is another beam propagating to the bottom left until it reaches $x = 10$ km. $f_{eff} \geq \sigma_T$ when $5 \leq x \leq 10$ km. Part of the energy tunnels through this blocking region with most of the energy reflecting from $x = 10$ km. At $x = 10$ km, the incident and the reflected IT beam creates a large disturbance resulting in a beam of $2\sigma_T$ (green dashed line in Figure 4.26). This beam propagates to the upper right until hitting the surface at $x = 20$ km. We extract the magnitude $|u|$ of the beams with the second

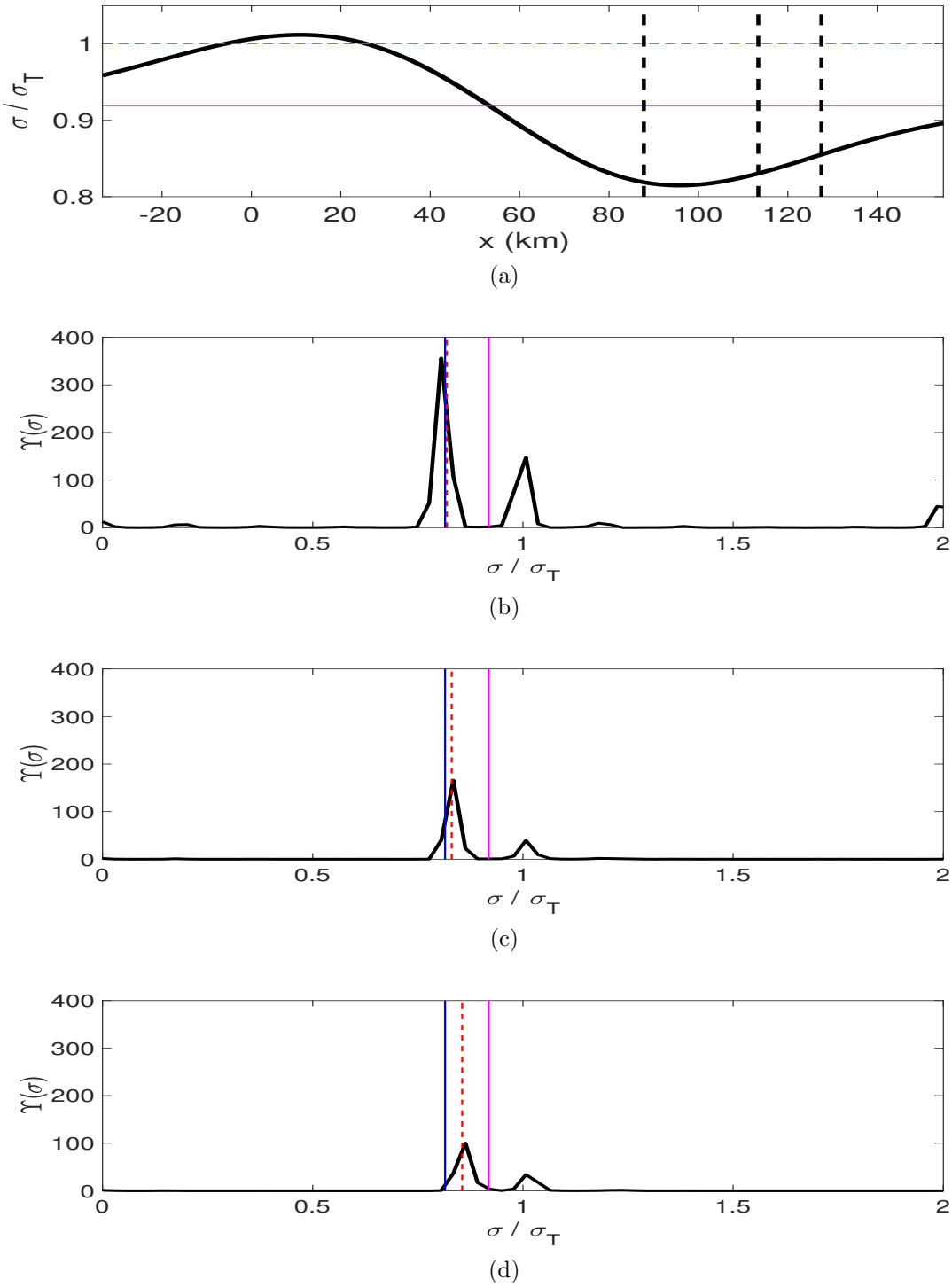

Figure 4.20: Case A1. a) Frequencies (solid black) scaled by the tidal frequency σ_T. Black dashed lines mark the location where $\Upsilon(\sigma)$ is calculated. (σ_T, f) = (magenta dashed, magenta solid). b, c, d) $\Upsilon(\sigma)$ (solid black) at x = (88, 113, 128) km. (min f_{eff}, local f_{eff}, f) = (blue, red dashed, magenta solid).

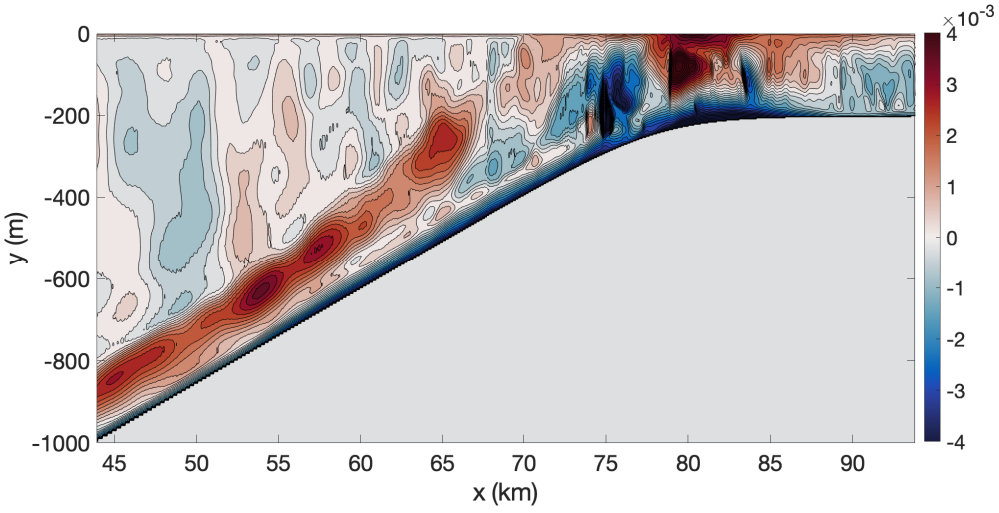

(a)

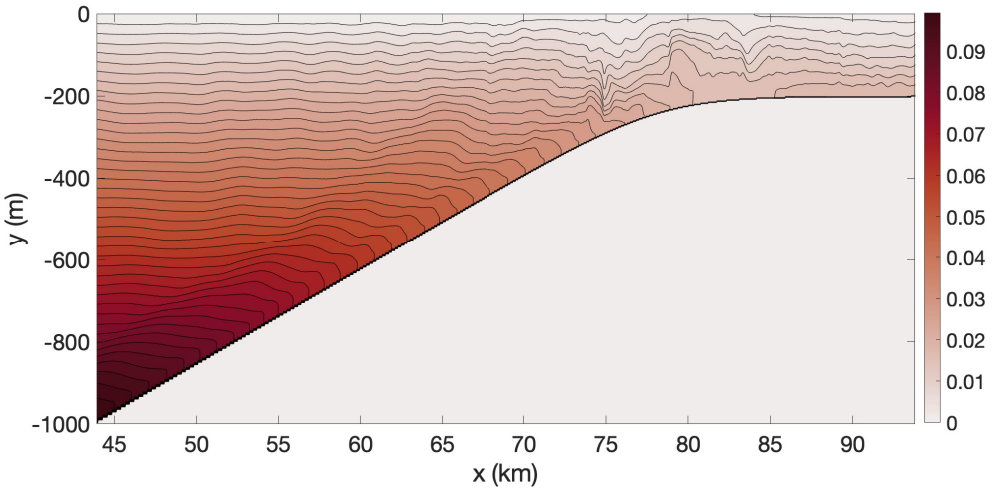

(b)

Figure 4.21: Case A1 at the end of 60 tidal periods. a) Density perturbation. b) Total density field.

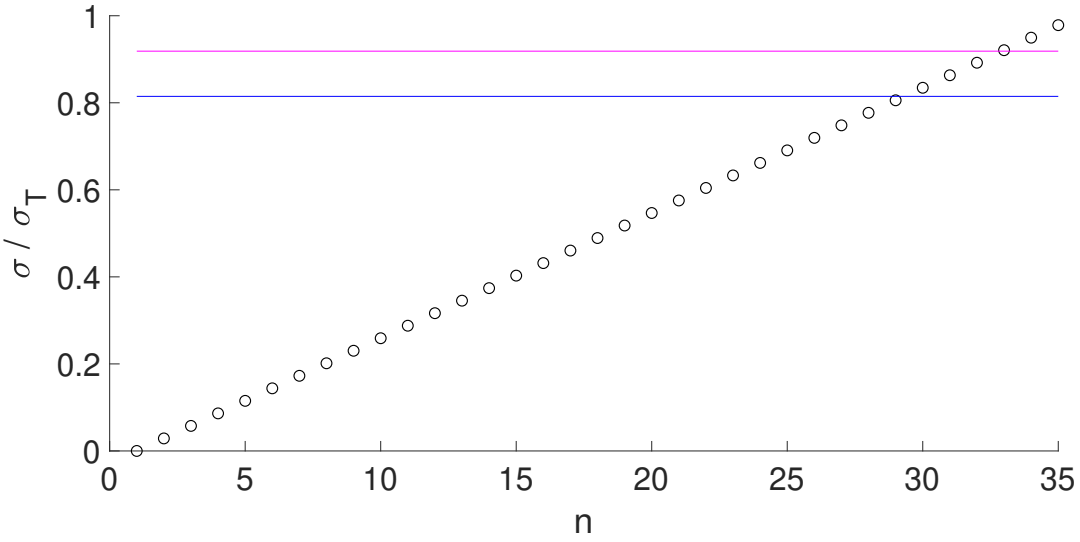

(a)

Figure 4.22: Plot of spectrum resolution. n is the number of points. (min f_{eff}, f) = (blue, magenta).

harmonics $\sigma_{2T} = \sigma_T$ over a period of $4 \cdot \dfrac{2\pi}{2\sigma_T}$ (Figure 4.27 a). The procedure is the same as that in section 4.3.1. A zoomed out plot with a wider range of x (Figure 4.27 b) confirms the prominent generation of the second harmonics is to the right of the blocking region and most of the energy dissipates over the slope as little propagates over onto the shelf. Figure 4.28 plots the spectrum $\Upsilon(\sigma)$ of the horizontal baroclinic velocity u on the shelf. We can see there is no strong signal of higher harmonics.

On the other hand, $f_{eff} < \sigma_T/2$ when $x \in [32, 74]$ km. We can see this strong PSI signal on the shelf (red lines in Figure 4.28). In the contours of ρ' (Figure 4.26 a), there are patches of waves with almost horizontal slopes at $x \in [25, 35]$ km near the bathymetry. As it moves towards the shelf break $x \approx 43$ km, the nonlinear interaction is too strong to spot clear patterns. The strongest spectrum at these two locations, $x = 45$ and 51 km, are signals with frequency close to be 0. These are not subinertial waves. $f_{eff}^2 \leq 0$ when $x \in [43, 57]$ km (black solid line in Figure 4.11 a), indicating in this region there is no lower bound on the frequencies of the freely propagating waves. More research needs to be done over the slope to understand the physical mechanisms behind the interharmonics and higher harmonics and their eventual fate.

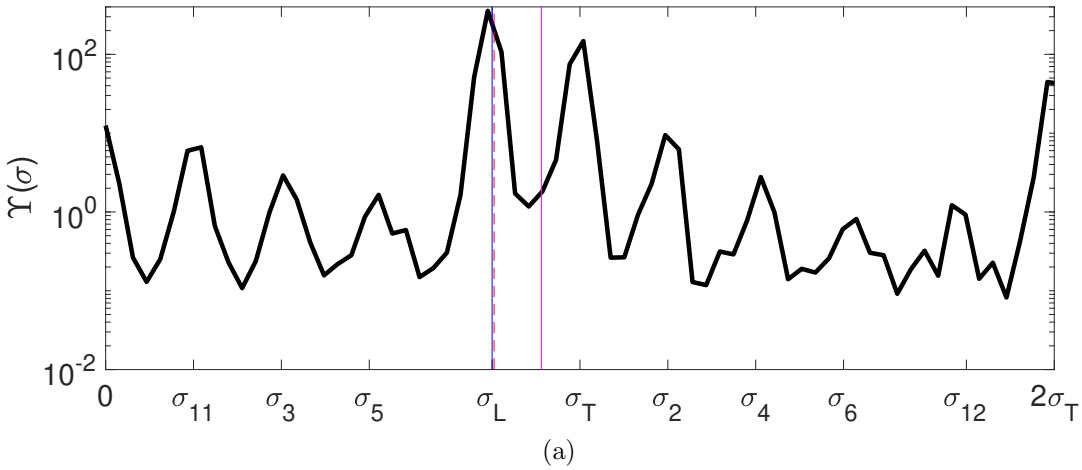

(a)

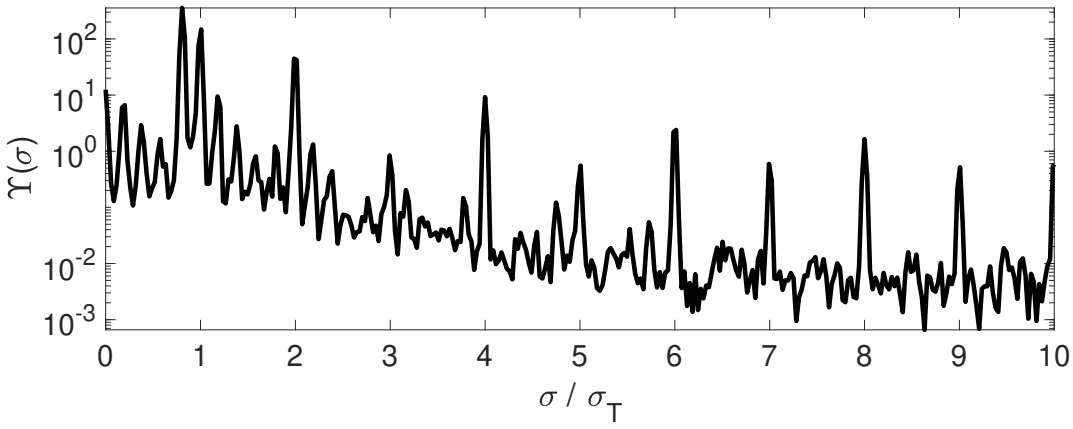

(b)

Figure 4.23: Same as Figure 4.20 b) except plotting the y-coordinate using a logarithmic scale. (min f_{eff}, local f_{eff}, f) = (blue, red dashed, magenta solid). See text for an explanation for interharmonics σ_n.

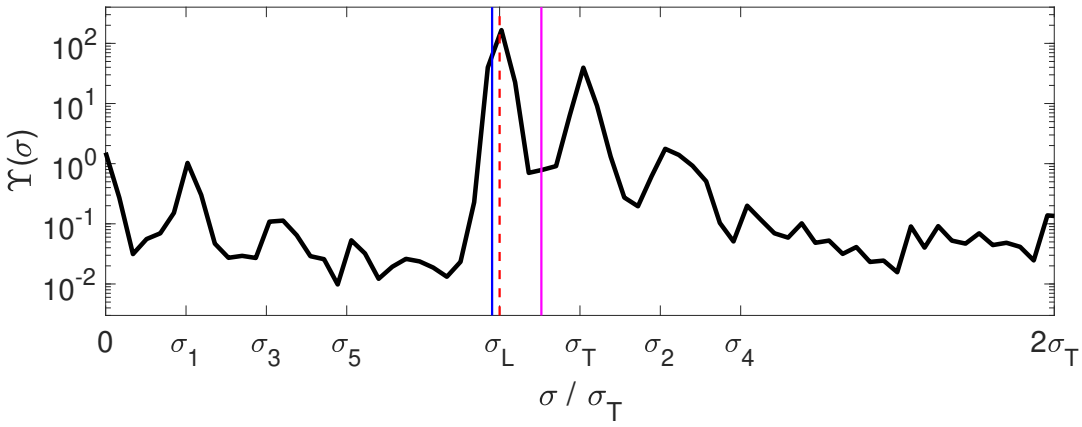

(a)

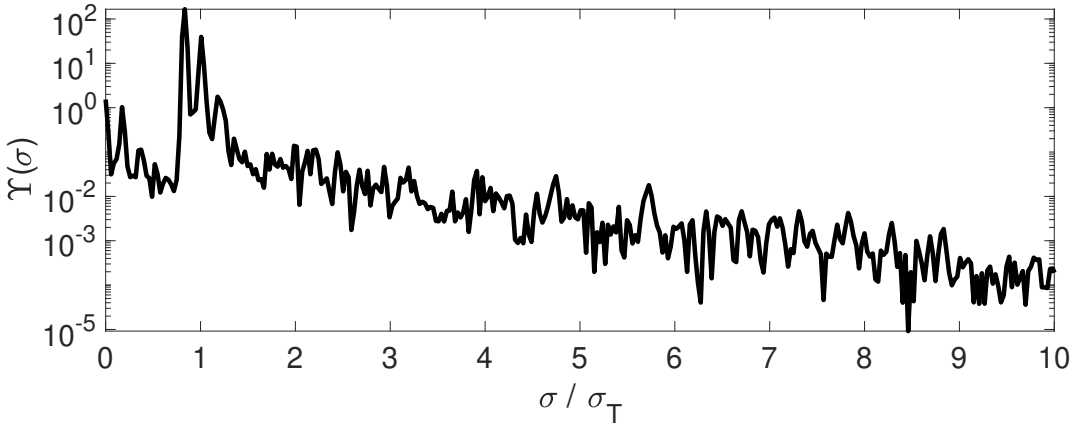

(b)

Figure 4.24: Same as Figure 4.23 except $x = 113$ km. (min f_{eff}, local f_{eff}, f) = (blue, red dashed, magenta solid). See text for an explanation for interharmonics σ_n.

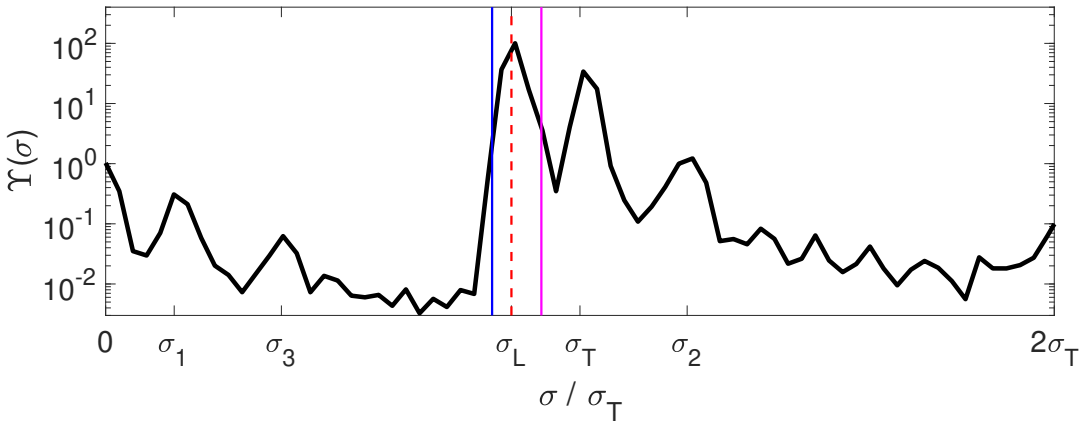

(a)

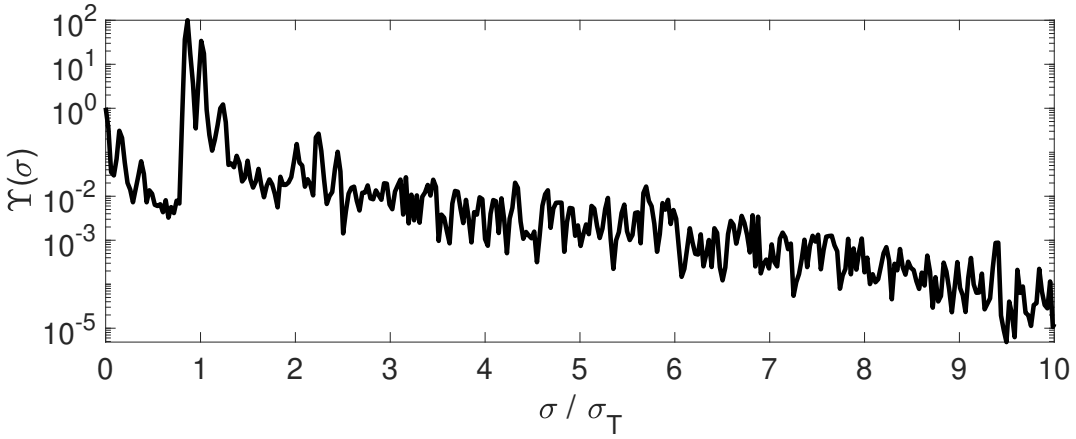

(b)

Figure 4.25: Same as Figure 4.23 except $x = 128$ km. (min f_{eff}, local f_{eff}, f) = (blue, red dashed, magenta solid). See text for an explanation for interharmonics σ_n.

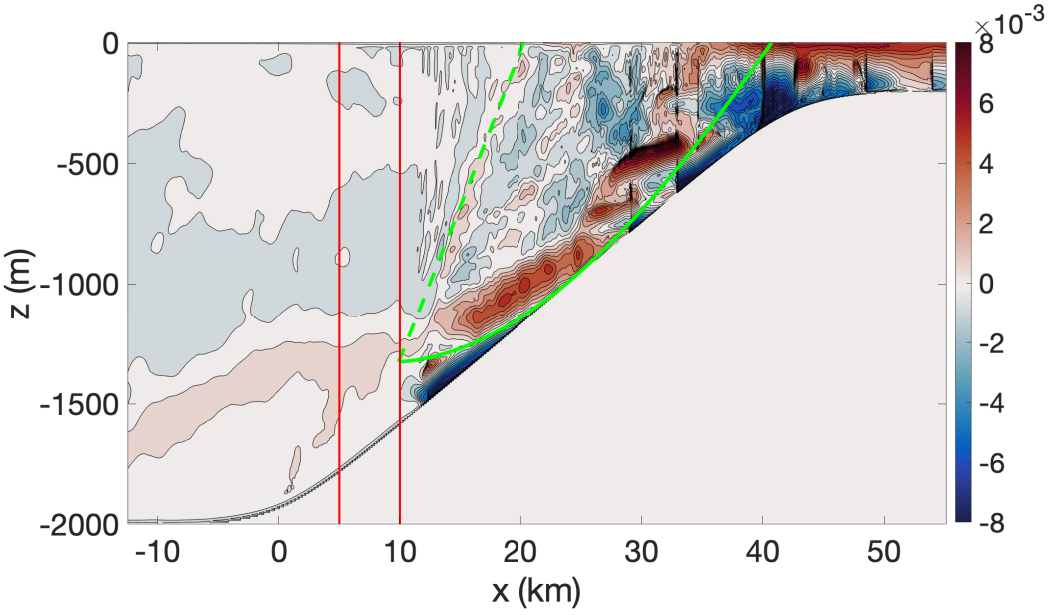

(a)

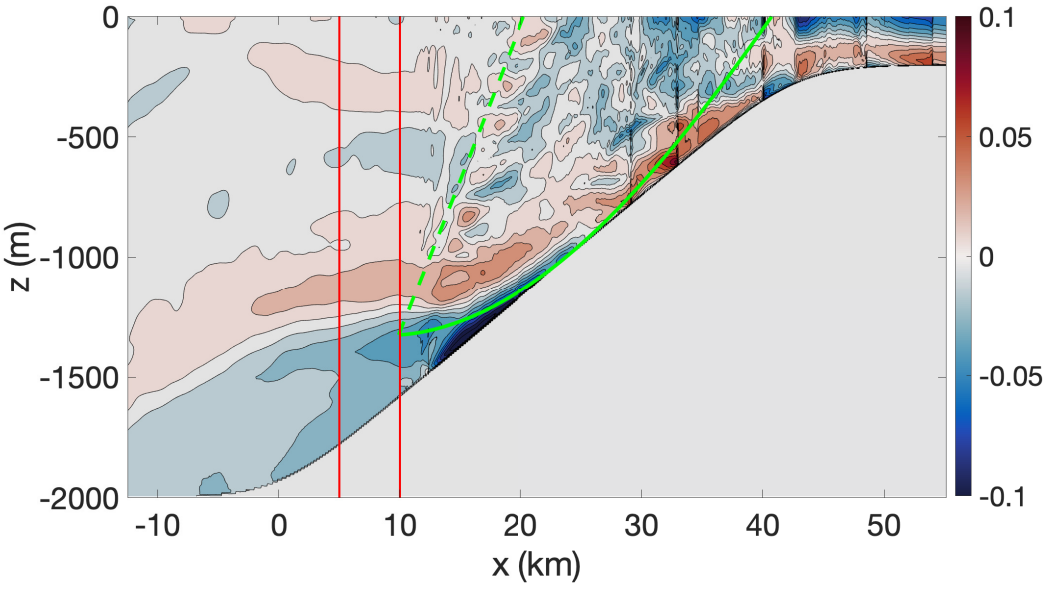

(b)

Figure 4.26: Case C1. Contours of (a) the density perturbation ρ' and (b) baroclinic horizontal velocity u at the end of 60 tidal periods. Wave characteristics of the tidal frequency σ_T (green solid) and twice the tidal frequency $2\sigma_T$ (green dashed) are overlaid. Red lines mark the edges of the blocking region for the IT beam.

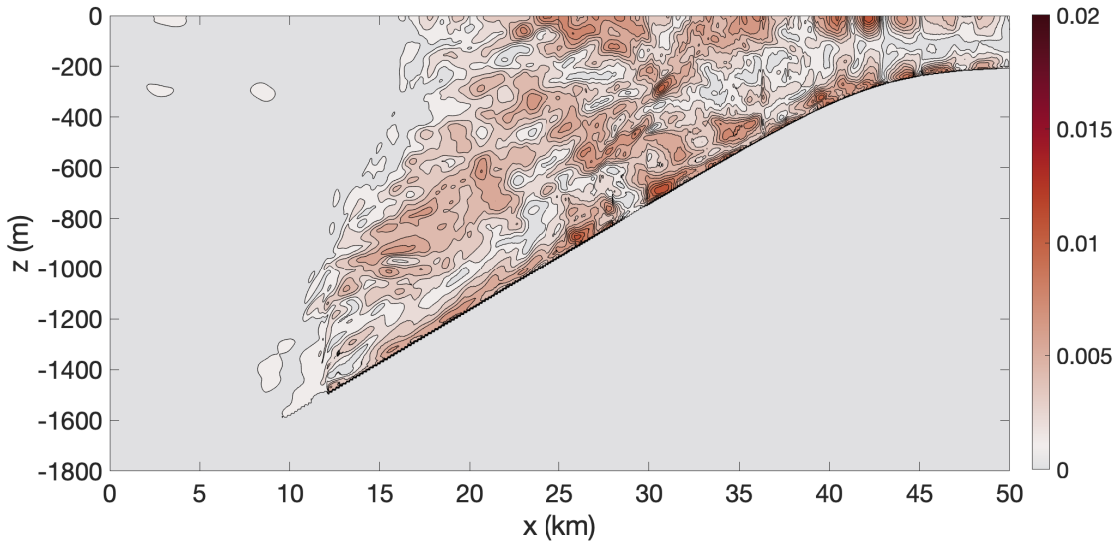

(a)

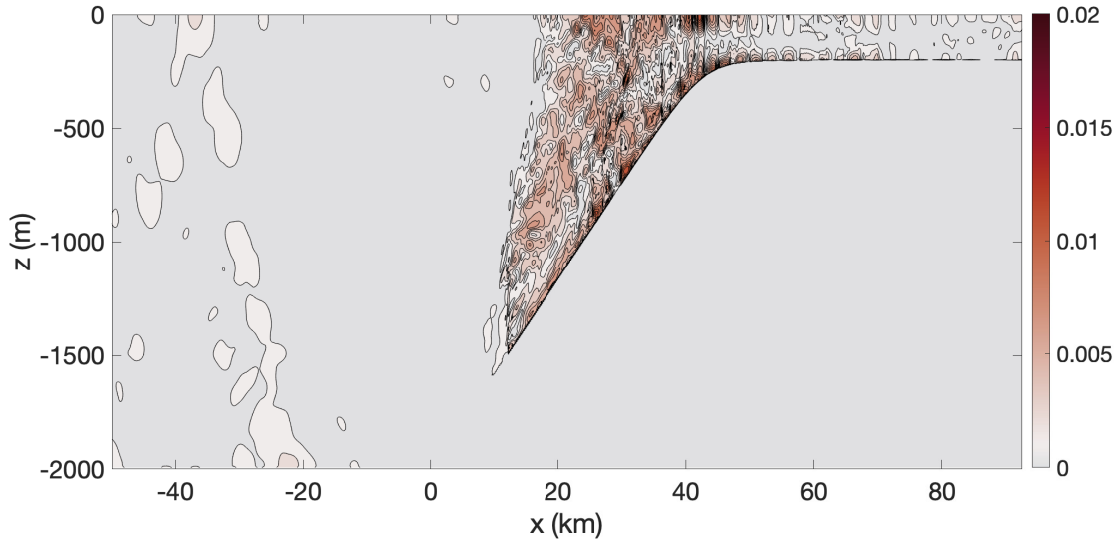

(b)

Figure 4.27: Case C1. The horizontal velocity amplitude $|u|$ for waves of twice the tidal frequency $2\sigma_T$ at the end of 60 tidal periods.

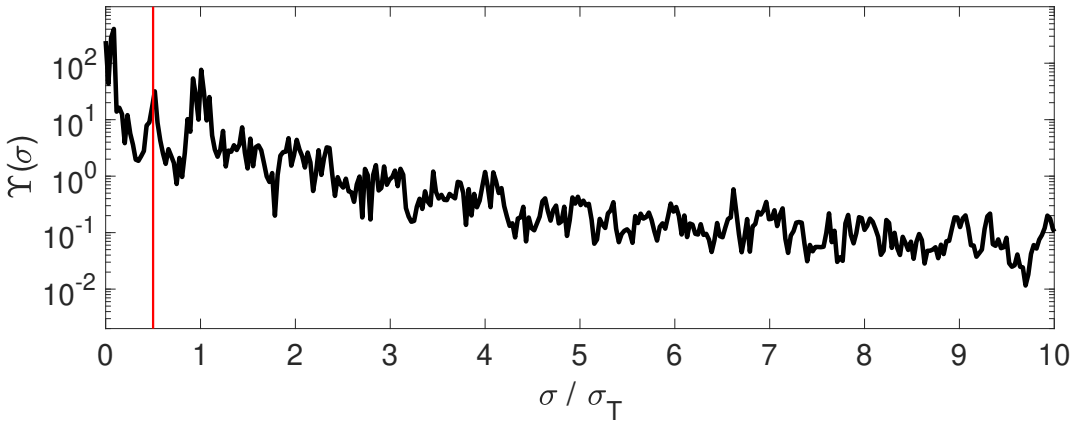

(a)

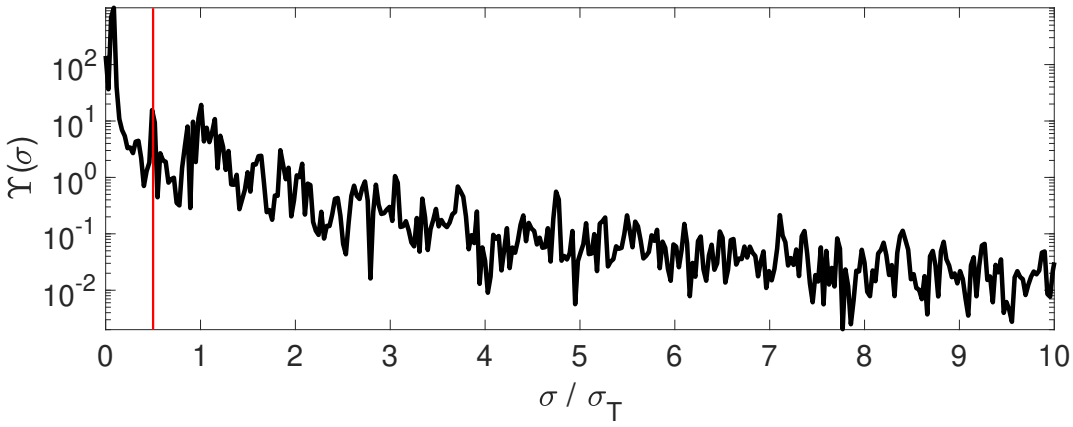

(b)

Figure 4.28: Spectrum $\gamma(\sigma)$ for case C1 at (a) $x = 45$ km and (b) $x = 51$ km. The shelf break is at 43 km. Red line marks $\sigma_T/2$. At these two locations, $f_{eff}^2 \leq 0$.

Chapter 5

Conclusions

In this thesis, we conducted two separate works to study the effects of a geostrophic current on ITs. In Chapter 3, we considered a flat bottom and how a baroclinic current can modify the propagation of a mode-1 IT. In particular, we investigated the amount of IT energy reflected from the current and the impact of the current on the transmitted wave field. These are quantified by considering the reflection coefficient R and the linear modal energy conversion P_n, where n is the modal number. A linear theory for the reflection coefficient R based on idealized barotropic currents has been presented. Under this setting, when $f/\sigma \in [0.71, 0.94]$ and $f_{eff} < \sigma$ so R is moderate, the local maximums of R coincide with the integer multiples of the current widths scaled by the incident IT wavelength $2L/\lambda$. This pattern disappears if V_{max} is very large. A linear equation for general barotropic currents is also proposed. The prediction from the theory is in good agreement with the results from the fully nonlinear numerical simulations.

Baroclinic currents have been investigated using the fully nonlinear numerical model MITgcm. Our parameter space covers typical geostrophic currents in the ocean and a wide range of f. We conclude that R is determined by the effective frequency f_{eff} and the interaction region L_w or how fast f_{eff} varies. This is consistent with our linear theory, though the theory is formulated for idealized barotropic currents. The reflection can be significant with R up to 50% if f_{eff} is large over a big enough area. The other conclusion is that the modal energy conversion P_2 is dependent on the horizontal variation of the density ρ_x, i.e. the vertical shear of the current V_z due to the thermal wind relation. P_2 is less than 6% among all our simulations. P_n with $n > 2$ is at least an order of magnitude smaller than P_2. This implies that the impact of the current on the transmitted wave field is small and the interaction of the ITs and currents is almost linear. P_2 in our runs is much smaller than the 13% conversion rate in Dunphy and Lamb [2014]. They used baroclinic

eddies. $\rho_x > 0$ in one half of the eddy while $\rho_x < 0$ in the other half so that N^2 stays the same outside of the eddy. With a geostrophic current, ρ_x is either greater or smaller than 0, either way N^2 to the left is different from that to the right of the current.

In Chapter 4, we considered a shelf-like bathymetry and the influence of a barotropic current on the IT generation process. The focus was on the total barotropic to baroclinic conversion rate. We use barotropic currents because it is the simplest way to study the effect of the horizontal shear of the current without complications of the varying stratification. We summarize how the presence of a geostrophic barotropic current $V(x)$ affects the conversion rate.

- $V(x)$ changes the effective frequency from $f_{eff}^2 = f^2$ to $f_{eff}^2 = f^2 + fV_x$. This has a direct impact on the slope of the IT characteristics γ and the slope criticality $\alpha = s/\gamma$. It has been shown previously that α is a crucial factor in determining the total conversion C (e.g. Baines [1982], Bell Jr [1975], Balmforth et al. [2002]).

- Since V_x is not a constant value, f_{eff} varies along the slope. This has a significant effect on IT beam generation location r_b and their propagation paths. When $f_{eff} < \sigma_T$, internal waves are generated everywhere along the slope. The intensity of the IT beams depends on the current, which also determines the beam generation location r_b. r_m is defined as the part of the slope where $\alpha > 0.99\alpha_{max}$. r_b is usually equivalent to or slightly larger than the upper bound of r_m because tidal forcing increases as the water depth decreases. With a slightly stronger current such that part of the slope is critical/supercritical, IT beams can be emitted near a critical point x_c if the slope is of the same sign as the slope of the beam and it is subcritical (supercritical) to the left (right) of x_c but not the other way around. With a strong current such that part of the slope acts as a blocking region where $f_{eff} > \sigma_T$, IT beams are emitted near a critical point and the conversion rate C becomes extremely small in the blocking region.

- The change of sign in $\overline{C}$ corresponds to the IT beam reflection location. As a result, the total conversion rate $C = C_p + C_n$ is also strongly affected by the IT beam pattern, which depends on V_x.

In conclusion, the total conversion rate C is affected by a combination of three factors: slope criticality α, the size and location of the blocking region where ITs cannot be generated and the IT beam pattern including where the beams are emitted and reflected, all of which can be varied by the geostrophic current V. In this chapter, we assumed $f > 0$, i.e., the Northern Hemisphere, and K_1 diurnal tides as the forcing. Our work can be extended

to the Southern Hemisphere by simply reversing the signs of f and V_{max}. It can also be applied to any other tidal constituents as long as f is close to the tidal frequency so that $\sigma_T^2 - f_{eff}^2 = \sigma_T^2 - f^2 - fV_x$ in (1.111) can vary significantly by varying V_x. This is easiest if $\sigma_T^2 - f^2$ is small. What matters is the dimensionless parameter $\tilde{f} = f/\sigma_T$. In our work, $\tilde{f} \geq 0.82$. At latitudes far from critical, i.e., $f \ll \sigma_T$ and $\tilde{f} \ll 1$, the slope criticality will be modified by V_x but the effects are expected to be reduced. As a result, the conversion rate is modified but not as much as that of the near-critical latitudes.

Although we considered idealized cases that use a linear stratification and a symmetric barotropic current, the key point of this work is that the current changes f_{eff} which changes the conversion. This is unlikely to change in a more realistic setting. For example, with a varying $N(z)$ in the absence of a current, the IT beams will bend instead of following a straight line. However, the presence of a current would affect how the beam bends and the slope criticality in the same way we have described in this thesis. Including baroclinic currents is an important future problem of this research, since it introduces horizontal density gradients. Other important future avenues of this research are to incorporate asymmetric currents and more realistic bathymetry.

In the last section 4.3 of Chapter 4, we have presented some preliminary results from analyzing the frequency spectrum of the generated IWs. We categorized the frequencies into three groups: PSI, interharmonics and tidal harmonics. There are many unanswered questions, such as, under what conditions does the PSI occur? when can a current play an important role? what are the physical mechanisms behind the subinertial waves generation?

References

Matthew H Alford, Jennifer A MacKinnon, Harper L Simmons, and Jonathan D Nash. Near-inertial internal gravity waves in the ocean. *Annual review of marine science*, 8: 95–123, 2016.

MH Alford, JA MacKinnon, Zhongxiang Zhao, Rob Pinkel, Jody Klymak, and Thomas Peacock. Internal waves across the pacific. *Geophysical Research Letters*, 34(24), 2007.

Adcroft Alistair, Campin Jean-Michel, Dutkiewicz Stephanie, Evangelinos Constantinos, Ferreira David, Forget Gael, Fox-Kemper Baylor, Heimbach Patrick, Hill Chris, Hill Helen, et al. Mitgcm user manual. Technical report, online, 2018.

Akio Arakawa and Vivian R Lamb. Computational design of the basic dynamical processes of the ucla general circulation model. *General circulation models of the atmosphere*, 17 (Supplement C):173–265, 1977.

Peter G Baines. On internal tide generation models. *Deep Sea Research Part A. Oceanographic Research Papers*, 29(3):307–338, 1982.

PG Baines. The generation of internal tides by flat-bump topography. In *Deep Sea Research and Oceanographic Abstracts*, volume 20, pages 179–205. Elsevier, 1973.

NJ Balmforth, GR Ierley, and WR Young. Tidal conversion by subcritical topography. *Journal of Physical Oceanography*, 32(10):2900–2914, 2002.

TH Bell. Lee waves in stratified flows with simple harmonic time dependence. *Journal of Fluid Mechanics*, 67(4):705–722, 1975.

TH Bell Jr. Topographically generated internal waves in the open ocean. *Journal of Geophysical Research*, 80(3):320–327, 1975.

John R Booker and Francis P Bretherton. The critical layer for internal gravity waves in a shear flow. *Journal of Fluid Mechanics*, 27(3):513–539, 1967.

Oliver Bühler and MICHAEL E McIntyre. Wave capture and wave–vortex duality. *Journal of Fluid Mechanics*, 534:67–95, 2005.

Maarten C Buijsman, Sonya Legg, and Jody Klymak. Double-ridge internal tide interference and its effect on dissipation in luzon strait. *Journal of Physical Oceanography*, 42 (8):1337–1356, 2012.

DA Cacchione, Lincoln F Pratson, and AS Ogston. The shaping of continental slopes by internal tides. *Science*, 296(5568):724–727, 2002.

Jule G Charney. The dynamics of long waves in a baroclinic westerly current. *Journal of Meteorology*, 4(5):136–162, 1947.

C Chavanne, P Flament, D Luther, and KW Gurgel. The surface expression of semidiurnal internal tides near a strong source at hawaii. part ii: Interactions with mesoscale currents. *Journal of Physical Oceanography*, 40(6):1180–1200, 2010.

Wen-Ssn Chuang and Dong-Ping Wang. Effects of density front on the generation and propagation of internal tides. *Journal of Physical Oceanography*, 11(10):1357–1374, 1981.

Sorin Codoban and Theodore G Shepherd. Energetics of a symmetric circulation including momentum constraints. *Journal of the atmospheric sciences*, 60(16):2019–2028, 2003.

PD Craig. Solutions for internal tidal generation over coastal topography. *Journal of Marine Research*, 45(1):83–105, 1987.

Benoit Cushman-Roisin and Jean-Marie Beckers. *Introduction to geophysical fluid dynamics: physical and numerical aspects*, volume 101. Academic press, 2011.

Thierry Dauxois, Sylvain Joubaud, Philippe Odier, and Antoine Venaille. Instabilities of internal gravity wave beams. *Annual Review of Fluid Mechanics*, 50:131–156, 2018.

Huw C Davies. Limitations of some common lateral boundary schemes used in regional nwp models. *Monthly Weather Review*, 111(5):1002–1012, 1983.

Jihai Dong, Robin Robertson, Changming Dong, Paul Scott Hartlipp, Tianyu Zhou, Zhibo Shao, Weihong Lin, Muzhi Zhou, and Jiarui Chen. Impacts of mesoscale currents on the diurnal critical latitude dependence of internal tides: A numerical experiment based on barcoo seamount. *Journal of Geophysical Research: Oceans*, 124(4):2452–2471, 2019.

Michael Dunphy and Kevin G Lamb. Focusing and vertical mode scattering of the first mode internal tide by mesoscale eddy interaction. *Journal of Geophysical Research: Oceans*, 119(1):523–536, 2014.

Michael Dunphy, Aurélien L Ponte, Patrice Klein, and Sylvie Le Gentil. Low-mode internal tide propagation in a turbulent eddy field. *Journal of Physical Oceanography*, 47(3):649–665, 2017.

ERIC T Eady. Long waves and cyclone waves. *Tellus*, 1(3):33–52, 1949.

Carl Eckart. Internal waves in the ocean. *The physics of fluids*, 4(7):791–799, 1961.

IA Eltayeb and JF McKenzie. Critical-level behaviour and wave amplification of a gravity wave incident upon a shear layer. *Journal of Fluid Mechanics*, 72(4):661–671, 1975.

David C Fritts and Li Yuan. An analysis of gravity wave ducting in the atmosphere: Eckart's resonances in thermal and doppler ducts. *Journal of Geophysical Research: Atmospheres*, 94(D15):18455–18466, 1989.

Chris Garrett and Eric Kunze. Internal tide generation in the deep ocean. *Annu. Rev. Fluid Mech.*, 39:57–87, 2007.

T Gerkema. Application of an internal tide generation model to baroclinic spring-neap cycles. *Journal of Geophysical Research: Oceans*, 107(C9):7–1, 2002.

Theo Gerkema, Frans-Peter A Lam, and Leo RM Maas. Internal tides in the Bay of Biscay: conversion rates and seasonal effects. *Deep Sea Research Part II: Topical Studies in Oceanography*, 51(25-26):2995–3008, 2004.

Adrian E Gill. *Atmosphere-Ocean Dynamics*, volume 30. Academic Press, 1982.

AE Gill, JSA Green, and AJ Simmons. Energy partition in the large-scale ocean circulation and the production of mid-ocean eddies. In *Deep sea research and oceanographic abstracts*, volume 21, pages 499–528. Elsevier, 1974.

Louis Gostiaux and Thierry Dauxois. Laboratory experiments on the generation of internal tidal beams over steep slopes. *Physics of Fluids*, 19(2):028102, 2007.

Nicolas Grisouard and Leif N. Thomas. Critical and near-critical reflections of near-inertial waves off the sea surface at ocean fronts. *Journal of Fluid Mechanics*, 765:273–302, January 2015.

Thomas WN Haine and John Marshall. Gravitational, symmetric, and baroclinic instability of the ocean mixed layer. *Journal of physical oceanography*, 28(4):634–658, 1998.

Mindy M Hall and Harry L Bryden. Direct estimates and mechanisms of ocean heat transport. *Deep Sea Research Part A. Oceanographic Research Papers*, 29(3):339–359, 1982.

Chris Halle and Robert Pinkel. Internal wave variability in the beaufort sea during the winter of 1993/1994. *Journal of Geophysical Research: Oceans*, 108(C7), 2003.

Philip Hazel. The effect of viscosity and heat conduction on internal gravity waves at a critical level. *Journal of Fluid Mechanics*, 30(4):775–783, 1967.

J Hazewinkel and KB Winters. Psi of the internal tide on a β plane: flux divergence and near-inertial wave propagation. *Journal of physical oceanography*, 41(9):1673–1682, 2011.

JH Hecht, RL Walterscheid, Michael P Hickey, and Steven J Franke. Climatology and modeling of quasi-monochromatic atmospheric gravity waves observed over urbana illinois. *Journal of Geophysical Research: Atmospheres*, 106(D6):5181–5195, 2001.

Peter E Holloway. A numerical model of internal tides with application to the Australian North West Shelf. *Journal of Physical Oceanography*, 26(1):21–37, 1996.

Peter E Holloway and Mark A Merrifield. Internal tide generation by seamounts, ridges, and islands. *Journal of Geophysical Research: Oceans*, 104(C11):25937–25951, 1999.

Peter E Holloway, Paul G Chatwin, and Peter Craig. Internal tide observations from the Australian North West Shelf in summer 1995. *Journal of Physical Oceanography*, 31(5): 1182–1199, 2001.

Louis N Howard. Note on a paper of john w. miles. *Journal of Fluid Mechanics*, 10(4): 509–512, 1961.

TY Huang, H Hur, TF Tuan, Xi Li, EM Dewan, and RH Picard. Sudden narrow temperature-inversion-layer formation in aloha-93 as a critical-layer-interaction phenomenon. *Journal of Geophysical Research: Atmospheres*, 103(D6):6323–6332, 1998.

Kenneth G Hughes and Jody M Klymak. Tidal conversion and dissipation at steep topography in a channel poleward of the critical latitude. *Journal of Physical Oceanography*, 49(5):1269–1291, 2019.

DG Hurley and G Keady. The generation of internal waves by vibrating elliptic cylinders. part 2. approximate viscous solution. *Journal of Fluid Mechanics*, 351:119–138, 1997.

R Michael Jones. A general dispersion relation for internal gravity waves in the atmosphere or ocean, including baroclinicity, vorticity, and rate of strain. *Journal of Geophysical Research: Atmospheres*, 110(D22), 2005.

WL Jones. A theory for quasi-periodic oscillations observed in the ionosphere. *Journal of Atmospheric and Terrestrial Physics*, 32(9):1555–1566, 1970.

D Kang. *Energetics and dynamics of internal tides in Monterey Bay using numerical simulations*. PhD thesis, Ph. D. dissertation, Stanford University, 2010.

Dujuan Kang and Oliver Fringer. Energetics of barotropic and baroclinic tides in the monterey bay area. *Journal of Physical Oceanography*, 42(2):272–290, 2012.

HussainH Karimi and TR Akylas. Parametric subharmonic instability of internal waves: locally confined beams versus monochromatic wavetrains. *Journal of fluid mechanics*, 757:381, 2014.

Samuel M Kelly and Pierre FJ Lermusiaux. Internal-tide interactions with the gulf stream and middle atlantic bight shelfbreak front. *Journal of Geophysical Research: Oceans*, 121(8):6271–6294, 2016.

S Khatiwala. Generation of internal tides in an ocean of finite depth: analytical and numerical calculations. *Deep Sea Research Part I: Oceanographic Research Papers*, 50 (1):3–21, 2003.

EM Kolomoitseva and LV Cherkesov. Generation of internal waves in the region of a bottom ridge with continuously varying height. *Physical Oceanography*, 9(6):433–443, 1999.

Alexander S Korobov and Kevin G Lamb. Interharmonics in internal gravity waves generated by tide-topography interaction. *Journal of Fluid Mechanics*, 611:61, 2008.

CR Koudella and Chantal Staquet. Instability mechanisms of a two-dimensional progressive internal gravity wave. *Journal of Fluid Mechanics*, 548:165–196, 2006.

Pijush K Kundu, Ira M Cohen, and DW Dowling. Fluid mechanics 4th, 2008.

Eric Kunze. Near-inertial wave propagation in geostrophic shear. *Journal of Physical Oceanography*, 15(5):544–565, 1985.

Eric Kunze. The energy balance in a warm-core ring's near-inertial critical layer. *Journal of Physical Oceanography*, 25:942–957, 1995.

Eric Kunze and Thomas B Sanford. Observations of near-inertial waves in a front. *Journal of Physical Oceanography*, 14(3):566–581, 1984.

Eric Kunze, Leslie K Rosenfeld, Glenn S Carter, and Michael C Gregg. Internal waves in Monterey submarine canyon. *Journal of physical oceanography*, 32(6):1890–1913, 2002.

Hsiao-lan Kuo. Dynamic instability of two-dimensional nondivergent flow in a barotropic atmosphere. *Journal of Meteorology*, 6(2):105–122, 1949.

AL Kurapov, JS Allen, and GD Egbert. Combined effects of wind-driven upwelling and internal tide on the continental shelf. *Journal of Physical Oceanography*, 40(4):737–756, 2010.

Kevin G Lamb. On the calculation of the available potential energy of an isolated perturbation in a density-stratified fluid. *Journal of Fluid Mechanics*, 597:415–427, 2008.

Kevin G Lamb and Jueun Kim. Conversion of barotropic tidal energy to internal wave energy over a shelf slope for a linear stratification. *Continental Shelf Research*, 33:69–88, 2012.

Dong-Kyu Lee and Pearn P. Niiler. The inertial chimney: The near-inertial energy drainage from the ocean surface to the deep layer. *Journal of Geophysical Research: Oceans*, 103 (C4):7579–7591, April 1998.

Sonya Legg and Karin MH Huijts. Preliminary simulations of internal waves and mixing generated by finite amplitude tidal flow over isolated topography. *Deep Sea Research Part II: Topical Studies in Oceanography*, 53(1-2):140–156, 2006.

Qiang Li, Xianzhong Mao, John Huthnance, Shuqun Cai, and Samuel Kelly. On internal waves propagating across a geostrophic front. *Journal of Physical Oceanography*, 49(5): 1229–1248, 2019.

R-C Lien and MC Gregg. Observations of turbulence in a tidal beam and across a coastal ridge. *Journal of Geophysical Research: Oceans*, 106(C3):4575–4591, 2001.

Richard S Lindzen and John W Barker. Instability and wave over-reflection in stably stratified shear flow. *Journal of Fluid Mechanics*, 151:189–217, 1985.

Stefan G Llewellyn Smith and WR Young. Conversion of the barotropic tide. *Journal of Physical Oceanography*, 32(5):1554–1566, 2002.

Rolf G Lueck and Todd D Mudge. Topographically induced mixing around a shallow seamount. *Science*, 276(5320):1831–1833, 1997.

J. Marshall, R. Ferrari, G. Forget, G. Maze, A. Andersson, N. Bates, W. Dewar, S. Doney, D. Fratantoni, T. Joyce, F. Straneo, J. Toole, R. Weller, J. Edson, M. Gregg, K. Kelly, S. Lozier, J. Palter, R. Lumpkin, R. Samelson, E. Skyllingstad, K. Silverthorne, L. Talley, and L. Thomas. The climode field campaign: Observing the cycle of convection and restratification over the gulf stream. *Bulletin of the American Meteorological Society*, 90 (9):1337–1350, September 2009.

John Marshall, Alistair Adcroft, Chris Hill, Lev Perelman, and Curt Heisey. A finite-volume, incompressible navier stokes model for studies of the ocean on parallel computers. *Journal of Geophysical Research: Oceans*, 102(C3):5753–5766, 1997.

Joseph P Martin, Daniel L Rudnick, and Robert Pinkel. Spatially broad observations of internal waves in the upper ocean at the Hawaiian ridge. *Journal of physical oceanography*, 36(6):1085–1103, 2006.

Eivind A Martinsen and Harald Engedahl. Implementation and testing of a lateral boundary scheme as an open boundary condition in a barotropic ocean model. *Coastal engineering*, 11(5-6):603–627, 1987.

Mark A Merrifield, Peter E Holloway, and TM Shaun Johnston. The generation of internal tides at the Hawaiian Ridge. *Geophysical Research Letters*, 28(4):559–562, 2001.

Sebastià Monserrat and Alan J Thorpe. Use of ducting theory in an observed case of gravity waves. *Journal of the atmospheric sciences*, 53(12):1724–1736, 1996.

Christopher NK Mooers. Several effects of a baroclinic current on the cross-stream propagation of inertial-internal waves. *Geophysical and Astrophysical Fluid Dynamics*, 6(3): 245–275, 1975.

Walter Munk and Carl Wunsch. Abyssal recipes II: Energetics of tidal and wind mixing. *Deep-sea research. Part I, Oceanographic research papers*, 45(12):1977–2010, 1998.

JR Munroe and KG Lamb. Topographic amplitude dependence of internal wave generation by tidal forcing over idealized three-dimensional topography. *Journal of Geophysical Research: Oceans*, 110(C2), 2005.

AL New and RD Pingree. Local generation of internal soliton packets in the central Bay of Biscay. *Deep Sea Research Part A. Oceanographic Research Papers*, 39(9):1521–1534, 1992.

Yoshihiro Niwa and Toshiyuki Hibiya. Three-dimensional numerical simulation of m2 internal tides in the East China Sea. *Journal of Geophysical Research: Oceans*, 109(C4), 2004.

Yoshihiro Niwa and Toshiyuki Hibiya. Estimation of baroclinic tide energy available for deep ocean mixing based on three-dimensional global numerical simulations. *Journal of oceanography*, 67(4):493–502, 2011.

Yoshihiro Niwa and Toshiyuki Hibiya. Generation of baroclinic tide energy in a global three-dimensional numerical model with different spatial grid resolutions. *Ocean Modelling*, 80:59–73, 2014.

Jonas Nycander. Tidal generation of internal waves from a periodic array of steep ridges. *Journal of Fluid Mechanics*, 567:415, 2006.

Isidoro Orlanski. Instability of frontal waves. *Journal of the Atmospheric Sciences*, 25(2): 178–200, 1968.

Isidoro Orlanski. The influence of bottom topography on the stability of jets in a baroclinic fluid. *Journal of the Atmospheric Sciences*, 26(6):1216–1232, 1969.

Isidoro Orlanski and Michael D Cox. Baroclinic instability in ocean currents. *Geophysical & Astrophysical Fluid Dynamics*, 4(1):297–332, 1972.

RC Pacanowski and SGH Philander. Parameterization of vertical mixing in numerical models of tropical oceans. *Journal of Physical Oceanography*, 11(11):1443–1451, 1981.

Jae-Hun Park and D Randolph Watts. Internal tides in the southwestern japan/east sea. *Journal of Physical Oceanography*, 36(1):22–34, 2006.

Joseph Pedlosky. Baroclinic instability in two layer systems. *Tellus*, 15(1):20–25, 1963.

Joseph Pedlosky. The stability of currents in the atmosphere and the ocean: Part i. *Journal of the Atmospheric Sciences*, 21(2):201–219, 1964.

Joseph Pedlosky. *Geophysical fluid dynamics*. Springer Science & Business Media, 2013.

Donald B Percival, Andrew T Walden, et al. *Spectral analysis for physical applications*. cambridge university press, 1993.

AF Pereira, BM Castro, L Calado, and ICA da Silveira. Numerical simulation of m2 internal tides in the south brazil bight and their interaction with the brazil current. *Journal of Geophysical Research: Oceans*, 112(C4), 2007.

Henry Perkins. Observed effect of an eddy on inertial oscillations. In *Deep Sea Research and Oceanographic Abstracts*, volume 23, pages 1037–1042. Elsevier, 1976.

François Pétrélis, Stefan Llewellyn Smith, and WR Young. Tidal conversion at a submarine ridge. *Journal of Physical Oceanography*, 36(6):1053–1071, 2006.

Norman A Phillips. Energy transformations and meridional circulations associated with simple baroclinic waves in a two-level, quasi-geostrophic model. *Tellus*, 6(3):274–286, 1954.

Norman A Phillips. Geostrophic motion. *Reviews of Geophysics*, 1(2):123–176, 1963.

KL Polzin, JM Toole, JR Ledwell, and RW Schmitt. Spatial variability of turbulent mixing in the abyssal ocean. *Science*, 276(5309):93–96, 1997.

Kurt L Polzin. Mesoscale eddy–internal wave coupling. part i: Symmetry, wave capture, and results from the mid-ocean dynamics experiment. *Journal of physical oceanography*, 38(11):2556–2574, 2008.

Kurt L Polzin. Mesoscale eddy–internal wave coupling. part ii: Energetics and results from polymode. *Journal of physical oceanography*, 40(4):789–801, 2010.

BS Powell, Ivica Janeković, GS Carter, and MA Merrifield. Sensitivity of internal tide generation in Hawaii. *Geophysical research letters*, 39(10), 2012.

SJ Prinsenberg, WL Wilmot, and Maurice Rattray Jr. Generation and dissipation of coastal internal tides. *Deep Sea Research*, 21:263–282, 1974.

Luc Rainville and Robert Pinkel. Observations of energetic high-wavenumber internal waves in the kuroshio. *Journal of physical oceanography*, 34(7):1495–1505, 2004.

Luc Rainville and Robert Pinkel. Propagation of low-mode internal waves through the ocean. *Journal of Physical Oceanography*, 36(6):1220–1236, June 2006.

Oceane Richet, Caroline Muller, and J-M Chomaz. Impact of a mean current on the internal tide energy dissipation at the critical latitude. *Journal of Physical Oceanography*, 47(6): 1457–1472, 2017.

Allan R Robinson and James C McWilliams. The baroclinic instability of the open ocean. *Journal of physical oceanography*, 4(3):281–294, 1974.

Jens Schafstall, Marcus Dengler, Peter Brandt, and Hermann Bange. Tidal-induced mixing and diapycnal nutrient fluxes in the Mauritanian upwelling region. *Journal of Geophysical Research: Oceans*, 115(C10), 2010.

Harper L Simmons. Spectral modification and geographic redistribution of the semi-diurnal internal tide. *Ocean Modelling*, 21(3-4):126–138, 2008.

Harper L Simmons and Matthew H Alford. Simulating the long-range swell of internal waves generated by ocean storms. *Oceanography*, 25(2):30–41, 2012.

Harper L Simmons, Robert W Hallberg, and Brian K Arbic. Internal wave generation in a global baroclinic tide model. *Deep Sea Research Part II: Topical Studies in Oceanography*, 51(25-26):3043–3068, 2004.

Joseph Smagorinsky. *Large eddy simulation of complex engineering and geophysical flows*. Cambridge University Press, 1993.

Louis St. Laurent and Chris Garrett. The role of internal tides in mixing the deep ocean. *Journal of Physical Oceanography*, 32(10):2882–2899, 2002.

Louis St. Laurent, Steven Stringer, Chris Garrett, and Dominique Perrault-Joncas. The generation of internal tides at abrupt topography. *Deep Sea Research Part I: Oceanographic Research Papers*, 50(8):987–1003, 2003.

Nataliya Stashchuk, Vasiliy Vlasenko, Phil Hosegood, and W Alex M Nimmo-Smith. Tidally induced residual current over the malin sea continental slope. *Continental Shelf Research*, 139:21–34, 2017.

Bruce R Sutherland and Kerianne Yewchuk. Internal wave tunnelling. *Journal of Fluid Mechanics*, 511:125–134, 2004.

Ali Tabaei and TR Akylas. Nonlinear internal gravity wave beams. *Journal of Fluid Mechanics*, 482:141, 2003.

Rémi Tailleux. Local available energetics of multicomponent compressible stratified fluids. *Journal of Fluid Mechanics*, 842, 2018.

SA Thorpe. Turbulence in stably stratified fluids: A review of laboratory experiments. *Boundary-Layer Meteorology*, 5(1-2):95–119, 1973.

John M Toole, Raymond W Schmitt, Kurt L Polzin, and Eric Kunze. Near-boundary mixing above the flanks of a midlatitude seamount. *Journal of Geophysical Research: Oceans*, 102(C1):947–959, 1997.

Cornelis A Van Duin and Hennie Kelder. Reflection properties of internal gravity waves incident upon a hyperbolic tangent shear layer. *Journal of Fluid Mechanics*, 120:505–521, 1982.

Clément Vic, Alberto C Naveira Garabato, JA Mattias Green, Amy F Waterhouse, Zhongxiang Zhao, Angélique Melet, Casimir De Lavergne, Maarten C Buijsman, and Gordon R Stephenson. Deep-ocean mixing driven by small-scale internal tides. *Nature communications*, 10(1):1–9, 2019.

Vasiliy Vlasenko, Nataliya Stashchuk, and Kolumban Hutter. *Baroclinic tides: theoretical modeling and observational evidence*. Cambridge University Press, 2005.

RL Walterscheid, JH Hecht, RA Vincent, IM Reid, J Woithe, and MP Hickey. Analysis and interpretation of airglow and radar observations of quasi-monochromatic gravity waves in the upper mesosphere and lower thermosphere over adelaide, australia (35 s, 138 e). *Journal of Atmospheric and Solar-Terrestrial Physics*, 61(6):461–478, 1999.

Robert A Weller. The relation of near-inertial motions observed in the mixed layer during the jasin (1978) experiment to the local wind stress and to the quasi-geostrophic flow field. *Journal of Physical Oceanography*, 12(10):1122–1136, 1982.

Daniel B Whitt and Leif N Thomas. Near-inertial waves in strongly baroclinic currents. *Journal of Physical Oceanography*, 43(4):706–725, 2013.

Kraig B Winters and Eric A D'Asaro. Two-dimensional instability of finite amplitude internal gravity wave packets near a critical level. *Journal of Geophysical Research: Oceans*, 94(C9):12709–12719, 1989.

Carl Wunsch and Raffaele Ferrari. Vertical mixing, energy, and the general circulation of the oceans. *Annu. Rev. Fluid Mech.*, 36:281–314, 2004.

Jiuxing Xing and Alan M Davies. A three-dimensional model of internal tides on the Malin-Hebrides shelf and shelf edge. *Journal of Geophysical Research: Oceans*, 103 (C12):27821–27847, 1998.

William R Young, Y-K Tsang, and Neil J Balmforth. Near-inertial parametric subharmonic instability. *Journal of Fluid Mechanics*, 607:25–49, 2008.

Xiaoming Zhai, Richard J Greatbatch, and Jun Zhao. Enhanced vertical propagation of storm-induced near-inertial energy in an eddying ocean channel model. *Geophysical research letters*, 32(18), 2005.

Weifeng G Zhang and Timothy F Duda. Intrinsic nonlinearity and spectral structure of internal tides at an idealized mid-atlantic bight shelf break. *Journal of physical oceanography*, 43(12):2641–2660, 2013.

Zhongxiang Zhao, Matthew H Alford, Jennifer A MacKinnon, and Rob Pinkel. Long-range propagation of the semidiurnal internal tide from the hawaiian ridge. *Journal of Physical Oceanography*, 40(4):713–736, 2010.

NV Zilberman, JM Becker, MA Merrifield, and GS Carter. Model estimates of m 2 internal tide generation over mid-atlantic ridge topography. *Journal of Physical Oceanography*, 39(10):2635–2651, 2009.

APPENDICES

Appendix A

The choice of background stratification

The choice of the background stratification N^2 requires a careful calculation. Here we present the details of determining the constant N^2 case.

N^2 refers to the buoyancy frequency sqaured to the left of the current, where the IWs are generated. We denote $N_g^2(x,z)+N^2$ and $\rho_g(x,z)+\rho(z)$ as the total buoyancy frequency squared and the total density field of the flow field, respectively. $\rho_g(x,z)$ and $N_g^2(x,z)$ are in geostrophic balance with the geostrophic current $V(x,z)$. Note $N_g^2(x,z)=0$ at the left of the current.

$$-fV_z = (\rho_g)_x g, \tag{A.1}$$
$$N_g^2 = -g(\rho_g)_z. \tag{A.2}$$

Assume $(x_0,z_0)=(0,0)$ and $V_{max}<0$. From the thermal wind relation A.1,

$$\rho_g = -\frac{f}{g}\int_{-\infty}^{x} V_z dx, \tag{A.3}$$
$$= -\frac{f}{g}\cdot V_{max}(-\frac{2z}{z_r^2})exp(-\frac{z^2}{z_r^2})\int_{-\infty}^{x} exp(-\frac{x'^2}{x_r^2})dx', \tag{A.4}$$
$$= \frac{2fz}{gz_r^2}V_{max}exp(-\frac{z^2}{z_r^2})\int_{-\infty}^{x} exp(-\frac{x'^2}{x_r^2})dx'. \tag{A.5}$$

We can have

$$N_g^2 = -g(\rho_g)_z, \tag{A.6}$$

$$= -\frac{2f}{gz_r^2} V_{max} \int_{-\infty}^{x} exp(-\frac{x'^2}{x_r^2}) dx' \cdot exp(-\frac{z^2}{z_r^2}) \cdot (1 - \frac{2z^2}{z_r^2}). \tag{A.7}$$

Some simple algebra gives the minimum of $N_g^2(x, z)$ occurs at $z = -\sqrt{\frac{3}{2}} z_r$ and $x = \infty$.

$$N_g^2 \geq \frac{4f\sqrt{\pi}}{z_r^2} V_{max} e^{-1.5} \cdot x_r. \tag{A.8}$$

To have a stable flow, we need

$$N_g^2 + N^2 \geq \frac{4f\sqrt{\pi}}{z_r^2} V_{max} e^{-1.5} \cdot x_r + N^2 \geq 0, \tag{A.9}$$

$$x_r \leq -\frac{N^2 e^{1.5} z_r^2}{4f\sqrt{\pi} V_{max}}. \tag{A.10}$$

Assume we want the diameter of the current is $4x_r = s \cdot \lambda$, where $s \geq 1$. Combining with A.10, we have

$$\lambda \leq -\frac{N^2 e^{1.5} z_r^2}{sf\sqrt{\pi} V_{max}}. \tag{A.11}$$

On the other hand,

$$\lambda = \frac{2\pi}{k}, \tag{A.12}$$

$$\approx \frac{2NH}{\sqrt{\sigma^2 - f^2}}. \tag{A.13}$$

Combining A.11 and A.13, we have

$$N \geq -\frac{2sHf\sqrt{\pi} V_{max}}{e^{1.5}\sqrt{\sigma^2 - f^2} z_r^2} \tag{A.14}$$

If we pick $f = 1 \times 10^{-4}/s$, $V_{max} = -0.5m/s$, $z_r = 650m$ and $s = 1.8$, we have $N_{min}^2 = 1.2 \times 10^{-5} s^{-2}$. This provides a first guess of N^2. Under this assumption, the IW wavelength, $\lambda = 140km$, is a reasonable value. Note decreasing z_r will largely increase N thus increase λ, which makes the internal waves unphysical. Similar analysis can be performed for $V_{max} > 0$.